

ADIATION DEFECTS IN MATERIALS AND THEIR CHARACTERIZATION USING ESR, UV-VISIBLE SPECTROMETRY AND TL

By
Santosh Kumar Suman
CHEM01201104028

Bhabha Atomic Research Centre, Mumbai

A thesis submitted to the
Board of Studies in Chemical Sciences
In partial fulfillment of requirements
For the Degree of
DOCTOR OF PHILOSOPHY
Of
HOMI BHABHA NATIONAL INSTITUTE

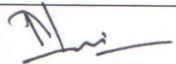
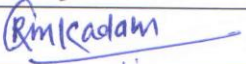

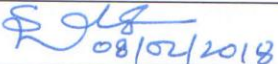
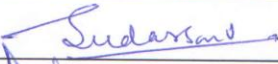



August, 2017

Homi Bhabha National Institute

Recommendations of the Viva Voce Committee

As members of the Viva Voce Committee, we certify that we have read the dissertation prepared by **Santosh Kumar Suman** entitled **RADIATION DEFECTS IN MATERIALS AND THEIR CHARACTERIZATION USING ESR, UV-VISIBLE SPECTROMETRY AND TL** and recommend that it may be accepted as fulfilling the thesis requirement for the award of Degree of Doctor of Philosophy.

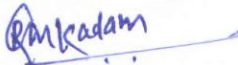
Chairman – Dr P K Pujari		Date: 08/02/2018
Guide / Convener – Dr. R M Kadam		Date: 08/02/2018
Co-guide - Dr Y K Bhardwaj		Date: 08/02/18
Examiner – Dr. Sanjay J. Dhoble	 08/02/2018	Date: 08/02/2018
Member 1- Dr V Sudarsan		Date: 08/02/2018
Member 2- Dr S Murali		Date: 08.02.2018

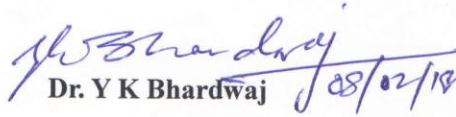
Final approval and acceptance of this thesis is contingent upon the candidate's submission of the final copies of the thesis to HBNI.

I/We hereby certify that I/we have read this thesis prepared under my/our direction and recommend that it may be accepted as fulfilling the thesis requirement.

Date: 08/02/2018

Place: BARC

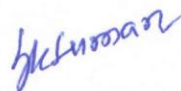

Dr. R M Kadam
Guide


Dr. Y K Bhardwaj
Co-guide

STATEMENT BY AUTHOR

This dissertation has been submitted in partial fulfillment of requirements for an advanced degree at Homi Bhabha National Institute (HBNI) and is deposited in the Library to be made available to borrowers under rules of the HBNI.

Brief quotations from this dissertation are allowable without special permission, provided that accurate acknowledgement of source is made. Requests for permission for extended quotation from or reproduction of this manuscript in whole or in part may be granted by the Competent Authority of HBNI when in his or her judgment the proposed use of the material is in the interests of scholarship. In all other instances, however, permission must be obtained from the author.



Santosh Kumar Suman

DECLARATION

I, hereby declare that the investigation presented in the thesis has been carried out by me. The work is original and has not been submitted earlier as a whole or in part for a degree / diploma at this or any other Institution / University.



Santosh Kumar Suman

List of Publications arising from the thesis Journal

1. "Vinyl content tailored flexible radio-opaque composites with improved interfacial, rheological and thermo-mechanical behaviors." S.K. Suman, Jitendra Kumar, R.K. Mondal, R.K. Gupta, K.A. Dubey, R.M. Kadam, J.S. Melo, Y.K. Bhardwaj, Lalit Varshney. European Polymer Journal, Vol-95, (2017), 41-55.
2. "Melt compounded ethylene vinyl acetate / magnesium sulfate composites as flexible EPR dosimeters: mechanical properties, dose response and processability", **S. K. Suman**, R.M. Kadam, R. K. Mondal, S. Murali, K. A. Dubey, Y. K. Bhardwaj, V. Natarajan, Applied Radiation and Isotopes, 121(2017), 82-86.
3. "Synthesis of a flexible poly (chloroprene)/methyl red film dosimeter using an environment-benign shear compounding method." **S. K. Suman**, Dubey, K.A., Mishra, B.B., Bhardwaj, Y.K., Mondal, R.K., Seshadri, M., Natarajan, V., Varshney, L. Applied Radiation and Isotopes Vol 98(2015), 60-65.
4. "Synthesis of flexible polymeric shielding materials for soft gamma rays: Physicomechanical and attenuation characteristics of radiation crosslinked polydimethylsiloxane/Bi₂O₃ composites." Dubey, K.A., Chaudhari, C.V., **S. K. Suman**, Rajeshwari, N., Mondal, R.K.,

Mondal, R.K., Grover, V., Murali, S., Bhardwaj, Y.K., Varshney, L.,
Polymer Composites Vol -37, (2016), 756-762.

Conferences

1. Dosimetric studies on radiation induced radicals in Barium sulphate using ESR, PL and TSL techniques; **S.K.Suman***, B.Rajeswari.,R.M.Kadam, S.Murali* and V.Natarajan ICLA-2015.
2. Development of flexible polymeric dosimeters for gamma dose measurement: color coordinates and dose response' by **S.K. Suman**, B.B Mishra, R.K. Mondal, K.A. Dubey, S.Murali, Natarajan V.(IARPNC 2014, March 19 -21, 2014, Mumbai,)
3. ESR Dosimetry – Investigation of Glass powder samples – **Suman S.K**, S. Murali, SatyaManojBairwa and M.K. Bhide – NUCAR-2014
4. Indigenous development of a low-cost EPR dosimeter in NICSSTAR-2015 held during 4-6 March 2015 (K. A. Dubey, **S. K. Suman**, R. M. Kadam, Y. K. Bhardwaj, L. Varshney, VNatarajan)

Santosh Kumar Suman

DEDICATED TO

MY FATHER AND MOTHER.....

ACKNOWLEDGEMENTS

At the outset, I would like to express my heartfelt gratitude to my research guide Prof. R M Kadam, RCD, BARC for his invaluable guidance, constant support and encouragement throughout the course of this work. I owe my sincere thanks to him for educating me in carrying out ESR work with his immense knowledge and support in ESR spectral recording, interpretation and data analysis. His guidance helped me during the entire time of research and writing this thesis.

My sincere thanks are also due to Dr. Y K Bhardwaj, RTDD who has helped me with all the polymer composite work and the data collection for mechanical properties and radiation effect on composites at HIRUP, BARC. His encouragement in helping me to improve my vocabulary in English and presentation skills would always be remembered.

I am deeply grateful to Dr. A K Dubey, RTDD for his expert guidance on selection of materials and their study on viability of use towards radiation protection. He has listened to my ideas to give refinement and his frequent discussions led to key insights to this work.

Quantification and analysis of Radiation defects by Electron Spin Resonance spectrometry was conducted at RCD, BARC. I will forever be thankful to Dr. V. Natarajan, ex-RCD, who introduced me to ESR dosimetry and allowed me to use the Electron Spin Resonance spectrometer at RCD, BARC, Mumbai.

I am grateful to Dr.P K Pujari Chairman, Doctoral Committee and Dr. V Sudarsan members of the Doctoral Committee, HBNI, for their for their motivation and constructive suggestions during the course of my work.

I express my sincere gratitude to Dr. R. K. Gopalakrishnan, Head, RHCS and Dr. K. S. Pradeepkumar, AD, HS & EG who have rendered constant support for completion of this research work along with my official duty assignments. I sincerely thank my senior colleague, Dr. S Murali, RSSD, for his continuous support during my Ph. D work related to literature study and research. I express my sincere thanks to Smt. Rajeswari, RCD for her timely support and help in compilation and corrections of the thesis work. My thanks are also due to Dr. Manoj Mohapatra, RCD for the assistance rendered by him in compilation of this work.

It is my pleasant duty to express my gratitude to C V Chaudhary, Raj Kumar Mondal RTDD in synthesis of nano composites and its analysis of mechanical properties and my colleagues Shri. S M Bhairwa, Shri. Pratap Singh, Malti, Vikash, Shailesh, Triveni, Ashma, RSSD.

I would like to express my appreciation for my wife, Mrs. Sujata Kiran, for her co-operation, love, support, encouragement and understanding during the course of my research project.

Finally, I would like to thank my beloved son Master Arpit, my respected Parents and In-laws for their constant support and help for all my accomplishments in this work.

Contents

Synopsis

List of figures

List of tables

Chapter 1-Introduction to Interaction of Radiation with Matter and Dosimetry

1.1. Interaction of radiation with matter.....	2
1.2. Radiation Induced defects/effects in matter.....	5
1.3. Quantification of radiation dose.....	6
1.3.1. Essentials of a dosimetry system.....	7
1.3.2. Techniques for dosimetric evaluation.....	8
1.3.2.1. Calorimetry.....	8
1.3.2.2. Fricke dosimetry.....	8
1.3.2.3. FBX dosimetric.....	8
1.3.2.4. Film badge dosimetry.....	9
1.3.2.5. Thermo luminescent dosimetry.....	9
1.3.2.6. ESR dosimetry.....	10
1.3.2.7. Thermally Stimulated Luminescence (TSL).....	11
1.4. Literature Survey.....	12
1.5 Outline of work.....	22

Chapter 2-Experimental methodology and characterization techniques

2.1. Introduction.....	29
2.2. Materials.....	29
2.3. Sample Preparation.....	30
2.4. Gamma radiation source.....	30
2.5. Dosimetry.....	31

2.5.1 Fricke dosimetry.....	33
2.5.2. ESR dosimetry.....	34
2.5.2.1 Splitting in electron spin resonance spectra.....	37
2.5.2.2 Electronic splitting.....	37
2.5.2.3 Hyperfine splitting.....	37
2.6 Thermally stimulated luminescence.....	38
2.7 Characterization techniques.....	39
2.7.1 Crosslinking Density.....	39
2.7.2 Optical Microscopy.....	39
2.7.3 UV-Visible Spectrophotometer.....	40
2.7.4 FTIR spectrophotometer.....	40
2.7.5 Thermo gravimetric analysis (TGA).....	41
2.7.6. Differential scanning calorimetry (DSC).....	42
2.7.7 Scanning electron microscopy (SEM).....	42
2.7.8 Atomic Force Microscope (AFM).....	43
2.7.9 Radiopacity and mass attenuation coefficients.....	43
2.7.10 Viscoelastic properties.....	43
2.7.11 Mechanical Properties.....	44
2.7.12 X-Ray Diffraction (XRD).....	44
2.7.13 Physical Properties.....	45
2.8. Summary.....	46

Chapter 3-Effect of high energy irradiation on polymer composites, synthesis of radio opaque composites and radiation shields

3.1 General Introduction.....	49
3.2. Material and methods.....	55
3.2.1. Materials.....	55
3.2.2. Sample preparation.....	56
3.2.3. Radiation source.....	56
3.2.4. Physico-mechanical properties.....	57
3.2.5. Viscoelastic properties.....	57

3.2.6. Sorption studies.....	58
3.2.7. Thermo gravimetric analysis.....	58
3.2.8. Scanning electron microscopy, atomic force microscopy, and X-Ray Diffraction.....	59
3.2.9. Radiopacity and mass attenuation coefficients.....	59
3.3. Results and discussion.....	60
3.3.1. Cross-linking density of the PDMS/bismuth oxide composites.....	60
3.3.2. Filler interaction in PDMS/bismuth oxide composites.....	63
3.3.3. Mechanical properties of PDMS/bismuth oxide composites.....	65
3.3.4. Thermo-gravimetric analysis of PDMS/bismuth oxide composites.....	67
3.3.5. γ -attenuation by PDMS/bismuth oxide composites.....	68
3.3.6. Dispersion, interface, and crystallinity of EVA/ BaSO ₄ composites.....	70
3.3.7. Radiopacity of EVA/BS composites.....	72
3.3.8. Physico-mechanical properties and mechanical hysteresis of EVA/ BaSO ₄ Composites.....	75
3.3.9. Effect of VA content and of BS loading on dynamic Rheology.....	76
3.3.10. Filler-filler contact break, polymer-filler interface breakdown in EVA/BaSO ₄ composite.....	81
3.3.11. Visco-elastic master curve and fractional free volume of composite Melts in EVA/ BaSO ₄ composites.....	84
3.3.12. Dynamic thermo-mechanical analysis of EVA/ BaSO ₄ composites.....	87
3.4 Summary.....	89

Chapter 4-Synthesis of a flexible poly(chloroprene) / Methyl red film dosimeter using an Environment-benign shear compounding method

1.1. General Introduction.....	119
4.2. Material and methods.....	121
4.2.1 Dosimeter preparation.....	121
4.2.2 Radiation source.....	121
4.2.3 Spectrophotometry.....	122
4.2.4 Colour measurements.....	122
4.2.5 Humidity standardization.....	122
4.3. Results and discussion.....	123
4.3.1. Effect of dye concentration and dehydrochlorination on the spectral features.....	123
4.3.2. Effect of composition on dose range and sensitivity.....	125
4.3.3. Effect of radiation dose on color coordinates.....	126
4.3.4. Reproducibility of radiation response.....	127
4.3.5. Effect of dose rate.....	127
4.3.6. Effect of humidity and temperature.....	128
4.3.7. Effect of storage duration.....	128
4.3.8. Processing parameters and optical microscopy.....	129
4.4. Summary.....	130

Chapter 5-Melt compounded ethylene vinyl acetate/magnesium sulfate composites as flexible EPR dosimeters: mechanical properties, dose response and processability

5.1. General Introduction.....	136
5.2. Materials and method.....	138
5.2.1 Material and sample preparation.....	138
5.2.2 Radiation source.....	138
5.2.3 Physico-mechanical properties.....	140
5.2.4 EPR studies.....	140
5.3. Results and discussion.....	141

5.2.1. Mechanical properties, melt flow index and density.....	141
5.2.2. ESR signal and power dependence.....	142
5.2.3. Linearity, fading and reproducibility.....	143
5.2.4. Water equivalency.....	144
5.3. Summary.....	145
Chapter 6-Europium doped Barium sulphate as a perspective dosimeter:	
Studies based on ESR, TSL and PL techniques	
6.1. Introduction.....	156
6.2. Experimental.....	158
6.2.1. Sample preparation.....	158
6.2.2. Sample Characterization.....	158
6.3. Results and discussion.....	159
6.3.1. XRD results.....	159
6.3.2. Thermally Stimulated Luminescence (TL) Studies.....	160
6.3.3. Photo Luminescence (PL) studies.....	160
6.3.4. Electron Spin Resonance (ESR) studies	161
6.4. Summary.....	163
Conclusions and future scope	170
References.....	175

SYNOPSIS

Ionizing radiation is known to induce physical, chemical or biological changes in materials. It is necessary to understand radiation induced defects [1-4] as they can be tailored to induce different advantages and disadvantages. The knowledge of the amount of energy absorbed per unit mass of the absorber and distribution of the absorbed energy in the absorbing material [1-3] is of critical importance in using high energy radiation for different applications. Radiation dosimetry [1-2,3] constitutes determination of these quantities. High-Range dosimetry [6-7] is an area of utmost interest to Health Physics, Medical Physicists and for accidental dose assessments during radiation incidences. This is also important during planned high irradiation at industrial irradiators. Even though a variety of techniques are presently available for the dosimetry, depending upon the requirements of dose measurement ranges, large scope exists for development of high-level dosimetry for industrial uses, therapeutic purposes and for investigating radiation accidents.

This thesis aims at investigating the effect of high energy radiation in different polymer and polymer composites to investigate the fundamental aspects of radiation induced defects in few matrices and to develop radio-opaque materials and advanced radiation dosimeters. It has been shown that incorporation of other component (polymers or nano-particulate fillers) in a polymer can influence the radiation attenuation and radical yield in the base polymer matrix. The study has also explored the plausible mechanisms behind the observed effects in the light

of various microscopic and macroscopic changes taking place in polymer matrix during nanocomposite/blend formation process as well as during irradiation. The results have been explained on the basis of polymer filler interactions, Electron Paramagnetic Resonance (ESR) measurements, rheometry, hardness, bulk density, dynamic mechanical analysis, X Ray Diffraction (XRD) and scanning electron microscopy. The work embodied in this thesis has been divided into six chapters.

Chapter-I: Introduction

Chapter 1 of the thesis introduces the subject of radiation, its interaction with matter, dosimeters, polymers, attenuation, radiation degradation and crosslinking of polymers. The details presented also include the modes of energy deposition and distribution of the absorbed energy in the medium. An introduction to the properties and applications of polymer blends and nanocomposites has also been incorporated. The chapter further explores the recent research on the radiation induced modification of thermoplastics, elastomers along with their applications in radiation dosimetry and radio-opacity.

Chapter 2: Materials and Methods

During the course of this study, a variety of methods have been employed to synthesize Dosimetric materials and polymer composites and their characterizations have been carried out using numerous characterization techniques. These include steady-state irradiation facilities, such as ^{60}Co Gamma Chamber and characterization techniques such as Melt Flow Index (MFI),

Atomic Force Microscopy (AFM), X-ray Scattering (XRD), UV-visible Spectroscopy, Electron Paramagnetic Resonance etc. The characteristics of various polymers, fillers and other reagents used in the study are also mentioned in this chapter.

Chapter 3: Effect of high energy irradiation of polymer composites, Synthesis of radio opaque composites and radiation shields

Radio-opacity of polymer based medical implants and drug eluting stents to the diagnostic X-rays is a highly desirable attribute to avoid expensive radiology or invasive approaches for the placement and performance monitoring of implants. Ethylene vinyl acetate copolymer and barium sulfate composites can be tailored to offer different mechanical and radio-opacity by modulating vinyl content in the copolymer and high loading 75% of barium sulfate can be obtained without mechanical integrity and flexibility. Extensive rheological, mechanical hysteresis and thermo-mechanical analysis was done to understand how BaSO₄ and vinyl segments interact. It was found that 0.5 mm sheet of ethylene vinyl acetate /BaSO₄ has markedly higher gray value (radio-opacity) than 1 mm sheet of aluminum, while having more than 400% elongation at break and complete flexibility even at 75% BaSO₄ content. Storage modulus and complex viscosity of the melt showed high dependence on VA content and BAS loading. The Payne effect was highest in the composites with lowest VA content and the morphology of the composites, as investigated by atomic force microscopy and scanning microscopy revealed marked influence on interphase behaviour and dispersion.

Flexible lead-free high energy radiation shielding material[4] was synthesized through internal compounding. Polymer-filler interaction, crosslinking density, specific gravity, physico-mechanical characteristics, percentage attenuation and thermal stability of the crosslinked composites were estimated[10-12]. It was found that even at very high filler loading composites can be crosslinked; however crosslinking density was composition dependent and was highest in 10-50 wt% loading range at all radiation doses. The Nielsen model was applied to understand micromechanics of the system. Attenuation of gamma radiation from ^{241}Am was not affected by irradiation. Thermal stability of composites was found to be significantly affected with bismuth oxide loading. In addition to the dispersion, PDMS/ Bi_2O_3 composites have other characteristics required for practical application such as high attenuation, good physico-mechanical and thermal characteristics

Chapter 4: Synthesis of a flexible poly(chloroprene)/Methyl red film dosimeter using an environment-benign shear compounding method

A dosimetric film[5-7] was synthesized through a solvent free route using polychloroprene rubber was doped with different concentrations of Methyl Red (MR) using an internal compounder. All the synthesized films displayed strong red colour with a λ_{max} around 515 nm, which was very different from the other reported studies for MR and was attributed to the presence of residual HCl in the chloroprene matrix. The peak position was independent of the concentration and the irradiation dose administered. The absorbance decreased with the irradiation

dose and the response was linear up to 30 kGy; though the regression values were poor when MR loading was less than 10 MR. The reproducibility and stability of the dosimeter was good. The color coordinates of the films was found to change with the irradiation dose and there was no significant yellowing or crosslinking of the base polymer in the irradiation dose range administered during the study. There was no significant effect of temperature and dose rate though some effect of humidity was observed when humidity was >70%. The optical micrograph of the films suggested homogeneous distribution up to 30 mg. The chapter will also present the radiation effect on EPDM/MR based dosimeters, demonstrating the criticality of dispersion of dye in polymer matrix for the perception of color and dosimetric properties.

Chapter 5: Melt compounded Ethylene Vinyl Acetate / Magnesium Sulfate composites as flexible EPR dosimeters: Mechanical properties, Dose response and Processability

Melt compounding of Ethylene Vinyl Acetate (EVA) (vinyl content 40%) and Magnesium Sulfate was carried out to develop ESR dosimeters[13-15] through a solvent free route. Mechanical properties, melt flow characteristics, dosimetric properties and water equivalency of the set of new dosimeters were investigated. Elastic modulus of the composites increased with the addition of MGH and elongation at break decreased. The composites were flexible and were found to flow during melt flow index measurements up to 50 wt% MGH. The response of dosimeter was linear between 20 Gy to 4 kGy. The response was reproducible

with the relative standard error of 0.06 (95% CI: 0.05-0.07). Dosimeters showed around 20% fading in the signal in 30 days and were found to be water equivalent for the energy greater than 100 keV.

Chapter 6: Europium doped Barium sulphate as a perspective dosimeter: Studies based on ESR, TSL and PL techniques

Polycrystalline samples of Europium (Eu) doped BaSO₄ were prepared by the co-precipitation method. These samples were annealed at high temperatures 550 °C, 750 °C and 900 °C in presence of argon atmosphere. The structural analysis carried out using X-ray diffraction (XRD) revealed that these samples exhibited orthorhombic structure. The samples annealed at high temperatures 550 °C, 750 °C and 900 °C were subsequently gamma irradiated at room temperatures were studied by Electron Paramagnetic Resonance (ESR), Thermally Stimulated Luminescence (TSL) [15-17] and Photo Luminescence (PL) techniques for measuring the signal for estimating the radiation dose which forms a prospective material for radiation dosimeter. The irradiated sample had a simple glow curve structure with prominent TSL glow peaks at 450 K and 500 K. ESR studies carried out on gamma irradiated BaSO₄ and Europium doped BaSO₄ samples revealed two prominent signals due to the presence of SO₄⁻ (g= 2.0140) and SO₃⁻ (g_{iso}= 2.0030) radicals. The intensities of both these radicals was found to be higher in samples annealed at 750 °C and therefore these samples were subsequently selected for investigating the dose response. The gamma irradiated samples did not show any significant changes in PL intensity of Eu²⁺ for both excitation and emission spectra indicating that there is no Eu²⁺ to Eu³⁺ valence

conversion occurring during gamma irradiation. Both Europium doped and undoped BaSO₄ samples had shown a linear gamma dose response over the range 10 Gy – 1 kGy. The dose response and fading properties of BaSO₄ samples were compared in ESR spectra. The sensitivity of Europium doped BaSO₄ to gamma irradiation was nearly five times better than that of Alanine. The fading characteristic of SO₃⁻ and SO₄⁻ radicals was found to be less in Europium doped BaSO₄ samples compared to un-doped samples suggesting that the former is better dosimetric material for dose measurements. The fading of SO₃⁻ and SO₄⁻ intensities in 750 °C annealed Europium doped BaSO₄ sample was of the order 5 % and 9% after a period of six months. ESR technique had shown practical applications in the field of dosimetry as the cumulative concentration of radiation-induced radicals could be quantified. The radiation induced paramagnetic radicals was assayed quantitatively using ESR technique, with the intensity of the ESR signal as a function of radiant energy deposited in the sample. Such techniques find applications in radiation dosimetry. New materials are investigated for feasibility of use in ESR dosimetry, wherein the radiation induced species retains the radiation signatures as a function of irradiation dose, leading to assessment of gamma radiation dose. Few of the materials have been identified as prospective ESR dosimeters. Alanine, an amino compound, is IAEA reference standard for ESR dosimetry.

Studies were carried out on gamma irradiated commercial amorphous glass samples in powder form, to investigate the possibility of using it as an ESR dosimeter. The first derivative ESR spectrum of such irradiated amorphous glass

samples, recorded at room temperature showed prominent signals due to oxy radicals of silicon at $g = 2.0023$ and 2.009 . It had been observed from ESR signal – irradiation dose response of irradiated glass powder that signal due to $g = 2.0023$ as linear in gamma dose range $200 \text{ Gy} - 2 \text{ kGy}$, the signal due to 2.009 had microwave power dependence in the range $6.2 \text{ } \mu\text{W}$ to 6.2 mW and the radiation induced radicals in glass were found to be stable (less than 5% decay) at RT for over 3 months. This investigation described the details on dose response of the irradiated glass powder as prospective dosimeter and the utility of ESR – Glass dosimetry for high range dosimetric applications.

Summary

Present thesis describes results from the research work carried out towards radiation engineering and characterization of polymer, dosimetric materials and composite materials using ^{60}Co -gamma, Electron beam irradiation. Effect of variation of different reaction parameters on the material properties was thoroughly studied and accordingly optimized to obtain polymer composites with desired properties.

References:

1. Knoll, Glenn F. (2000), Radiation detection and measurement, Wiley & Sons, New York.
2. Price, William, J. (1964), Nuclear radiation detection, Mc Graw Hill, New York.
3. Gupta B.L. and Bhat R.M. (1986), Calibration of high – dose radiation facilities, BARC – 1303.

4. Nayak A.R., (1998), Interaction of radiation with matter, IAEA regional basic professional course on radiation protection.
5. Attix F.H., Roesch W.C. (1968), Radiation dosimetry, Vol.II, Academic Press, New York.
6. Ajji, Z., 2006. Usability of aqueous solutions of methyl red as high-dose dosimeter for gamma radiation. Radiat. Meas. 41, 438-442.
7. Al Zahrary, A., Rabaeh, K., Basfar, A., 2011. Radiation-induced color bleaching of methyl red in polyvinyl butyral film dosimeter. Radiat. Phys. Chem. 80, 1263-1267.
8. Babic, S., McNiven, A., Battista, J., Jordan, K., 2009. Three-dimensional dosimetry of small megavoltage radiation fields using radiochromic gels and optical CT scanning. Phys. Med. Biol. 54, 2463-2481.
9. Barakat, M.F., El-Salamawy, K., El-Banna, M., Abdel-Hamid, M., Abdel-Rehim Taha, A., 2001. Radiation effects on some dyes in non-aqueous solvents and in some polymeric films. Radiat. Phys. Chem. 61, 129-136.
10. Dubey, K.A., Bhardwaj, Y.K., Chaudhari, C.V., Bhattacharya, S., Gupta, S.K., Sabharwal, S., 2006. Radiation effects on SBR–EPDM blends: A correlation with blend morphology. J. Polym. Sci. Pol. Phys. 44, 1676-1689.
11. Dubey, K.A., Bhardwaj, Y.K., Chaudhari, C.V., Goel, N.K., Sabharwal, S., Rajkumar, K., Chakraborty, S.K., 2011. Radiation effects on styrene-

- butadiene-ethylene-propylene diene monomer-multiple walled carbon nanotube nanocomposites: Vulcanization and characterization. *Polym. Advan. Technol.* 22, 1888-1897.
12. Dubey, K.A., Bhardwaj, Y.K., Rajkumar, K., Panicker, L., Chaudhari, C.V., Chakraborty, S.K., Sabharwal, S., 2012. Polychloroprene rubber/ethylene-propylene diene monomer/multiple walled carbon nanotube nanocomposites: synergistic effects of radiation crosslinking and MWNT addition. *J. Polym. Res.* 19, 9876-9876.
 13. W. Gordy, Theory and applications of electron spin resonance, John Wiley & Sons, New York. (1980).
 14. Ralph Mathews, Aqueous chemical Dosimetry, *App. Radiat. Isot.* 33, (1982)
 15. Murali, V. Natarajan, R. Venkataramni, Pushparaja and M. D. Sastry, ESR Dosimetry using inorganic materials a case study of Li_2CO_3 and $\text{CaSO}_4\text{:Dy}$ as prospective dosimeters, *Applied Radiation and Isotopes*, 55, 253-258, (2001).
 16. V.Gorome, P. Iacconi, D.Lapraz, H.Prevost, A.Baumer, TL of undoped and Dy doped CaSO_4 ; effect of preparation method, *Radiat. Prot. Dosi.* 65, 309- 312(1996)
 17. O.Annalakshmi, M. T. Jose* and U. Madhusoodanan, synthesis and characterization of $\text{BaSO}_4\text{:Eu}$ Thermo luminescence phosphor, *Radiation Protection Dosimetry* (2012), pp. 1–7

List of figures

Chapter-1

Figure-1.1a: Energy dependence of the various gamma ray interaction processes in sodium Iodide

Figure-1.1b Relative importance of the three principal interactions of photons in matter

Chapter-2

Figure-2.1: BRUKER ESR spectrometer

Figure-2.2: Basic electron resonance and Electronic Zeeman splitting

Figure-2.3: Hyperfine Coupling

Figure-2.4: TSL electronic process

Chapter-3

Figure-3.1: Variation in cross-linking density of composites with absorbed dose (a) 100kGy (b) 200kGy (c) 400 kGy

Figure-3.2: Variation in density of composites with absorbed dose. (a)Experimental values (b) Theoretical values theoretical. Inset: Percentage changes in density with the loading of Bi₂O₃ (Weight %)

Figure-3.3: Variation of swelling ratio [$Q_i = (\text{Swelled weight}/\text{initial polymer weight})$]of composites with absorbed dose (a) 100 kGy (b) 200 kGy (c) 400 kGy Inset: Kraus plot for PDMS/Bi₂O₃ composites

Figure-3.4; Variation in elongation at break of composites with absorbed dose
(a) 100 kGy (b) 200 kGy (c) 400 kGy

Figure 3.5: Variation in elastic modulus of composites with absorbed dose (a)
100 kGy (b) 200 kGy (c) 400 kGy

Figure-3.6: Thermo-gravimetric profiles of composites containing different
percentages of Bi₂O₃ (profiles have been offset for better clarity)

Figure-3.7: Variation in attenuation of different composites irradiated to
different doses. Inset: Variation in counts with Bi₂O₃ (Weight %) at two
different radiation doses.

Figure-3.8: Scanning electron micrographs of cryogenic fracture surfaces of
EVA/ BaSO₄ composites (a) VA12BS50 (b) VA25BS50 (c) VA40BS50.

Figure-3.9: Atomic force microscopy of the composites (a) Phase image of (i)
VA12BS50 (ii) VA25BS50 (iii) VA40BS50 (b) topographical images of (i)
VA12BS50 (ii) VA25BS50 (iii) VA40BS50 (c) histograms of surface
roughness (i) VA12BS50 (ii) VA25BS50 (iii) VA40BS50

Figure-3.10: X-ray diffractograms of (a) EVA with different VA content 12 %
(VA12), 25% (VA25) and 40% (VA40) [Inset: X-ray diffractograms of BS] (b)
VA12BS50, VA25BS50 and VA40BS50

Figure-3.11: Radiopacity of the composites (i) actual x-ray radiographs of
different composites, A: VA12BS75, B: VA40BS75, C: VA12BS50, D:
VA25BS50, E: VA40BS50, F: VA12BS50 (ii) variation in gray values for
composites with composition; dotted block presents gray values for aluminum

sheets (iii) variation in mass attenuation coefficient variation of VA12, VA25 and VA40 with x-ray energy (Inset: variation in the mass attenuation coefficient of BS with x-ray energy)

Figure-3.12: Effect of VA content on mechanical properties (a) Stress-strain profile (Left panel VA12 composites; right panel VA40 composites) (b) Mechanical hysteresis in the composites during five cyclic deformations of 5% (5-10%) strain. The arrows show mechanical hysteresis reduces with increase in VA content.

Figure-3.13: Physical and mechanical properties of the EVA/BS composite (a) Density (b) Elongation at break (c) Elastic modulus (d) Hardness (shore A). The properties are presented for different BaSO₄ content (%) and for different VA content

Figure-3.14: Effect of the VA content and the filler loading on (a) dependence of the complex viscosity on angular frequency in the linear visco-elastic regime [Inset: Fold increase in complex viscosity on filler addition; defined as the ratio of complex viscosity of filled system to the unfilled one] (b) dependence of the storage modulus (G') on the angular frequency in the linear visco-elastic regime (c) Cole-Cole representations for different EVA/ BaSO₄ composites in the linear visco-elastic regime. $T=140.0\text{ }^{\circ}\text{C}$,

Figure-3.15 Storage (G') and loss modulus (G'') crossover for different EVA/ BaSO₄ composites. $T=140.0\text{ }^{\circ}\text{C}$,

Figure-3.16: Melt rheology of unfilled systems (a) dependence of the complex viscosity on angular frequency in the linear viscoelastic regime (b) dependence of the storage modulus (G') on the angular frequency in the linear viscoelastic regime (c) Cole-Cole representations for different EVA in the linear viscoelastic regime. $T=140.0\text{ }^{\circ}\text{C}$,

Figure-3.17: Structural breakdowns in EVA/BS composites in molten and solid states (a) dependence of the storage modulus on the small amplitude oscillatory shear strain (b) dependence of the storage modulus on the dynamic tensile strain (solid) [$f=1\text{ Hz}$, $T=30^{\circ}\text{C}$]. Dotted lines represented best fit of the experimental data to phenomenological quantitative Kraus model (equation iii).

Figure-3.18: Time temperature (t - T) superimposition curves of storage and loss modulus for different EVA/ BaSO_4 composites. Reference temperature= 140°C .

Figure-3.19 Temperature dependence and model fitting of horizontal shift factors (a_T) of EVA/ BaSO_4 composites (a) WLF model (b) Arrhenius model

Figure-3.20: Dynamic thermo-mechanical changes in EVA/ BaSO_4 composites with the change in vinyl acetate content and BS loading (a) storage modulus versus temperature (b) loss factor versus temperature [% depicts percentage loading of BaSO_4 in the respective composite]

Figure-3.21: Scheme depicting interplay of crystalline domains, vinyl acetate groups, and BaSO_4 particles distribution in the matrix.

Chapter-4

Figure-4.1: Molecular structures of Methyl red and Polychloroprene

Figure- 4.2 : Visible spectrum of PC doped with different concentrations of MR/100g PC (a) 0 mM (b) 0.02 mM (c) 0.04 mM (d) 0.06 mM (e) 0.12 mM

Figure-4.3: Relative change in absorbance with radiation dose for the film containing (a) 0.04 mM of MR/100 g of PC (b) 0.06 mM of MR/100 g of PC.

Inset: Relative change in absorbance with radiation dose for the film containing 0.12 mM of MR/100 g of PC

Figure-4.4: Changes in polymer films (0.06 mM of MR/100 g of PC) irradiated to 10 kGy. (a) Relative change in absorbance [(RCA at 0.21 kGy/hr – RCA at specific dose rate)/ RCA at 0.21 kGy/hr] at different dose rates. (b) Relative change in absorbance kept under laboratory light conditions. Inset: Relative change in absorbance [(RCA at 11% humidity – RCA at specific humidity)/ RCA at 11% humidity] for polymer films (0.06 mM of MR/100 g of PC) irradiated to 10 kGy at different humidity.

Figure-4.5: Optical micrograph of polymer films made using two different polymer systems and two MR concentrations (a) 0.06 mM of MR/100g PC (b) 0.30 mM of MR/100g PC (c) 0.06 mM of MR/100g EPDM (d) 0.30 mM of MR/100g PC

Figure 4.6: Photograph of films loaded with 0.06 mM of MR/100g PC (a) unirradiated (b) irradiated to 30 kGy.

Chapter-5

Figure-5.1: Variation in the mechanical properties with increase in MGS weight percentage (a) Tensile strength (b) Elastic modulus (c) Elongation at break

Figure-5.2: Variation in the melt flow index with increase in MGS weight percentage

Figure-5.3: Variation in the density with increase in MGS weight percentage

Figure 5.4: EPR spectra of un-irradiated and irradiated composites (a) 0 kGy (b) 1.1 kGy (c) 2.2 kGy (d) 3.3 kGy

Figure-5.5: Variation in the HPP with increase in microwave power (square root)

Figure-5.6(b): Variation in the signal height (Hpp) increase in radiation dose (100 Gy-4000Gy)

Figure-5.6 (a): Variation in the signal height (Hpp) increase in radiation dose (2Gy-600 Gy)

Figure-5.7: Variation of fading of signal with increase in the storage time. Fading was expressed as the percentage of decrease in the signal intensity of the initial signal.

Figure-5.8: Variation in mass energy absorption coefficient of EVA and water with increase in energy

Figure-5.9: Variation in mass energy absorption coefficient of MGS and water with increase in energy

Chapter-6

Figure-6.1: XRD pattern of polycrystalline sample of BaSO₄:Eu annealed at different temperatures

Figure-6.2: TL glow curve for gamma irradiated BaSO₄: Eu

Figure-6.1.3: Photo Luminescence of BaSO₄-Eu at different annealing temperatures

Figure-6.4: ESR Spectra of Un irradiated Un doped and Europium doped BaSO₄

Figure 6.5(A): Changes in radical intensity of BaSO₄:Eu with temperature

Figure 6.5(B): Changes in radical intensity of un-doped BaSO₄ with temperature

Figure 6.6 (A): Power dependence - Un-doped BaSO₄

Figure-6.6: (B) Power dependence – Eu doped BaSO₄

Figure-6.7: Comparison between the dose responses of irradiated un-doped BaSO₄ and BaSO₄: Eu to different gamma doses

List of Tables

Chapter-1

Table-1.1: Interactions of photons with matter

Table-1.2-Materials and corresponding dosimetry technique

Table-1.3: Characteristics of ESR dosimetric system

Chapter-2

Table-2.1: Specifications of polymers used

Chapter-3

Table-3.1: Percentage deviation from Nielsen's model at different doses

Table-3.2: Effect of Bi₂O₃ on thermal degradation of PDMS

Table-3.3: Small amplitude oscillatory shear and dynamic thermo-mechanical properties of EVA copolymers and EVA/BS composites

Table-3.4: Parameters of phenomenological quantitative Kraus model fitting to non- linear oscillatory melt shear rheology (angular shear strain) and to solid dynamic mechanical analysis (uniaxial tensile strain) data of EVA/BS composites

Table-3.5: WLF parameters, fractional free volume and experimental and theoretical densities of pristine EVA copolymers and EVA/BS composites

Chapter-4

Table-4.1: Linear fitting parameters for PC/MR dosimetric films

Table-4.2: Reproducibility of relative change in absorbance at different doses (0.12 mM of MR /100g PC)

CHAPTER-1

INTRODUCTION TO INTERACTION OF RADIATION WITH MATTER AND DOSIMETRY

High energy radiation provides unique opportunities and finds wide application in various fields such as for material modification, medical diagnosis, therapy and also for industrial purposes. Several technologies and products have been developed using ionizing radiation and considerable efforts have been made to understand its effect on biological systems and materials. The chemical effects of radiation depend on the composition of matter and the amount of energy deposited by the radiation. High energy radiation can be classified into two groups particles: {charged (e^- , e^+ , α , etc) and uncharged particles (n)} and electromagnetic radiation (γ , X-ray). With an extensive use of radiation for various medical and industrial applications, it becomes imperative to have a better and complete understanding of radiation effects on materials for which advanced radiation dosimetric procedures should be developed. This chapter presents fundamental aspects of effect of high energy radiation on matter along with the different techniques used for characterizing defects induced by radiation and literature review.

1.1. Interaction of radiation with matter

Matter consists of atomic nuclei and extra-nuclear electrons. The radiation may interact with either or both of these constituents, depending upon the type, energy of the radiation and the nature of the absorbing medium (Table-

1.1). These interactions result in excitation and ionization of the absorber atoms in the matrix. Ultimately the energy transfer is manifested, partly as production of radicals and partly by dissipating energy in the form of heat. The ‘specific ionization’ [1] viz. the number of ion pairs formed per unit distance traveled in the medium is a measure of the rate of energy loss by the radiation due to ionization. To study the radiation effect in the medium, the linear rate of energy absorption in the medium, expressed in eV/A°, ‘**linear energy transfer**’ (LET) should be known. The interaction of gamma ray photons is qualitatively different from the corpuscular radiations. Such corpuscular radiations have definite ranges beyond which their radiation effects cannot be observed. However, the intensity of gamma rays can only be decreased and cannot be completely absorbed. The interaction of gamma ray with matter varies systematically with the electron density [1, 2], which is reflected as effective Z, of absorbing medium and with the energy of the gamma ray photon [3].

The gamma ray photons moving through the medium interact with the medium basically in three different ways:

- (i) Collision with atom as a whole proportional to Z
- (ii) Collision with an atomic electrons proportional to Z
- (iii) By radiative processes (Bremsstrahlung) proportional to Z^2 .

When the distance of closest approach of the photon is large compared to the atomic dimensions, the atom as a whole reacts, resulting in excitation or ionization of the atom (Soft collision). When the distance of closest approach of the photon is of the order of atomic dimensions, it interacts with one of the

atomic electrons, resulting in the ejection of electron from the atom with considerable energy known as knock-on (Hard collision). Hard collisions transfer a large amount of energy to the secondary electrons. When the secondary electron has Kinetic Energy (KE) large enough to cause ionization, from its own track, it is called delta ray (δ - ray >100 eV). For δ – rays of energy exceeding 10 keV, LET comes into play. Primarily the interaction of gamma radiation is of three types viz. Photo-electric effect, Compton scattering and Pair-production (Table-1.1, Figure-1.1a).

In Photo-electric process, a photon interacts with the absorber atom in which the photon completely disappears; an energetic photoelectron is ejected from the bound shells of the absorber atom [1, 3, 4]. Here the interaction with the atom as a whole, cannot take place with the free electron. The energy of the photoelectron is given by $E_{e^-} = h\nu - E_b$ where $h\nu$ is the energy of incident photon and E_b represent the binding energy of the electron in its shell. As the photoelectric process is predominant at lower energy, with the increase in the photon energy the probability of photoelectric effect decreases rapidly. When the energy of the photon is more than few hundreds of keV upto 1.5 MeV, the photon interaction is by Compton scattering [1, 3]. During this process, the photon undergoes an elastic collision with a loosely bound electron. During this, part of the energy is transferred to the electron. The directions of the scattered photon of lower energy and that of electron with respect to the incoming photon satisfy the laws of conservation of momentum. The probability of the Compton scattering process, in general, decreases with the increasing photon energy. Pair production

is the process of interaction of photon with matter, when its energy exceeds 1.02 MeV. The energy of the photon partly appears as the rest masses of two particles and partly as the kinetic energies of the electron E_e and positron E_p given by [1,4]

$$h\nu = E_e + E_p + m_0c^2 \quad (1.1)$$

It is obvious that the process cannot take place for $h\nu < 1.02$ MeV. The available energy in the kinetic energy form is divided almost equally between the two particles generated. Pair production process is always followed by annihilation of the positrons and in most cases, the formation of 0.51 MeV gammas. The probability of this process is proportional to Z^2 .

The energy dependence of the three processes in a typical absorber sodium iodide medium/detector is given in Fig. 1.1a. The relative importance of the three processes described above for different absorber materials and gamma ray energies is shown in Figure 1.1b. The line at the left represents the energy at which photoelectric absorption and Compton scattering are equally probable as a function of the absorber atomic number. The line at the right represents the energy at which Compton scattering and pair production are equally probable. Three areas in the figure thus define within which photoelectric absorption, Compton scattering and pair production are dominant.

1.2. Radiation Induced defects/effects in matter

The overall effect of radiation depends on the quantum of energy absorption from the incident radiation and the type of matter. The radiation dose

is therefore expressed in terms of the absorbed energy per unit mass of the medium/tissue. The external gamma radiation of a given energy flux delivers the absorbed dose to the material depending upon the point at which the absorbed dose is required and the elemental constitution of the absorbing medium [5]. For example, in case of living matter, bones of elemental constitution calcium and phosphorus absorb more energy from the photon per unit mass of medium than the soft tissues of elemental constitution C, O, N and H. One exposure unit (X unit) is defined as ‘the quantity of X or gamma radiation that produces ions carrying 1 coulomb of either charge per kilogram of air.

$$1 \text{ X unit} = 1 \text{ C/kg of air. } 1 \text{ X unit} = 34 \text{ Gy (in air).} \quad (1.2)$$

The operational definition of the exposure unit may be converted into a more fundamental unit of energy absorption per unit mass of air with single ion charge as $1.6 \times 10^{-19} \text{ C}$ and average energy dissipated per single ion pair in air as 34 eV. Gray, the unit of radiation dose, applicable to all types of ionizing radiation, used in radiation dosimetry is defined as ‘the amount of radiation energy deposited as 1 Joule per 1 kg of matter ($1 \text{ Gy} = 1 \text{ J/kg.}$). One rad is defined as ‘the amount of energy deposited as 100 ergs per gram of matter’ ($1 \text{ rad} = 100 \text{ ergs/gm.}$).

1.3. Quantification of radiation dose

Radiation dosimetry is an area of utmost interest to Health Physicists, Medical Physicists, dose rate reconstruction, computation and for accidental dose assessments during radiation incidences. This is also important during any planned high dose irradiation at industrial irradiators, radiation processing of

materials. A radiation dose measurement system must give signals that could be accurately and precisely measured. Besides, the radiation-induced signal as the radiation signature must have a well-defined and reproducible functional relationship with energy deposited in the matrix viz., absorbed doses of the ionizing radiation.

1.3.1. Essentials of a dosimetry system

The essentials for a system to qualify for dosimetry [3, 5, and 6] are:

1. The dosimetric signal should be linear or well defined, with linear dose – signal relationship, over an appreciable dose range.
2. The radiation-induced signal should have relatively high contrast with radiation dose and a good reproducibility of the radiation induced signal.
3. Well-characterized radiation induced signals that can be related to the dose or dose rate by established relationships with constant parameters.
4. The ingredients of the dosimeter, its various batches should remain stable, for periods for few weeks, during the period between irradiation and signal readout; the radiation-induced signal should remain stable with reproducibility.
5. Absence of environmental / dose rate effects and radiation special energy effects.

1.3.2. Techniques for dosimetric evaluation

1.3.2.1. Calorimetry

It is an absolute method of (reference) dosimetry. It finds application as a primary dosimetric standard for calibration purposes. Due to the radiant energy deposited in the substance, the material gets heated up. The rise in temperature

is a function of the energy deposited per unit mass of the substance. In calorimetry, the rise in temperature of the material due to irradiation is measured [7]. However, the rise in temperature is very less, $0.0024\text{ }^{\circ}\text{C} / \text{Gy}$, ($2.4 \times 10^{-3}\text{ }^{\circ}\text{C} / \text{Gy}$) can find applications only in cases of higher radiation doses. The materials and their corresponding dosimetric techniques are given in Table-1.2.

1.3.2.2. Fricke dosimetry

It is based on the assessment of the radiation induced ferric ion concentration at 305 nm, by spectro-photometry. The Fe^{+2} ions on irradiation get oxidized to Fe^{+3} ions, in the Fricke solution. The optical density (Fe^{+3} concentration) measured at 305 nm is used to calculate the absorbed dose. It is useful in the radiation dose range 40 Gy – 400 Gy [3,8,9].

1.3.2.3. FBX dosimetry

Spectrophotometric methods of radiation dose measurements are based on the light absorbing complexes. The chemical dosimetry uses aqueous sulphuric acid solution of ferrous sulphate, xylenol orange and benzoic acid. The free radicals present in irradiated material, oxidize Fe^{+2} to Fe^{+3} . Concentration of Fe^{+3} ions is quantified, by spectrophotometry, (Fe^{+2} ions on irradiation get oxidized) for estimation of the radiation dose.

1.3.2.4. Film badge dosimetry

A photographic film of ~200 microns thickness coated with ~12 microns thick emulsion act as the film badge dosimeter. The emulsion consists of silver halide in the matrix. The effect of nuclear radiation is reflected in the

film becomes darkened on exposure. The degree of darkening is related to the film density $D = \log_{10} (I_0 / I)$, where I_0 is the intensity of incident light and I is the intensity of light transmitted by the film, which in turn, is a measure of radiation dose. The film response to the radiation dose is found to be linear in $10^{-3}\text{Gy} - 10\text{ Gy}$ [10]. Though the system is a permanent record, the dosimetric technique was discontinued due to its non-reusable nature and environmental effects leading to ghost signal.

1.3.2.5. Thermally Stimulated Luminescence (TSL)

TSL dosimeters depend on the electrons trapped between the valence and conduction bands in the crystalline structure of matter [11-14]. The band structure in an insulator is normally described in terms of valence band and conduction bands separated from each other by a forbidden gap. The defects can create localized states at different depths. The trap depth i.e. the energy separation between localized levels (defects) and conduction band edge can be provided by TSL. The probability p per unit time that a trapped electron will escape from the trap is: $p = s e^{(-E / kT)}$, where E is the trap depth [thermal activation energy required to liberate a trapped charge] in eV, k is the Boltzmann constant, T is the temperature in K and s is the frequency factor in Hz. In first order kinetics, with the basic assumption that the electrons once released from the trap will undergo recombination rather than getting re-trapped, the number of trapped electrons 'n' is given by,

$$N = n_0 [\exp (-pt)] = n_0 [\exp \{-s \exp (-E / kT)\}]. \quad (1.3)$$

Where n_0 is the trapped electrons at time $t = 0$.

For a single trap depth, the first order kinetics, the TL intensity 'I' at any temperature is directly proportional to the rate of de-trapping.

$$I(T) = n_0 p \exp [-(s/q) \exp (-E/kT) dT] \quad (1.4)$$

Where q is the linear heating rate dT/dt.

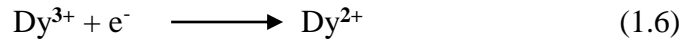
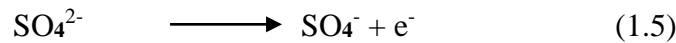
The TSL glow curves of first order are asymmetrical, while those of second order are symmetrical. These measurements give a reliable estimate of radiation dose.

As evident from the above mentioned techniques, different methods and different type of dosimetric systems can be designed depending on the radiation dose involved.

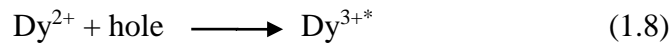
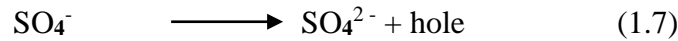
1.3.2.6. Thermo luminescent dosimetry (TLD)

Certain phosphor materials on irradiation produce defect centers, (electron-hole trap centers), that are stable at room temperature. However on heating, the electron-hole pairs recombine and get de-excited emitting photons in the visible range of electromagnetic spectrum [3,7,11-14]. The behavior can be depicted (for CaSO₄: Dy dosimeter) as here under:

On irradiation,



On heating,



The intensity of photon emission is a function of concentration of

radiation induced defects, in turn a function of irradiation / absorbed dose. This is a very sensitive technique (10^6 defects / cc.), useful for a wide range of dose from μGy – kGy level, and is used for personnel and environmental dosimetry. However, it is considered as a destructive technique as the signals get erased on heating the phosphor to the requisite temperature, for estimation of dose. It is a not a permanent record.

1.3.2.7. ESR dosimetry

The measurement of concentration of free radicals generated due to ionizing radiation yields the absorbed dose in a quantitative way. ESR relies on the direct measurement of free radical concentration generated in the dosimetric material as a consequence of deposition of energy by the ionizing radiation [2, 3, 6]. Free radicals in organic materials correspond to trapped electrons or homolytic rupture of covalent bonds depending on the quantum of radiant energy absorbed per unit mass of matter. Since, the concentration of paramagnetic defect centers is proportional to the dose delivered to the specimen; the signal intensity is used to calibrate the radiation dose delivered to the specimen in ESR dosimetry. Besides, ESR is a non-destructive, non-invasive method, highly sensitive technique (responsive for spin concentration $\geq 10^{13}$ / cc). The dose measurements can be repetitive with accumulated dosimetric signal and can be used at wide range of temperatures from 4K onwards [15-19]. ESR read-out technique is based on the quantitative measure of the absorption signal of irradiated dosimeter material.

1.4. Literature Survey

Radiation induced defects in alanine, an amino acid, have been extensively investigated. ESR dosimetry indeed has emerged as an important tool in high range radiation dosimetry of low and high LET ionizing radiation [17-24]. The dosimeter in powder form can be used and that dispenses with the angular positioning in the resonant cavity of the ESR spectrometer. The dosimetric response of alanine in the readout process is non-destructive; hence, cumulative dose measurement is possible. Besides, in the radiotherapy dose range, alanine – ESR dosimetry could find possible usage. Alanine dosimeter in powder form viz. α – alanine and other forms such as alanine-polystyrene material [18], alanine single crystals and alanine tablets with certain binders have been used for a variety of dosimetric studies. Alanine-ESR dosimeters are referred for usage by the IAEA [6], for standardization of irradiation dose at the various irradiator facilities. Alanine dosimeters have found applications even as postal dosimeters for inter-calibration of facilities. The dose response of ESR signal of irradiated alanine is reported to be independent of photon / beam energy in the range of 0.5 MeV – 3 MeV [25]. Thus, the alanine dosimeters could be used for dose determinations for inter-calibrations of gamma irradiators with Co^{60} source and gamma irradiators with Cs^{137} source or electron beam accelerators of beam energies upto 3 MeV. The gamma dose profile at different locations could be evaluated with selected parameters of the irradiation facilities using alanine-ESR dosimeters. In situ dose determinations could be assayed

using the alanine-ESR dosimeters at nuclear reactor beam columns, thermal shields with / without temperature and humidity. During the last 35 years, the precision of absorbed dose determinations by means of ESR spectrometry of irradiated alanine has considerably improved. It has been known for several years that the ESR spectrum of alanine has an excellent applicability for dosimetric purposes. It is reported that when 95% alanine tablets with certain binders were studied for dose inter-comparison with alanine paraffin dosimeters, an uncertainty of $\pm 1.1\%$ was observed for observed dose ~ 5 Gy and was found to have a precision better than $\pm 2\%$ at dose ~ 2 Gy [18].

Other than the alanine dosimeter used in the ESR technique, a variety of other materials have also been investigated for their suitability of application as ESR dosimeters in select ranges or as accidental dosimeter and retrospective dosimeters. The ESR spectroscopy using cotton fabric, human tooth enamel, dentine and bones has been reported to have wide dosimetric application [26-27]. It was used in the evaluation of personal dose and in individual retrospective dosimetry during a few radiation accidents. The signals from human tooth enamel are reported to be invaluable in assessing the absorbed dose of people exposed to radiation accidents. The measurement of radiation induced radicals originating from carbonate impurity of all tooth tissues [28] and bone by ESR technique has been reported to be useful. Thus, carbonate radical has been found to be of importance in ESR dosimetry. Experimental investigations have been carried out to compare by ESR technique the radiation sensitivity of biological and synthetic carbonated apatites [26-29]. It has been reported that the lower

detection limit for tooth enamel is 100 mGy, for dentine 300 mGy, for cementum 700 mGy and for synthetic carbonated apatite 1 Gy. The $\text{CO}_3^{\cdot-}$ center is reported to be stable, and accurate measurements could be possible even after 40 years of the radiation incident. However, this approach is reported to be applicable only, if the human teeth be readily obtained from the accident victims. A number of biological samples [29-30] on the potentially exposed persons have been reported to be evaluated for the feasibility study on the use of ESR dosimetric technique for accidental radiation exposure.

Effects of high energy radiation on properties of polymers such as Lucite, polyethylene, paper, wool, human hair and nail have also been investigated. Wool, human hair and nail have shown rapid decay of the ESR signal intensity, and were not found suitable for quantitative dosimetric study. Samples containing sugars [31] have been reported to have high sensitivity to radiation with the induced radicals in those materials as relatively stable. Fingernails, human hair and leather are reportedly promising for accidental dosimetry. The signal fading could be of use if the time interval between irradiation and ESR measurement is known. From extrapolation of the fading curves it should be possible to determine the dose using those substances. Sugar a suitable tissue equivalent dosimetric material has been reported [31] to have stable radiation signal, responding linearly with dose in 0.5 Gy – 10 Gy. Hence, sugar an inexpensive commodity, universally available in pure, uniform and homogeneous form, has ESR dosimetric applications in the form of silicone bound sugar pellet matrix.

Effect of radiation on the watch glass has been investigated [22 and references therein] dose response and the signal stability investigated through the ESR technique has been reported to have linearity of dose response in the range 2 Gy – 50 kGy with decay of about 20% in first 24 hour after irradiation and slower decay later, suggesting watch glass could be an ESR dosimetric material during accidental dose evaluations. The use of cotton clothing fabrics made up of natural cellulose polymer, a condensation product of glucose, when exposed to radiations has their macromolecules degraded and free radicals generated [26]. The dose response of cellulose has been reported to be linear in the range 7 Gy – 10^4 Gy, the fading could be considerably reduced by increasing the matrix crystallinity. Thus the ESR spectrum of the free radicals due to radiation in the cotton fabric could give an idea of dose in the few Gray to 10^4 Gray range.

The sample of magnesium lactate on gamma irradiation is found to produce radicals, measured by ESR technique in dose 0.1 Gy – 100 kGy range. The samples of magnesium lactate and samples of magnesium lactate doped with lithium lactate give ESR signals with dose response in 20 Gy – 100 kGy range [20]. The ESR signals of these dosimeter materials consist of light atoms with tissue equivalence and the radicals generated are stable at room temperature. The results indicate that the material could be a good ESR dosimeter for low as well as high dose ranges. Both undoped as well as Li- lactate doped Mg- lactate being light sensitive can be useful ESR dosimeters with an additional caveat to avoid direct light exposure. Radiation dosimetry was done by measuring free radicals induced in synthetic nano-structure hydroxyapatite (HAP) [32] using

EPR method. The HAP samples were synthesized via fluid body simulated method and were irradiated at different dose intervals and subsequently subjected to the EPR measurement. The effects of some EPR parameters were investigated as well. Variations of EPR signal intensities were constructed as peak-to-peak signal amplitude and were compared with alanine and bovine bone samples for two different dose ranges of Gy and kGy from dosimetric point of view. The results showed that the HAP samples were more useful for doses in Gy range. At kGy range doses the bone sample and alanine dosimeter showed a better ESR response.

Radiation-induced primary radicals generated in lithium formate [33], a material used in ESR dosimetry have been studied using electron paramagnetic resonance (ESR), electron nuclear double resonance (ENDOR) and ENDOR-Induced EPR (EIE) techniques. In this study, single crystals were irradiated with X-ray at 6-8 K and radical formation at these and higher temperatures were investigated. Periodic density functional theory calculations were used to assist in assigning the radical structures. Mainly two radicals were present at 6 K; the well-known $\text{CO}_2^{\cdot-}$ radical and a protonated electron-gain anion radical product. Hyperfine coupling tensors for proton and lithium interactions were obtained for these two radicals and show that the latter radical exists in four conformations with various degrees of bending at the radical center. Pairs of $\text{CO}_2^{\cdot-}$ radicals were also observed and the tensor for the electron-electron dipolar coupling was determined for the strongest coupled pair, which exhibited largest spectral intensity. Upon warming, both the radical pairs and the reduction product

decayed the latter apparently by a transient species. Above 200 K, the ESR spectrum occurred mainly due to the $\text{CO}_2^{\bullet-}$ (mono) radicals, which were previously characterized as the dominant species present at room temperature and which account for the ESR dosimetric signal.

Until very recently, analysis of bone biopsies of samples collected after surgery or amputation by ESR was considered as the sole reliable method for radiation dose assessment in hands and feet. ESR measurements in finger-and toe nail [30] have been considered for accident dosimetry for a long time. Human nails are very attractive biophysical materials because they are easy to collect and pertinent to whole body irradiation. Information on the existence of a radiation-induced signal in human nails has been reported almost 25 years ago. However, no practical application of ESR dosimetry on nails is known to date because, from an ESR perspective, nails represent a very complex material. In addition to the radiation-induced signal (RIS), parasitic and intense signals are induced by the mechanical stress caused when collecting nail samples (mechanically induced signals—MIS). Moreover, it has been demonstrated that the RIS stability is strongly influenced not only by temperature, but also by humidity. Most studies of human nails were carried out using conventional X-band microwave band (9.5GHz). Higher frequency Q-band (35GHz) provides higher spectral resolution which allows obtaining more detailed information on the nature of different radicals in human nails. Four different MIS signals and five different signals specific to irradiation with ionizing radiation have been identified [34]. The most important outcome of this work is the identification of a stable RIS

component. In contrast with other identified (unstable) RIS components, this component is thermally stable and not affected by the physical contact of finger nails with water. The discovery of stable radiation-induced radical(s) associated with the RIS component mentioned opens a way for broad application of EPR dosimetry in human nails.

The electron spin resonance technique has been used to study the production of long-lived radicals in glycine, valine, aspartic acid and glutamic acid. The yield of radicals as a function of dose was measured, using a 3 MeV electron beam accelerator very high dose rate. In all cases saturation was observed at high doses (in the megarad range). The yield vs. dose curves were analyzed in terms of exponential functions and some possible explanations put forward. Absolute values of the yield per unit dose, as well as the saturation values, were calculated, and possible sources of error in these values were discussed.

Sucrose, the main component of table sugar, present in nearly every household and quite radiation sensitive, is considered as an interesting emergency dosimeter [31]. Another application of radiation-induced radicals in sugars is the detection of irradiation in sugar-containing foodstuffs. The complexity of electron paramagnetic resonance (ESR) spectra of radicals in these materials, as a result of many hyperfine interactions and the multi-compositeness of the spectra of individual sugars, complicates dose assessment. A thorough understanding of the ESR spectrum of individual irradiated sugars is desirable when one wants to reliably use them in a wide variety of dosimetric applications. Recently, the dominant room temperature stable radicals in irradiated sucrose have been

thoroughly characterized using ESR, electron nuclear double resonance (ENDOR) and ENDOR-induced ESR. These radicals were structurally identified by comparing their proton hyperfine and g-tensors with the results of Density Functional Theory calculations for test radical structures. The results indicate that the major part of the dosimetric spectrum can be understood in terms of three dominant radicals, but as-yet unidentified radicals also contribute in a non-negligible way.

Taurine/EVA [35] rods (3×10 mm) have been prepared by a simple technique in the laboratory where taurine powder was mixed with a molten mixture of paraffin wax and ethylene vinyl acetate (EVA) copolymer. The binding mixture EVA/Paraffin does not present interference or noise in the ESR signal before or after irradiation. The rods show good mechanical properties for safe and multi-use handling. An ESR investigation of radiation induced radicals in taurine rods revealed that there are two types of radicals produced after exposure to gamma radiation. ESR spectra were recorded and analyzed – also the microwave power saturation and modulation amplitude were studied and optimized. Response of taurine to different radiation doses (1.5–100 kGy) was studied and found to follow a linear relationship up to 100 kGy. Radiation induced radicals in taurine persisted and showed a noticeable stability over 94 days following irradiation. Uncertainties associated with the evaluation of radiation doses using taurine dosimeters were discussed and tabulated. It was found that taurine possesses good dosimetric properties using ESR spectroscopy at high doses in addition to its simple spectrum. Radiation-induced free radicals

in hydrated magnesium sulfate, which are thought to be present on the surface of Europa, one of the Jovian moons, have been studied by electron spin resonance (ESR). ESR signals of both atomic hydrogen (H.) at $g = 2.0023$ and sulfite radical ($\text{SO}_3^{\bullet-}$) at $g = 2.0029$ are observed [7]. Table 1.3 presents characteristics of some of ESR based dosimetric systems.

1.5 Outline of work

Literature survey pointed out the paucity of work on the radiation defects generated in multiphase polymer systems and their composites, though these systems have significant applied and theoretical interest in different applications. It was also clear that there is a pressing need of developing new cost-effective, user friendly and efficient dosimeters for the routine use. The objective of this work included synthesis of different polymer based multiphase systems, investigate the effect of radiation on them and explore their applications in radiation dosimetry and in radiation shielding/radiopacity.

Melt compounding was used to synthesize different polymer composites. These compounded formulations were explored for ESR and optical dosimetry. Optical dosimeters were extensively characterized for the morphological characteristics; dye doping, linearity, color indices, fading and reproducibility. Several formulations were developed for EPR dosimetry and an extensive characterization of radicals generated, linearity, fading, reproducibility and of polymeric attributes such as melt flow index, hardness and mechanical properties were conducted. Polymer composite formulations were also developed for radiopacity and shielding applications and were extensively characterized by

rheological, morphological and physico-mechanical analysis to reveal complex interplay of the morphology, the crystallinity, and the copolymer architecture.

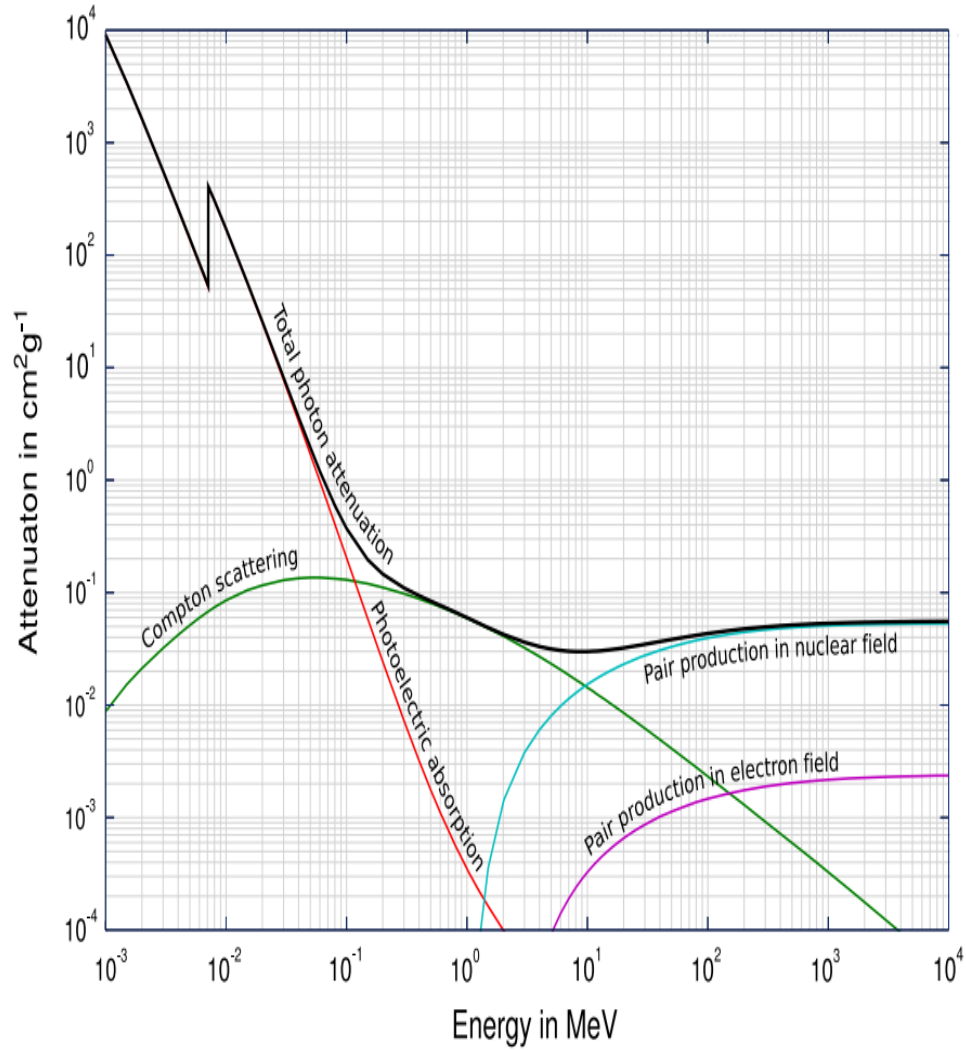


Figure 1.1a: Energy dependence of the various gamma ray interaction processes in sodium Iodide medium.

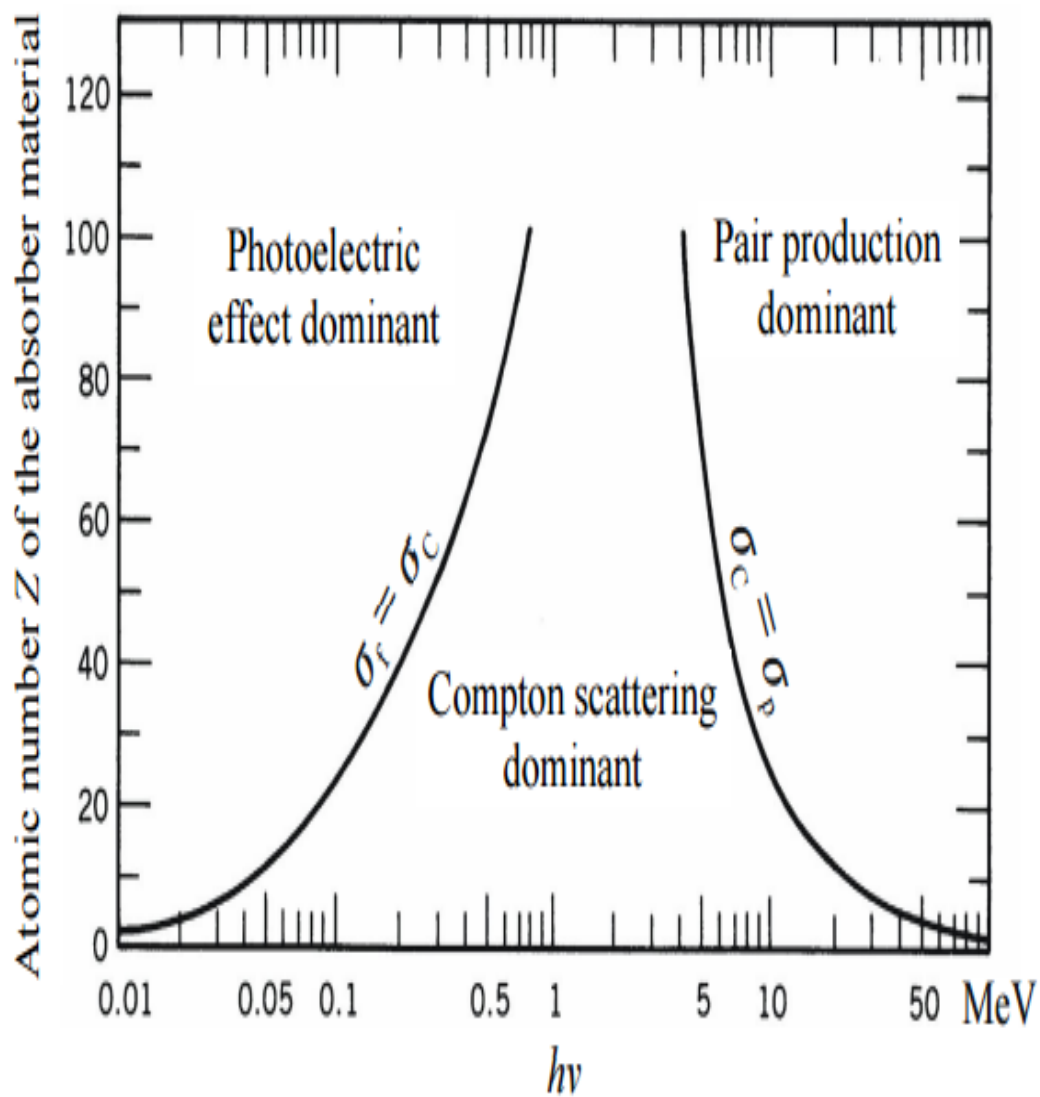


Figure 1.1b: Relative importance of the three principal interactions of photons in matter

Table: 1.1: Interactions of photons with matter

Type of interaction/ Interaction with	Absorption	Scattering	
		Elastic	Inelastic
Atomic Electrons	PE effect $\sim Z^4$ (low energy) $\sim Z^5$ (high energy)	Rayleigh $\sim Z^2$	Compton $\sim Z$ (low energy)
Nucleons	Photonuclear reaction (γ, n), (γ, p), (γ, f) $\sim Z$ (Energy ≥ 10 MeV)	Elastic Nuclear Nuclear Resonance scattering	
Electric field of surrounding charged particle	Pair production $\sim Z^2$ (KE > 1.02 MeV)	Delbruck scattering	

Table: 1.2-Materials and corresponding dosimetry technique

Matter	Radiation effects	Dosimetric technique
Water	Heat generation	Colorimetry
In-Organic Crystals	Defects/Radicals	Luminescence/ ESR
Organic	Scintillation	Luminescence
Polymer	Radicals/Color change	ESR/Optical
Glass	Radicals/Color change	ESR/Optical
Solution	Chemical Change	Optical
Gas	Ionization	Current

Table 1.3: Characteristics of ESR dosimetric system

No.	Dosimeter	Form	Dose range (Gray)	Signal stability
1	Alanine	Powder, pellet, films	$1-10^5$	<150°C
2	Tooth enamel	Powder	$0.1-10^3$	<200°C
3	Sugar	Pellets	0.5-10	<160°C
4	Medicinal Tablets	Pellets, powder	0.5-20	<160°C
5	Cotton	Pieces	$2-6 \times 10^3$	---
6	Watch glass	pieces	2-50	<200°C
7	Quartz	Powder	$100-10^7$	<300°C
8	Corn	Powder	$200-2 \times 10^3$	---
9	Dentine	Powder	0.3-7	<160°C
10	Granite	Powder	$100-10^5$	<300°C
11	Magnesium lactate	Powder	$0.1-2 \times 10^3$	---

CHAPTER-2

EXPERIMENTAL METHODOLOGY AND CHARACTERIZATION TECHNIQUES

2.1. Introduction

The present work deals with the investigation of radiation induced defects in matter generated due to gamma irradiation and the utilization of resultant radiation induced changes for material modification and for the absorbed dose quantification [1-3]. Various novel polymer matrices were synthesized by melt, shear or solvent compounding [36-38] and were irradiated with different doses of gamma radiation. Thereafter, radiation induced changes were characterized by universal tensile testing [38], rheology, cross-linking density measurements, Scanning Electron Microscopy (SEM), Atomic Force Microscopy (AFM), X-ray Diffraction (XRD), Fourier Transform Infrared Spectroscopy (FTIR), Elemental Analysis (EA), Thermal Analysis (TGA and DSC), UV-visible Spectroscopy and Electron Spin Resonance (ESR). The present chapter discusses the principles and methodologies involved in these studies.

2.2. Materials

Ethylene-Propylene Diene Monomer rubber (EPDM), Poly-chloroprene Rubber (PCR), and Ethylene Vinyl Acetate (EVA) were procured from M/s Polystar

chemicals, Mumbai. Specifications of the polymers used in the study are mentioned in Table 2.1. All solvents and reagents used in the study were from Aldrich chemicals, USA and were of AnalaR grade. Freshly prepared distilled water was used in the synthesis of thermoplastic starch and in other experiments.

2.3. Sample Preparation

Blends and nano-composites used in the study were prepared by mixing ingredients (Polymer composites) on a two-roll laboratory mill or in a Brabender Plasticodar. The homogeneous mix was cut into small pieces and compressed into sheets of size $12 \times 12 \text{ cm}^2$ of different thicknesses in range 1-4 mm using compression-molding machine at 150 kg/cm^2 pressure for 2 minutes at 130°C (403 K).

2.4. Gamma radiation source

A gamma radiation source, Gamma Chamber GC-5000, supplied by the Board of Radiation & Isotope Technology (BRIT), Mumbai, India was used for irradiation of reaction mixture solutions. Gamma chambers mainly consist of a set of stationary ^{60}Co source placed in a cylindrical cage surrounded by a lead shield. The shielding of suitable thickness is provided around the source to keep external radiation field well within the permissible limits. The material for irradiation is placed in an irradiation chamber located in the vertical drawer inside the lead flask. The drawer can be moved up and down with the help of a motorized driven system, which enables precise positioning of the irradiation chamber at the center of the radiation field. ^{60}Co radioisotope emits two photons of energy 1.33 and 1.17 MeV each with 100 % yield.

2.5. Dosimetry

Radiation dosimetry is the term applied to describe the process of quantification of radiation effects [1,33] of a given radiation source. Any device or process employed to carry out dosimetry is known as a radiation dosimeter. A prior Knowledge about the amount of radiant energy absorbed per unit mass and distribution of the absorbed energy in any absorbing material is essential in order to quantify the physical, chemical or biological changes induced by the radiation exposure in the said material due to the ionizing radiation.

Some of the important terms associated with the process are:

(i) Absorbed dose: It is defined as the average amount of energy absorbed per unit mass of the irradiated material. The SI unit for the absorbed dose is Joules/kilogram (J.kg^{-1}), termed as gray (Gy) [1, 39]. The older unit is Rad quantified as 100 ergs per gram of matter ($1 \text{ rad} = 0.01 \text{ Gy}$).

(ii) Absorbed dose rate: The radiation dose absorbed per unit time is termed as the absorbed dose rate. The unit used for absorbed dose is Gy.s^{-1} or Gy. h^{-1} .

Dosimeters can be classified into two categories viz. primary dosimeters and secondary dosimeters. Primary dosimeters involve physical measurement of any parameter such as rise in temperature, measured by a thermocouple / calorimeter, ionization produced in a gas or the electrical charge due to ionization, carried by a beam of charged particles of known energy [1, 39]. Secondary dosimeters are those dosimeters whose response to radiation has to be calibrated against a primary dosimeter. These include Fricke dosimeter, nylon film dosimeter, solutions of various dyes, Perspex dosimeters etc [1]. The choice of a dosimeter

for a particular application depends on certain factors such as, (i) state of the system, (ii) dose range to be monitored and (iii) nature of radiation.

The absorbed dose measured by the dosimeter will represent the dose absorbed by the sample only when the following conditions are satisfied: (a) the dosimeter as well as the sample are both homogeneous, (b) both have similar size, density and atomic composition, and (c) both are irradiated under identical conditions. The simple and convenient method to achieve these conditions is to use equal volumes of dilute solutions of both sample and dosimeter, and irradiate them in turn under identical conditions. However, since exact duplication of reaction conditions is very often not attainable, certain approximations and relations are used to determine the absorbed dose for a given sample. For electromagnetic radiation like ^{60}Co gamma-rays, the absorbed dose in the dosimeter (D_d) and sample (D_s) are related by the equation (2.1).

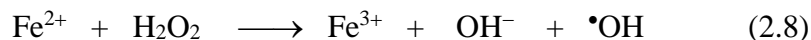
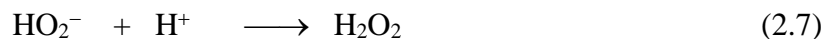
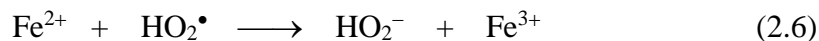
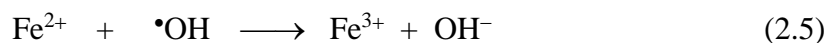
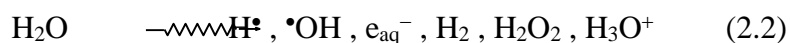
$$D_s = \frac{D_d \times (Z/A)_s}{(Z/A)_d} \quad (2.1)$$

Where, Z/A is the ratio of the atomic number (Z) to the atomic weight (A) for an element and the ratio of the sum of the atomic numbers of the element present to the molecular weight for a compound. Fricke dosimeter, ESR dosimeter and thermo luminescent dosimeter (TLD) are among the commonly used dosimetric techniques and are discussed below.

2.5.1. Fricke dosimetry

The dose rate of gamma chamber GC-5000 was measured by Fricke dosimeter

[9] prior to carrying out the experiments. The basic principle underlying Fricke dosimeter is the radiation induced oxidation of ferrous ions to ferric ions in acidic aqueous solutions in the presence of oxygen. The standard Fricke dosimeter [3] comprises of an aerated solution of $1.0 \times 10^{-3} \text{ mol dm}^{-3}$ ferrous ammonium sulphate, $1.0 \times 10^{-3} \text{ mol dm}^{-3} \text{ NaCl}$ and 0.4 mol dm^{-3} sulphuric acid (pH= 0.46). The reactions involved in the Fricke dosimeter are summarized under reactions (2.2) – (2.8).



The yield of ferric ion is related to the primary radical and molecular yields by Equation (2.9)

$$G_{(\text{Fe}^{3+})} = 2G_{(\text{H}_2\text{O}_2)} + 3 \left[G_{(e_{\text{aq}}^-)} + G_{(\text{H}^\bullet)} \right] + G_{(\text{OH}^\bullet)} \longrightarrow \quad (2.9)$$

Since each molecule of hydrogen peroxide oxidizes two ferrous ions by reactions (2.8) and (2.5), while the reducing radicals each oxidize three ferrous ions by sequential reactions involving HO_2^- , H_2O_2 and OH^- respectively [9]. The number of moles of Fe^{3+} ions (M) produced upon irradiation is determined by absorption

spectro-photometry employing Beer's law (7.8) ($A = \epsilon \cdot c \cdot l$) at 304 nm with $(\text{Fe}^{3+}) = 2205 \pm 3 \text{ dm}^3 \text{ mol}^{-1} \text{ cm}^{-1}$ and $\epsilon(\text{Fe}^{2+}) = 1 \text{ dm}^3 \text{ mol}^{-1} \text{ cm}^{-1}$ at 25°C. The $G(\text{Fe}^{3+})$ value accepted for electron and photon radiation in the range 1 to 30 MeV is 15.5 (or, $1.606 \times 10^{-6} \text{ mol dm}^{-3} \text{ J}^{-1}$) at 25°C and the density of Fricke dosimeter solution is 1.024 gm ml^{-1} .

The Fricke dosimeter can be used to determine accurately dose only up to 400 Gy, because of depletion of oxygen in the system beyond this dose $G(\text{Fe}^{3+})$ does not remain constant. Fricke dosimeter is independent of dose rate between $0.2 - 2.0 \times 10^6 \text{ Gy s}^{-1}$. A modified version of Fricke dosimeter, also called as super Fricke dosimeter, containing $10^{-2} \text{ mol dm}^{-3}$ ferrous ions, oxygenated but without any sodium chloride, is independent of dose rate up to absorbed dose rates of the order of 10^8 Gy s^{-1} . The upper limit of absorbed dose that can be measured using a super Fricke dosimeter is 2.0 kGy. Lead attenuators of suitable thickness were used for reducing the dose rates.

2.5.2. ESR dosimetry

2.5.2.1. Theory of ESR Spectroscopy

The Bruker ESR spectrometer used in the present studies is shown in Figure- 2.1. Electron Spin Resonance (ESR) spectroscopy is based on the electronic Zeeman levels transitions (Figure-2.2) occurring due to the spin flip of unpaired electrons under the influence of an external magnetic field [40- 42]. It is a highly efficient technique for detecting and characterizing the presence of unpaired electrons in any substance. Important theoretical aspects of ESR technique are discussed below.

When a molecule or a compound with an unpaired electron is placed in a strong magnetic field, the spin of the unpaired electron can align in two different ways creating two spin states, $m_s = \pm \frac{1}{2}$. The alignment can either be along the direction (parallel) to the magnetic field which corresponds to the lower energy state $m_s = -\frac{1}{2}$ or opposite (antiparallel) to the direction of the applied magnetic field $m_s = +\frac{1}{2}$. The two alignments have different energies and this difference in energy lifts the degeneracy of the electron spin states. The energy difference is given by:

$$\Delta E = E_+ - E_- = h\nu = g\beta H \quad (2.10)$$

h = Planck's constant ($6.626 \times 10^{-34} \text{ J s}$),

ν = the frequency of radiation,

β = Bohr magneton ($9.274 \times 10^{-24} \text{ J T}^{-1}$),

H = strength of the magnetic field in Tesla,

g = the g-factor.

During the experiment the values of h , ν , and β does not change and g value decrease as H increases. The g-factor is a unit less measurement of the intrinsic magnetic moment of the electron, and its value for a free electron is 2.0023. The concept of 'g' can be roughly equated to that of chemical shift in NMR. ESR spectrum is the absorption of microwave frequency radiation plotted against the magnetic field intensity.

2.5.2.2. Working principles of ESR:

In an ESR experiment, the field of spectrometer magnet is swept linearly to excite some of the electrons in the lower energy level to the upper energy level while the sample is exposed to fixed microwave irradiation. The free or the unpaired

electrons have a small magnetic field and orient themselves parallel to the larger field produced by the spectrometer's magnet. At a particular magnetic field strength, the microwave irradiation will cause some of the free electrons to “flip” and orient against the spectrometer's magnetic field. This separation between the lower and the higher energy level is exactly matched by microwave frequency. The condition where the magnetic field and the microwave frequency are “just right” to produce an ESR resonance (or absorption) is known as the resonance condition detected by the spectrometer. ESR spectroscopy can be carried out either by,

1. Varying the magnetic field and holding the frequency constant or
2. Varying the frequency and holding the magnetic field constant (as is the case for NMR spectroscopy).

Typically, in a commercial spectrometer works by varying the magnetic field and holding the frequency constant. ESR spectrometers working at frequencies ranging from several hundred MHz to several hundred GHz are in use- 1-2 GHz (L-band) and 2-4 GHz (S-band), 8-10 GHz (X-Band), 35 GHz (Q-band) and 95 GHz (W-band). The most commonly used ESR spectrometer is in the range of 9-10 GHz (X-band).

Measuring a CW-ESR spectroscopy can be influenced by various parameters, both instrumental and experimental. The significant aspect of the measurement is to get a high resolved ESR spectrum from a low concentration sample of interest which is dependent on the sensitivity and resolution of the spectrometer. Microwave bridge and resonator governs the sensitivity of the signal. Magnet,

Magnet field controller, magnet power supply and signal channel control the resolution of the spectrum obtained.

2.5.2.3. Application of ESR:

Only direct method to detect the presence of free radicals and to identify the paramagnetic species provides information on:

1. Dose measurements for sterilization of medical goods and foods
2. Molecular structure near the unpaired electron.
3. ESR spectra line shape gives insight to dynamic processes molecular motions or fluidity.
4. Probes the structure of “active sites” in metallo proteins.
5. Detection of irradiated foods, and the dating of early human artifacts.

2.5.2.4. Methods to record ESR spectra:

Continuous wave method: the sample is irradiated continuously with microwave radiation of fixed frequency while the magnetic field is slowly swept and the microwave absorption is measured for each field position.

2.5.2.5. Splitting in ESR spectra

There are two main kinds of splitting that can be produced in ESR spectrum viz. electronic splitting and hyperfine splitting. The electronic splitting is due to the presence of more than one unpaired electron in atom or molecule of the specimen. The hyperfine splitting is due to the interaction of the unpaired electron with the magnetic moment of the nuclei of the atoms or molecules of the specimen.

2.5.2.6. Electronic splitting

When there is more than one unpaired electron per atom or molecule with triplet state system with two unpaired electrons in the molecular orbital, the spin angular momentum give rise to total spin quantum number of $S = 1$. The combined angular momentum and magnetic moment orient as a unit in applied magnetic field, with three possible orientations corresponding to $M_s = +1, 0$ or -1 . In the absence of any electric field, the unpaired electrons have equal energies in zero applied magnetic field, while their energies diverge as shown in Figure.2.2, when an external field is applied.

If the electromagnetic radiation of frequency corresponding to the energy difference between $+1$ and 0 level or the 0 and -1 level, be applied, the resonant absorption for each of the two allowed transitions for $M_s = \pm 1$ taking place result in a single absorption line.

2.5.2.7. Hyperfine splitting

The interaction of the unpaired electron with the magnetic moment of the nucleus of any atom results in the hyperfine splitting (Figure-2.3). If the unpaired electron is confined to an atomic orbital associated with only one atom, the interactions will be with the magnetic moment of the nucleus of that particular atom. In case of the unpaired electron moving in molecular orbital with several atoms, the hyperfine splitting is due to the interaction with several nuclei result in the complicated pattern. In a typical case of electron moving around a nucleus having nuclear magnetic moment, I gives rise to $(2I + 1)$ resolved components that differ from each other by an integer. In case of

electron moving around a multi-nuclear arrangement, the electron interacts with several nuclei at once. In the multi-nuclear pattern with 'n' nuclei having identical nuclear magnetic moment. I, the number of components are $(2nI + 1)$. These components are not identical, but are different in intensities given by the binomial coefficients.

2.6. Thermally stimulated luminescence

The defects produced by high energy radiation can lead to the generation of electrons and holes [13, 14] in the matrix. If band gap is high enough to forbid the recombination of holes and electrons, their concentration can be correlated with absorbed dose. Thermal or optical stimulation of such traps can allow the recombination and release the stored energy by emission of photons. Luminescence intensity associated with this process can be quantified and correlated with the absorbed radiation dose.

Thermally stimulated luminescence (TSL) is among the easily amenable modes for studying the thermally stimulated electron-hole recombination process (Figure-2.4) in non-metallic solids subjected to external gamma and X-ray irradiations or internal alpha and/or gamma irradiations in actinide-doped phosphors. The energy stored due to irradiation, when released on electron-hole recombination, partly goes in radiative processes giving out luminescence and partly in non-radiative pathways. The radiative part, luminescence, is referred to as thermally stimulated luminescence (TSL), or thermo luminescence (TL). In this chapter it will be referred to as TSL, as this is a more appropriate way of describing this phenomenon. For the occurrence of this phenomenon the presence

of activators in the form of doped impurities is an important prerequisite. In actinide-doped solids, the actinide ions play a multiple role: as a source of irradiation, activators of luminescence, electron/hole traps and in some cases electron/hole recombination centres. The experimental observation of TSL in the simplest form consists of monitoring the emission of light from an irradiated substance as a function of temperature. The resulting curve containing one or more peaks of light emission at different temperatures is referred to as a TSL glow curve. TSL and other trap level spectroscopy techniques monitoring the release of the trapped charge carriers into either the conduction or valence band and subsequent capture by recombination centres during a dynamic heating process, provide information about traps regarding their activation energies, thermal escape rates, etc. Over the past forty years or so a number of methods have been developed for obtaining these parameters from TSL and thermally stimulated current (TSC) peaks.

2.7. Characterization techniques

2.7.1. Crosslinking Density

The molecular weight between cross-links (M_c) [43-44] was estimated using the following relation, based on the theory initially proposed by Flory and Rehner,

$$\bar{M}_c = -V_1 \rho_p \frac{\varphi_p^{1/3} - 1/2\varphi_p}{\ln(1 - \varphi_p) + \varphi_p + \chi \varphi_p^2} \quad (2.11)$$

where, V_1 is the molar volume of the solvent, ρ_p is the polymer density and φ_p is the volume fraction of the polymer in the swollen matrix. χ is the Flory–Huggins

interaction parameter between solvent and polymer which can be calculated using following relation

$$\chi = \beta + \frac{V_1}{RT} (\delta_s - \delta_p)^2 \quad (2.12)$$

where δ_s and δ_p are the solubility parameters of the solvent and the polymer, b is the lattice constant, R is the universal gas constant and T is absolute temperature.

2.7.2. Optical Microscopy

Colorimetric parameters of the dosimeter [45- 47] were measured by reflectance measurement using a Minolta CM-3600D Spectrophotometer (Konica Minolta Sensing, Inc., Osaka, Japan). The reflectance of whole visible spectrum (360 to 780 nm) was recorded at wave length interval of 10 nm. D₆₅ lamp was used as reference light source and the detector was fixed at an angle of 10°C with respect to the light source. The equipment was calibrated before use with a standard white tile and a black box for 100 and 0% reflectance, respectively. The data was analysed using JAYPAK 4808 software (Quality Control System, Version 1.2).

2.7.3. UV-Visible Spectrophotometer:

The absorbance changes were measured using a Shimadzu UV-2500 spectrophotometer at λ_{\max} of absorbance or transmittance, depending on the dosimeter absorption [9,47]. For each data point, four measurements were made and average value was reported as relative change in the absorbance.

The absorbance behavior of any material can be explained in terms of the Beer Lambert's Law. The absorbance value (A) depends on nanoparticle concentration

(c), path length (l) of measuring cell and extinction coefficient of materials.

$$A = \epsilon cl \quad (2.13)$$

2.7.4. FTIR spectrophotometer

The FTIR spectra of samples were recorded in ATR mode using diamond single reflectance ATR assembly in FTIR spectrometer (Affinity-1, Shimadzu, Japan) using resolution of 4 cm^{-1} and with data acquisition run of 25 scans for each sample. FTIR gives information regarding the structure and functional groups of a given molecule. More importantly, FTIR analysis is useful for conducting analysis of polymer composition and molecular structure.

2.7.5. Thermo gravimetric analysis (TGA)

The non-isothermal thermo gravimetric measurements were carried out with TGA/DSC1 system with gas controller system (GC100) from Mettler Toledo, Switzerland, to determine the thermal degradation behavior of Gamma radiation cured PCN films. For TG experiments $\sim 10\text{ mg}$ of the powder sample was taken in alumina crucible and heated in temperature range of 35 to 850°C at heating rate of $10^\circ\text{C.min}^{-1}$ under inert dynamic high purity nitrogen atmosphere at a flow rate of 50 ml min^{-1} .

TGA gives important information regarding the thermal degradation behavior of polymers and composite materials. Any changes in the thermal behavior of a material on incorporation of a filler can be detected using this technique. The residual weight observed in case of certain polymer nano

composite materials can also be indirectly used for predicting the flame retardant behavior of the material.

The basic requirement for TGA is a precision balance with a pan loaded with the sample, and a programmable furnace. The furnace can be programmed either for a constant heating rate, or for heating to acquire a constant mass loss with time. The TGA instrument continuously weighs a sample as it is heated. As the temperature increases, various components of the sample are decomposed and the weight percentage of each resulting mass change can be measured. Results are plotted with temperature on the X-axis and mass loss on the Y-axis.

2.7.6. Differential scanning calorimetry (DSC)

Glass transition temperature (T_g) of the samples was determined by a differential scanning calorimetry (DSC) using DSC 823e system from Mettler-Toledo, Switzerland. For all experiments ~10 mg of the sample was taken in standard aluminum pan and heated to 250 °C at heating rate of 20 °C.min⁻¹ followed by cooling to -50 °C at cooling rate of 20 °C.min⁻¹, and then again heated to 250 °C at heating rate of 20 °C.min⁻¹. All the cooling and heating cycles were carried out under inert dynamic high purity nitrogen atmosphere at a flow rate of 50 ml min⁻¹. The T_g values of samples were estimated from the second heating cycle.

2.7.7. Scanning electron microscopy (SEM)

The surface morphologies of samples were investigated by SEM analysis using VEGA MV2300T/40 (TS 5130 MM) microscope (TESCAN) at acceleration voltage of 5kV. SEM images of the cross-section of the nano-

composite coatings were taken at 10kx magnification, after the gold coated fractured coating films were fixed vertically on to a conducting steel stub surface using conducting carbon paste.

SEM involves the scanning of the sample surface with an electron beam of accelerating voltage $< 50\text{kV}$. The secondary or backscattered electrons collected by the detector are analyzed for obtaining the final image. SEM provides information about the topography and morphology of the sample and it can attain upto 1,00,000x magnification with a resolution of $\sim 1.5\text{ nm}$.

2.7.8. Atomic Force Microscope (AFM)

AFM measurements were performed using an NT-MDT solver model P47 instrument (Russia) with $50\mu\text{m}$ scanner head and silicon nitride tip in contact mode. The sample for AFM measurement was prepared by depositing a dilute solution of silver nanoparticles on a glass slide and allowing it to dry in a Laminar flow hood.

2.7.9. Radiopacity and mass attenuation coefficients

Radiopacity of different composites was tested on a diagnostic X-ray machine. The samples of different thickness were placed on the radiological sheet. The X-ray was operated at 120 kV_p and the gray scale of the x-ray scan was digitized using Image J image processing software (NIH, USA). Mass attenuation coefficients of the composites were calculated from the data mentioned in NIST Report (NIST-IR-5632).

2.7.10. Viscoelastic properties

Dynamic thermo-mechanical analysis (DMTA) measurement was

performed on an MCR 102 Rheometer (Anton Par, Austria) using Solid Rectangular Fixture (SRF) or with Universal Extensional Fixture (UXF). Samples dimensions were 20 mm x 10 mm x 1 mm (l x w x t) for all samples. Temperature sweep was done from -100 °C to 30 °C to monitor storage modulus in glass and rubbery stages, at 1 Hz frequency and 1% strain. Rheology measurements were performed on an MCR 102 Rheometer (Anton Par, Austria) at different angular frequencies using a parallel plate fixture. Samples dimensions were 12.5 mm (radius) and 1 mm (thickness). All measurements were conducted in the linear viscoelastic regime. Time-temperature (t-T) superimposition (TTS) was conducted on polymer melts for pristine polymers as well as on their composites. N₂ atmosphere was maintained to avoid oxidative degradation. Frequency sweep measurements were conducted at 1% strain and strain sweep experiments were conducted at 1 Hz frequency. A series of composites with same VA content but different BS content and vice versa were tested.

2.7.11. Mechanical Properties

For tensile strength measurements at least five dumbbell shaped specimens were cut from blend sheets using a steel die. Thickness of the samples was determined to the nearest of 1 mm. Tensile strength and elongation at break were measured by INSTRON universal testing machine as per the ASTM D 412.

2.7.12. X-Ray Diffraction (XRD)

XRD patterns were recorded using a Philips X-ray diffractometer PW 1710 (Almelo, Netherlands) using mono-chromatized CuK α radiation from an X-

ray generator operated at 30 kV & 20 mA. Lattice constant and lateral crystal size were calculated for blends and nano-composites from the XRD data. Bragg equation (equation 2.14) was used to calculate the lattice distance ($d_{hkl}, \text{\AA}$)

$$d_{hkl} = \frac{\lambda}{2 \sin \theta_{hkl}} \quad (2.14)$$

where λ is 1.541 \AA and θ_{hkl} represents the Bragg angl. The lateral crystal size l_{hkl} (\AA) was calculated by Scherrer formula given by

$$l_{hkl} = \frac{\beta \lambda}{f_{hkl} \cos \theta_{hkl}} \quad (2.15)$$

Where structure factor β is taken as 1 and f_{hkl} is the full width at half maxima of the respective crystal plane reflection.

2.7.13. Physical Properties

Density of polymer films was determined by displacement method (ASTM D792-08). Density in kg m^{-3} was estimated by using density balance from M/s AND, Japan (Least count 0.00001 g) using suitable liquids. The wetting liquids selected were of lower density than that of polymer sheet under investigation. Melt flow index was determined as per the ASTM D2839-05 standard. However, for some nano-composites and blends nano-composites, due to their low melt viscosity 10 kg weight was used, with proper normalization. Hardness was measured in accordance with ASTM D2240 using durometer (Asha-testers, Blue-steel Eng. (P) Ltd, India) and expressed in shore A.

2.8. Summary

High energy radiation induces a variety of changes in the material. Quantification of radiation induced radicals, the irradiation dose imparted and

estimation of mechanical properties and thermal properties of irradiated material is essential to understand the high energy radiation induced defects in a matrix. Fricke dosimetry and ESR dosimetry are the gold standard for dose quantification. Mechanical properties, X-ray studies, thermal properties and crosslinking density measurements provide important information on the effect of high energy radiation on the basis of induced effects.



Figure-2.1: BRUKER ESR spectrometer

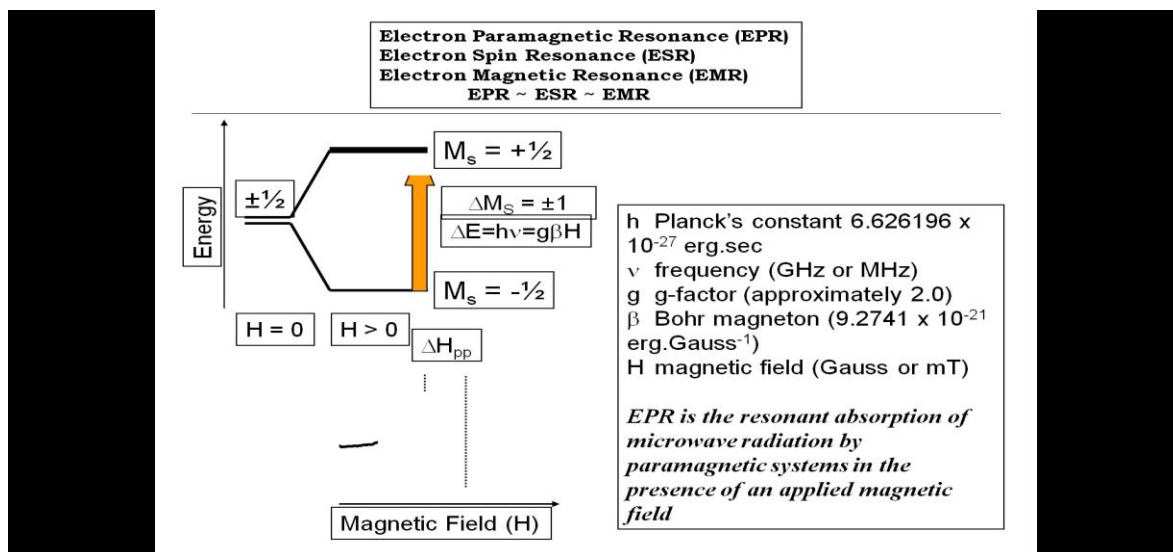


Figure 2.2: Basic electron resonance and Electronic Zeeman splitting

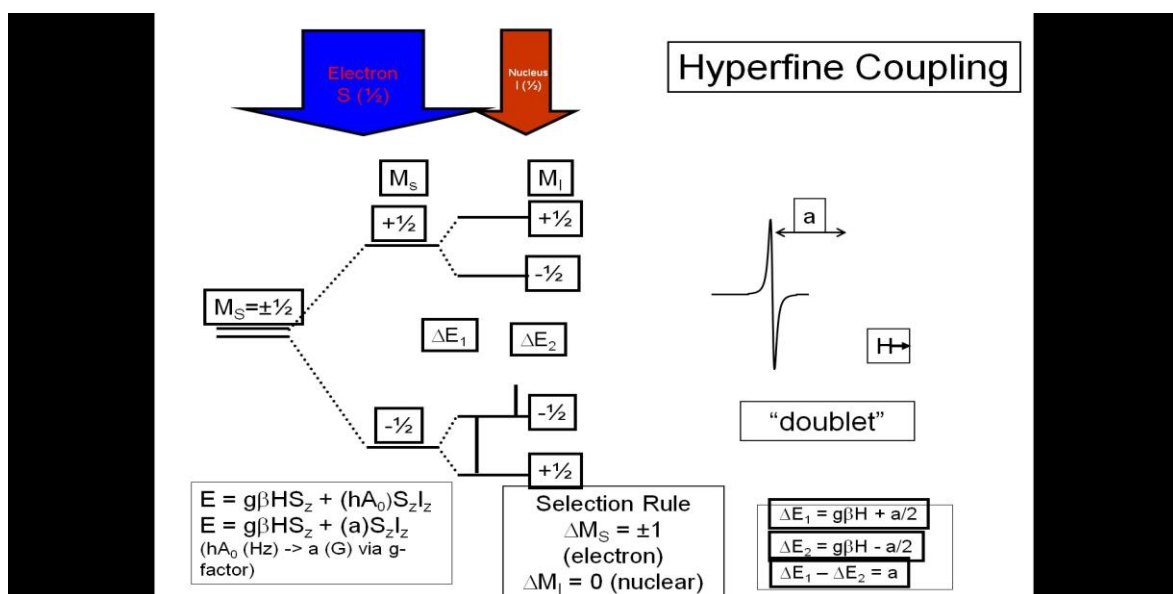
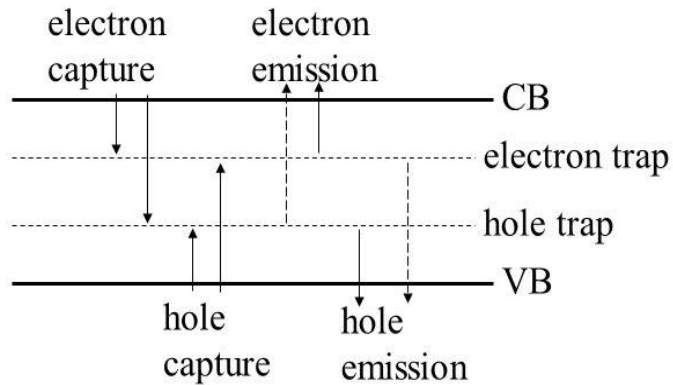


Figure-2.3: Hyperfine Coupling

Possible electronic processes



thermal (electron) emission probability: $e_n = \frac{\sigma_n v_n N_c}{g} \exp \frac{-E_t}{kT}$

"emission rate" [s^{-1}]

capture probabilities: $P_{c_n} = n \sigma_n v_n = n c_n$

$c_{n,p}$: "capture coefficients [$cm^3 s^{-1}$]" $P_{c_p} = p \sigma_p v_p = p c_p$

trap parameters: E_t (thermal activation energy), σ_n and σ_p resp. c_n and c_p

Figure-2.4: TSL electronic process

Table 2.1: Specifications of polymers and fillers used

Name	Specifications
EPDM	Ethylene content 55%; Diene: Ethylidenenorbornene (4%) Specific gravity: 0.87; Mooney viscosity ML1+4: ~60 (120°C)
EVA	Vinyl content: 18%, Specific gravity: 0.91, Melting point: 88
PDMS	Poly-dimethyl siloxane procured from M/s DJ silicone, China Hardness = 60; density= 1.13±0.05 g/cc
Bismuth oxide	Bismuth Oxide (purity >99%) was purchased from M/s Loba Chemie Pvt. Ltd., India. Melting Point- 817°C
Magnesium sulfate	Purity 99%, Aldrich chemicals, USA, Melting Point- 1124°C
Barium sulfate	Purity 99%, Aldrich chemicals, USA, Melting Point- 1580°C
Chloroprene rubber (PCR)	Specific gravity :1.23, Mooney viscosity ML1+4 : ~40 (120°C)

CHAPTER-3

EFFECT OF HIGH ENERGY IRRADIATION ON POLYMER COMPOSITES, SYNTHESIS OF RADIO OPAQUE COMPOSITES AND RADIATION SHIELDS

3.1. General Introduction

Medical implants are artificial devices that are used to replace, support or enhance damaged biological structures. With the recent improvement in public health, nutrition, and medicine, the world has witnessed a remarkable enhancement in the average human life expectancy, increasing in the fraction of the elderly population. This, in turn, has increased the use of medical implants in orthopedic, cardiovascular, gynecological and urological disorders. Polymers are an attractive choice for medical implants; however, the invisibility of polymer implants to the diagnostic x-rays scans is a challenge to monitor its function and integrity and often necessitates expensive radiology imaging such as MRI [48-52] or invasive surgery. To enable monitoring of implants by routine medical X-ray scans, there is a pressing need to impart radiopacity in polymer based implants without compromising their physical, mechanical or biological behavior. Additionally, there is an increasing need to improve structural characteristics of polymer based implants to expand their durability, mechanical strengths and other desired attributes [53-56]. As the use of drug-eluting stents (DES) and control release implants is increasing for therapeutic applications, the polymer based medical implants are gaining more acceptance and so is the radiopacity of such medical implants to monitor DES placement and performance [56]. In addition to radiopacity, flexible lead free high energy

radiation shielding materials are required for applications in the environments where exposure to radiation is unavoidable namely nuclear fuel processing, radiopharmaceuticals preparation and space exploration. High energy radiation is very effective in developing cross-linked structures in polymer and therefore can be useful in the development of cross-linked polymer composites to give potential applications in radiation shielding. Minimization of hazardous additives and the finished-stage processing are among the prime advantages of the radiation cross-linking over conventional processes; however, the extent of cross-linking has been shown to be a function of structure of parent matrices, dose rate, dose and irradiation ambience, making the effect of radiation highly material specific. Additionally, the effect of high energy radiation in terms of cross-linking, attenuation and polymer composites is not fully understood. The situation is further complicated as the understanding of highly filled polymer systems is not yet mature and very few studies have provided the detail of rheological, filler aggregation-disaggregation dynamics, mechanical and morphological attributes of such composites [57-60]. These factors accentuate the need of developing polymer composites with excellent radiopacity and physico-mechanical characteristics and underscore the paucity of studies on morphology, filler aggregation dynamics and radiopacity correlation in such composites.

Bismuth oxide has advantages of significantly lower toxicity over conventional lead based particulate fillers [58-61]. Barium sulphate (BaSO_4) is also a promising material in radiopacity / shielding applications. To improve the

radiological efficacy of diagnostic X-rays, BaSO₄ is often injected in patients with severe trauma to the chest, abdomen or spinal cord. Polymer / BaSO₄ composites are also being investigated for radiation protection in fluoroscopy – guided interventions, and clinical trials are going on for testing the efficacy of such matrices [61-62]. BaSO₄ has also been used for improving radiopacity of polypropylene and polyethylene [63] and indeed claimed to be the first radiopaque filler used in medical formulations. However, to obtain a high radio contrast, high BS loadings are needed, which limits the use of BaSO₄ in such application despite its many obvious advantages such as white color, inexpensiveness and availability [64]. Most importantly, one of the biggest impediments in designing radiopaque implants based on polymer/BS composites is the marked deterioration of mechanical properties on high filler loading, making such composites unsuitable for applications in interventional radiology, cardiology or in implants.

Ethylene vinyl acetate (EVA) is a transparent copolymer, which has potential to offer a variety of property combination through variation of ethylene and vinyl acetate (VA) ratio. EVA based composites offer a new class of materials with benefits of engineering plastics depending on filler characteristics and elastomeric properties [65]. Mechanical properties and favorable biocompatibility of EVA make it one of the promising non-biodegradable implant materials [66]. Recently, it is demonstrated the controlled release of quinolinic acid from EVA based brain implants, causing behavioral and neuro-anatomical alterations in a rodent model of Huntington's disease [67]. For

contraception, an implantable rod of EVA is currently approved in Europe, Canada and Indonesia for the delivery of etonogestrel, and is awaiting Food and Drug Administration (FDA) approval in US [68-69]. EVA based DES are used to treat a coronary artery disease [70-73]. Furthermore, EVA based composites are also explored for applications demanding cranioplastic analogs and integrated cartilage/bone joint prosthesis [74-75]. EVA based radiopaque formulations are expected to be of high medical significance; furthermore, since they are thermoplastics they can be used in various forms such as standalone objects, laminates, coating or adhesives. On the other hand, PDMS (poly-di-methyl-siloxane), has higher atomic number (Z_{eff}), better heat resistance, acts as an electrical insulator, and shows better chemical stability than common carbon based polymers, making PDMS/Bi₂O₃ composites excellent choice for flexible radiation shields (76-77).

The present chapter describes the effectiveness of radiation induced cross-linking of poly-di-methyl-siloxane (PDMS) / bismuth oxide (Bi₂O₃) composites. Efforts have also been made to understand how radiation cross-linking affects the physico-mechanical properties of the composites and the attenuation characteristics of the composites were studied. Attenuation of gamma radiation from ²⁴¹Am was also investigated. ²⁴¹Am is an important radioisotope produced during ²³⁸Pu processing [76-77]. It has applications in radiography, radiotherapy and for heat and power generation in spacecrafts. Many of such applications demand, flexible light weight shielding material, mainly for the 59.9 KeV gamma radiation emitted from ²⁴¹Am. Furthermore, highly radiopaque yet

flexible EVA/ BaSO₄ composites were also developed by tailoring polar/non-polar ratio and crystalline content in the composites *via* varying copolymer ratio. It was hypothesized that such an approach can entail flexible, radiopaque and melt processable formulations. This chapter also elucidates mechanical, crystalline, rheological and thermo-mechanical properties of these filled systems. Morphology of the composites was monitored using atomic force microscopy, scanning electron microscopy and phase imaging.

3.2. Material and methods

3.2.1. Materials

Polydimethylsiloxane procured from M/s DJ silicone, China (Hardness=60; density= 1.13±0.05 g/cc) containing vulcanizator 2, 5-dimethyl-2, 5-bis (tert-butylperoxy) hexane (0.65%) was used as such. Bismuth Oxide (purity >99%) was purchased from M/s Loba Chemie Pvt. Ltd., India. Xylene used for swelling and crosslinking density determination was of AnalaR grade (Purity > 99%) and was procured from local supplier M/s SD Fine chemicals, Mumbai.

EVA of different vinyl acetate content [12% (MFI 8g/10 min at 190°C); 25% (MFI 19 g/10 min at 190°C); 40% (MFI 57g/10 min at 190°C)] and barium sulfate (BS) (Purity 99%) was procured from Aldrich chemicals, USA.

3.2.2. Sample preparation

A series of PDMS/Bi₂O₃ composites were prepared by mixing the components homogeneously in Brabender Plasti-Corder® Lab-Station at 120°C at 50 rpm for 20 minutes. Weight of the components were carefully chosen by considering the bulk density of the components to get volume contribution with respect to the constituents. The homogeneous mix was cut to small pieces and compressed into sheets of size 10x10 cm² of different thicknesses in range 1-4 mm using compression-molding machine at 150-kg/cm² pressure for 20 minutes

at 120°C. Sample designation for samples used in this study are designated by $C_{\text{Bi2O3}}^{\text{Dose}}$ (wt%) (superscript shows the radiation dose and subscript shows wt% of Bi₂O₃).

A series of EVA/Composites were prepared by mixing the components in Brabender plasticordar at 120°C, 30 rpm for 25 minutes. The weight of the components was carefully chosen by considering the bulk density of the components to get volume contribution with respect to the constituents, assuring proper filling of the mixing chamber. The homogeneous mix was cut into small pieces and compressed into sheets of size 12x12 cm² of different thicknesses in range 0.5-1.5 mm using a compression-molding machine at the pressure of 150 kg/cm² for 5 minutes at 150°C. Sample compositions and designations have been defined as VA_XBS_Y where X denotes the percentage of vinyl acetate (VA) content and Y denotes BScontent.

3.2.3. Radiation source

Irradiation was carried out under aerated condition using a gamma chamber 5000 (GC-5000) having Co-60 gamma source supplied by M/s BRIT, India. The dose rate of the gamma chamber was ascertained to be 1.7 kGy/h by Fricke dosimetry prior to irradiation of samples.

3.2.4. Physico-mechanical properties

For tensile strength measurements at least five dumbbell shaped specimens were cut out from nano-composite sheets using a sharp edged steel die of standard dimensions. The thickness of the samples were determined to the nearest of 0.1 mm. The tensile strength and elongation at break were measured using a universal testing machine supplied by M/s HEMETEK, Mumbai, INDIA

at crosshead speed of 100 mm/min at room temperature. Density of the samples was determined by displacement method in accordance with ASTM D792-08.

3.2.5. Viscoelastic properties

Dynamic thermo-mechanical analysis (DMTA) measurement was performed on an MCR 102 Rheometer (Anton Par, Austria) using Solid Rectangular Fixture (SRF) or with Universal Extensional Fixture (UXF). Samples dimensions were 20mmx10 mmx1mm (l_xw_xt) for all samples. Temperature sweep was done from -100°C to 30°C to monitor storage modulus in glass and rubbery stages, at 1 Hz frequency and 1% strain. Rheology measurements were performed on an MCR 102 Rheometer (Anton Par, Austria) at different angular frequencies using a parallel plate fixture. Samples dimensions were 12.5 mm (radius) and 1 mm (thickness). All measurements were conducted in the linear viscoelastic regime. Time-temperature (t-T) superimposition (TTS) was conducted on polymer melts for pristine polymers as well as on their composites. N₂ atmosphere was maintained to avoid oxidative degradation. Frequency sweep measurements were conducted at 1% strain and strain sweep experiments were conducted at 1 Hz frequency. A series of composites with same VA content but different BS content and vice versa were tested.

3.2.6. Sorption studies

For the sorption studies, radiation cross-linked nano-composites were Soxhlet extraction at elevated temperature for 12 h to extract any sol content using xylene. The insoluble gel part was then dried initially under room conditions and later under vacuum at 40°C. The dried composite thus obtained was cut into

uniform square pieces (1 cm²) using a sharp edged die and used for swelling studies. Pre-weighed samples were placed in a 200-mesh stainless steel compartment and immersed in excess of solvent at the desired temperature. The swollen samples were periodically removed, blotted free of surface solvent using laboratory tissue paper, weighed on an analytical balance (accuracy 0.00001 g) from M/s AND, India, in stopper bottles and returned to the swelling medium. Measurements were taken until the samples attained constant weight.

3.2.7. Thermo gravimetric analysis

Thermal stability of the samples was investigated by recording thermograms in the temperature range of RT-600°C in air at a heating rate of 10°C/min using Netzsch thermal analyzer [Model: STA 409 PC LXXX]; 100mL/min carrier gas flow rate was used for all the measurements. Alumina crucibles were used as sample/reference holder.

3.2.8. Scanning electron microscopy (SEM), Atomic force microscopy (AFM) and x-ray diffraction (XRD)

The morphology of composites with EVA with different vinyl content was investigated using a scanning electron microscope (Model PS-230, Pemtron, S. Korea). The cryofractured specimen was used to monitor dispersion of BS and interface. XRD patterns were recorded using a Philips x-ray diffractometer PW 1710 (Almelo, Netherlands) using the monochromatized CuK_α radiation from an x-ray generator operated at 30 kV and 20 mA. Atomic force microscopy (Easyscan 2, Nanosurf AG, Switzerland) was used for topographic studies of

composites in contact mode as well as in phase imaging mode.

3.2.9. Radiopacity and mass attenuation coefficients

Radiopacity of different composites was tested on a diagnostic X-ray machine. The samples of different thickness were placed on the radiological sheet. The X-ray was operated at 120 kV_p and the gray scale of the x-ray scan was digitized using ImageJ image processing software (NIH, USA). Mass attenuation coefficients of the composites were calculated from the data mentioned in NIST Report (NIST-IR-5632).

3.3. Results and discussion

3.3.1. Cross-linking density of the PDMS/bismuth oxide composites

In figure 3.1, variation in the cross-linking density with filler weight fraction has been plotted in the dose range 100-400 kGy. The cross-linking density was determined by estimating the molecular weight between cross-links (M_c) using the following relation, which is based on the theory initially proposed by Flory and Rehner [78-79] and can be presented as

$$\bar{M}_c = -V_1 \rho_p \frac{\phi_p^{1/3} - 1/2 \phi_p}{\ln(1 - \phi_p) + \phi_p + \chi \phi_p^2} \quad (3.1)$$

where V_1 is the molar volume of the solvent, ρ_p is the polymer density; ϕ_p is the volume fraction of the polymer in the swollen matrix and χ is the Flory–Huggins interaction parameter between solvent and polymer, which can be calculated using following relation

$$\chi = \beta + \frac{V_1}{RT} (\delta_s - \delta_p)^2 \quad (3.2)$$

where, δ_s and δ_p are the solubility parameters of the solvent and the polymer, β is the lattice constant, R is the universal gas constant and T is absolute temperature. φ_v was calculated using following relation

$$\varphi_p = \frac{(w_d - fw_i)/\rho_p}{(w_d - fw_i)/\rho_p + w_s/\rho_s} \quad (3.3)$$

where w_s and ρ_s are the weight and density of the solvent respectively; f is filler weight fraction and w_d and w_i are initial and dried weight respectively. The cross-linking density has been reported as $1/2M_c$. Two interesting observations were that for a fixed Bi_2O_3 content, the cross-linking density increased with absorbed dose and for a fixed dose cross-linking density was strong function of Bi_2O_3 content in the composite. Highest cross-linking was observed at a dose of 400 kGy over the entire composition range. The cross-linking increased up to 10 % Bi_2O_3 loading, remained almost constant till 50 wt % Bi_2O_3 and decreased thereafter. The increase in cross-linking extent with increase in dose and Bi_2O_3 content indicates synergistic effect of filler induced physical cross-linking and radiation vulcanization, especially when filler is of reinforcing type as reported for some other systems earlier [79-81]. Such effects have been attributed to reduction in free volume due to the physical cross-linking rendered by the reinforcing fillers. These processes might affect cross-linking mechanism, by influencing the migration and distribution of radiolytic species.

To understand the effects of Bi_2O_3 loading on the free volume of the composites, density of the composite was estimated. The density of composites is expected to change with Bi_2O_3 loading owing to substantial difference between the densities

of the polymer and Bi₂O₃. Density is also expected to vary with radiation cross-linking or degradation; though relative change may be smaller. The variation in the density with the Bi₂O₃ weight fraction has been shown in figure 3.2. Densities of the PDMS/Bi₂O₃ composites increased significantly with increase in Bi₂O₃ loading. Initially the increase was linear followed by non-linear increase at higher loading. The density of the composites can be predicted by the rule of mixture or in terms of mass fractions depicted by following equations

$$\rho_{ct} = \rho_f V_f + \rho_m V_m \quad (3.4)$$

$$1/\rho_{ct} = w_f/\rho_f + w_m/\rho_m \quad (3.5)$$

where ρ_{ct} is the theoretically determined density of composites whereas ρ_f, ρ_m are the densities of the Bi₂O₃ and the PDMS respectively; V_f, V_m are the volume fractions and w_f & w_m are weight fractions of the Bi₂O₃ and PDMS respectively. The theoretical values determined from the equations have also been plotted in the Figure 3.2. It can be seen that the experimental values perfectly matched with the theoretical values up to 50 wt % Bi₂O₃ content, beyond which slight negative deviation (highlighting increase in the free volume) was observed. The change in void fraction calculated using following relation (ρ_{ce} being experimentally determined density) is presented in inset of the Figure 3.2.

$$V_v = \frac{(\rho_{ct} - \rho_{ce})}{\rho_{ct}} \quad (3.6)$$

At lower Bi_2O_3 loading, low but consistent reduction in void fraction was observed. Such change was possible only if Bi_2O_3 was reinforcing PDMS matrix. At Bi_2O_3 loading > 50 wt %, increase in void volume fraction was observed. This reversal of trend may be attributed to the agglomeration of the Bi_2O_3 at higher loading, as commonly observed in polymer composites [82-83]. With the increase in dose, no significant change in density was observed suggesting cross-linking does not affect the free volume much. These results partly explain the observed variations in the cross-linking density. Initially as the fillers lead to the reduction in the void volume radical migrations and interactions are expected to be affected. The reduction in free volume may lead to the formation of X type of cross-linking rather than Y type crosslink. In the compositions with significant agglomeration, such effects are expected to be minimal as the possibility of a radical finding another radical on the neighbouring macromolecular chains is reduced due to the increase in the space occupied by Bi_2O_3 particles within the composite matrix. In addition to the agglomeration, Bi_2O_3 particles may also block the gamma radiation and act as energy sink. This gamma energy otherwise would be effective in generating radicals, which would contribute to cross-linking of the matrix. To further understand the effect of incorporating, Bi_2O_3 into PDMS matrix polymer filler interaction was investigated using Kraus equation.

3.3.2. Filler interaction in PDMS/bismuth oxide composites

The most important parameter in determining the mechanical properties and radiation cross-linking behaviour of the composites is the type and extent of

polymer-filler interaction. Polymer filler interactions in the composites were studied using Kraus plot obtained using equation

$$\frac{V_{ro}}{V_{rf}} = 1 - m \left(\frac{\phi_f}{1 - \phi_f} \right) \quad (3.7)$$

where V_{ro} is the volume fraction of the polymer in the swollen rubber, V_{rf} , volume fraction of polymer in the swollen filled system and ϕ_f is the volume fraction of the filler in the filled nano-composite. Swelling behaviour of the composites irradiated to different doses has been presented in Figure 3.3. It can be seen that saturation swelling is affected by both radiation dose and filler loading. The difference between the samples irradiated to dose of 100 kGy and 200 kGy was not much, but composites irradiated to 400 kGy showed significantly lower swelling even for unfilled polymer. This difference in swelling extent may be attributed to reduced pore size due to radiation cross-linking and to the steric hindrances to the diffusion of solvent molecules imposed by Bi_2O_3 particles. To access the polymer filler interaction, V_{ro}/V_{rf} was plotted against $\phi_f/(1-\phi_f)$. A linear profile with negative slope obtained suggested high reinforcement by filler. The polymer-filler interaction parameter C (Kraus constant) was calculated using the Kraus equation (equation 3.8) by putting “ m ” value obtained from plotting suitable parameters of equation (3.7) (Inset figure 3.3)

$$C = \frac{m - V_{r0} + 1}{3(1 - V_{r0}^{1/3})} \quad (3.8)$$

The negative slope for nano-composites (Inset figure 3.3) implied positive polymer filler interaction. The C value for the system was found to be 1.3, indicating a high reinforcement of the matrix. This suggests that Bi₂O₃ loading up to 150 wt% would provide best mechanical properties for Bi₂O₃/PDMS composites. This observation was well supported by the observed mechanical properties of the composites.

3.3.3. Mechanical properties of PDMS/bismuth oxide composites

Reinforcing fillers and radiation induced cross-linking both are expected to improve the mechanical properties of polymers. The elongation at break of the composites with increase in Bi₂O₃ fraction as a function of absorbed dose has been plotted in Figure 3.4. Elongation at break (EB) decreased sharply up to 10 wt% Bi₂O₃ loading, remained almost constant for 10-50 wt% Bi₂O₃ and decreased sharply later. With increase in radiation dose, the elongation at break further decreased. This decrease was clearly due to formation of intermolecular and intermolecular cross-linked network which will impede the chain slippage and reduce elongation at break [79]. It was interesting to note that with increase in radiation dose, EB trend remained almost the same; however the decrease in EB after 50 wt% loading was less sharper in case of irradiated samples.

Figure 3.5 shows trend of young modulus of the composites. The young modulus increased both with the absorbed dose as well as with the Bi₂O₃ loading. To understand the effect of filler induced reinforcement and radiation cross-linking, Nielsen's macroscopic model was employed. The model considers filler and

matrix moduli, volume fraction of each component and packing density of the fillers. It can be described as,

$$\frac{E_c}{E_m} = \frac{1 + ABV_f}{1 - \psi BV_f} \quad (3.9)$$

$$A = k_E - 1 \quad (3.10)$$

$$B = \frac{\frac{E_f}{E_m} - 1}{\frac{E_f}{E_m} - A} \quad (3.11)$$

$$\psi \cong 1 + \frac{1 - \phi_m}{\phi_m^2} V_f \quad (3.12)$$

where, E_f, E_c, E_m are the modulus of the filler, composite and matrix respectively, k_E is the Einstein's coefficient. The constant A is a function of the aspect ratio and orientation of the filler. The factor B is used to take into account the relative difference in the modulus of the two components. The term ϕ_m is related to the packing fraction of the filler in the composite and ψ is related to the volume fraction of the filler. A modified ψ equation (equation 3.13) has also been used in the study as it has been reported to be quite effective in several similar systems.

$$\psi = 1 + \frac{V_m}{\phi_m} [\phi_m V_f + (1 - \phi_m) V_m] \quad (3.13)$$

The values of ϕ_m and A were taken as 0.7045 and 1.5 respectively and the modulus of Bi_2O_3 was taken as 32 GPa. Table 3.1 shows variation of the Nielsen's model values from the experimental data, considering ψ and modified ψ parameters. It is clear from the table that at lower filler loading (up to 30 wt%), the deviation was much less for composites irradiated to 400 kGy than those irradiated to dose of 100 kGy. A plausible explanation for this might be formation of a continuous network of Bi_2O_3 within the composite matrix at higher filler loading, negating the effect of filler induced physical cross-linking as well as of the grafting of polymer chains on to filler [80,83-85]. Such a distribution might increase the modulus considerably and lead to deviation from the model. A complete morphological analysis of the system is essential to conclusively prove this hypothesis; however based on the results of this study, morphological dependence of the physico-mechanical and other properties can be safely claimed. Cross-linking density of the composites as discussed in the previous section was also found to be significantly high at 400 kGy and was found to depend on filler fraction.

3.3.4. Thermo-gravimetric analysis of PDMS/bismuth oxide composites

Thermal stability of the polymer is an important characteristic that can get affected by filler loading [57,86]. Thermal stability of the composites having different weight fractions of Bi_2O_3 was investigated by thermo-gravimetric analysis and thermal decomposition profiles of the polymer containing 0, 10%, 30% and 70% of Bi_2O_3 are shown in Figure 3.6. It can be seen that all composites exhibited two-step decomposition. First in temperature range 350-

500°C and second, the major one in temperature range 500-650°C. The first peak (as shown in the derivative profile of weight loss curve), can be attributed to the thermal decomposition of lower molecular weight products formed from residuals left during the synthesis of PDMS [58]. It can be seen that the onset of degradation varies with increase in filler loading, for both the steps (Table 3.2). The onset temperature of the second step was found to increase from 451°C to 491°C as loading of Bi₂O₃ increased from 0 to 70 wt%. It may be noted that second peak represents the degradation of main chain of PDMS and is important in reflecting thermal stability of the Bi₂O₃/PDMS composites. Degradation of PDMS may involve terminal group or the breakage of main chain. The filler addition is expected to affect degradation mechanism by increase the rigidity of the matrix, by acting as a gas barrier or by scavenging the radicals generated during thermal decomposition. As discussed in sections above, as Bi₂O₃ is reinforcing filler, it would improve localized rigidity of the polymer chains in addition to affecting thermal conductivity and barrier properties.

3.3.5. γ -attenuation by PDMS/bismuth oxide composites

Attenuation of gamma radiation from ²⁴¹Am by the PDMS/Bi₂O₃ composites irradiated to different doses has been shown in the inset of Figure-3.7. It represents reduction in the counts by a 1.5 mm thick sheet of the composites containing different amount of Bi₂O₃. It can be seen that with the increase in radiation dose, not much difference in the shielding efficiency was observed, though with the increase in filler loading the decrease in counts was substantial. As with the increase in radiation dose, the specific density of the

composites was not much affected (discussed in section on cross-linking density of composites), irradiation was not expected to affect the shielding efficiency much. On the other hand, the significant attenuation of γ -radiation on addition of such high atomic number and density additive was very much expected depending on composite composition. The attenuation of ^{241}Am gamma ray by PDMS/ Bi_2O_3 composites was calculated using this relation for the composites having different weight fractions of Bi_2O_3 .

$$\% \text{Attenuation} = \frac{N_o - N_t}{N_o} \times 100 \quad (3.14)$$

Figure 3.7 clearly shows that 10 wt% of Bi_2O_3 loading could show attenuation of 50% and on increasing loading to 30 wt % ~70% attenuation could be achieved. It is worth mentioning here that the rise in the density in this range was only about 40% over the unfilled PDMS. In the recent past, several polymer composites have been explored to develop flexible shields for high-energy radiation. In literature, there are contradictory reports regarding effect of size of filler on attenuation efficiency of composites. Lead oxide was used by as filler in epoxy matrix and improvement in the mass attenuation coefficient was observed with filler loading, though particle size didn't affect shielding response. Whereas, size dependent radiation-stability and shielding characteristics of the Bi_2O_3 nano-particles embedded in polymer matrices against diagnostic x-rays has also been reported. Harish et al, investigated the shielding properties of lead oxide filled polymer matrix against ^{137}Cs gamma radiation, showing noticeable attenuation at 50 wt% loading [59] The major aspect that determines practical application of these composites is the high attenuation along with good physico-

mechanical and thermal characteristics. The % attenuation and mechanical properties of the radiation cross-linked $\text{Bi}_2\text{O}_3/\text{PDMS}$ composites suggest that the composites can be used in designing flexible shield materials. Further analysis is however needed to precisely determine mass attenuation coefficients and correlate with them filler dispersion, loading and polymer-filler interactions [60-61,87].

3.3.6. Dispersion, interface, and crystallinity of EVA/ BaSO_4 Composites

Morphological features of the composites were investigated using the scanning electron microscopy and phase imaging atomic force microscopy. To understand the changes in the dispersion state and the interfacial interaction between BS and EVA, with different VA content, cryo-fractured surfaces of composites were imaged by SEM. In SEM (Fig. 3.8), pillow shaped microdomains were found to be distributed in all micrographs and were assigned to BaSO_4 crystals [88]. A distinct pattern of fracture, dispersion and interface adhesion was observed for each composite. The $\text{VA}_{12}\text{BS}_{50}$ exhibited a relatively brittle fracture; whereas, $\text{VA}_{40}\text{BS}_{50}$ showed ductile failure with no impressions of fracture morphology. Variation in the failure mechanism with a change in VA content can be attributed to the differences in the intrinsic properties of the EVA such as variation in amorphous content, polarity and overall macromolecular architecture. However, it is also suggestive of weak bonding between polymer and filler. The poor interfacial adhesion was also evident from the pulling out of BS domains; $\text{VA}_{12}\text{BS}_{50}$ showed either pulled out or completely embedded morphology; in contrast, $\text{VA}_{40}\text{BS}_{50}$ exhibited embedded domains and the most

distinct pattern was observed in VA₂₅BS₅₀. As observed with interfacial variation in terms of pulling out, the dispersion state of the filler was found to be highly dependent on the VA content. VA₁₂BS₅₀ showed agglomerated domains, VA₄₀BS₅₀ showed relatively better dispersion and VA₂₅BS₅₀ exhibited uniformly dispersed BS in the matrix.

The phase imaging of composites was further carried out to analyze dispersion and interfacial characteristics. Agglomerated domains of BS were observed in VA₁₂BS₅₀ and in VA₄₀BS₅₀; whereas, VA₂₅BS₅₀ showed uniform dispersion (Fig. 3.9a). The topographical profile was also found to support SEM observations (Fig. 3.9b). Average surface roughness was 66.08 nm, 22.34 nm and 93.38 nm in VA₁₂BS₅₀, VA₂₅BS₅₀, and VA₄₀BS₅₀ respectively. Skewness of the composites was 0.8641, -0.05 and 0.05651 and kurtosis was 3.03, 3.04 and 4.1 in VA₁₂BS₅₀, VA₂₅BS₅₀ and VA₄₀BS₅₀ respectively (Fig. 3.9c). These results confirm the surface was more uniform (flat) in VA₂₅BS₅₀ than that in either VA₁₂BS₅₀ or VA₄₀BS₅₀.

X-ray diffractograms of pristine EVA and BS are shown in Figure 3.10(a). VA₁₂ and VA₂₅ showed two major crystalline peaks at 21° and 23°, which were attributed to characteristic [110] and [200] crystal planes of polyethylene domain [89]. No crystallographic peak was observed in VA₄₀ and there was no significant difference in the percentage crystallinity of VA₁₂ and VA₂₅. Inset of figure 3.10(a) represents, X-ray diffraction pattern of BS. Several sharp peaks were observed, reflecting the highly crystalline nature of BS. All diffraction peaks in the XRD pattern matched well with the orthorhombic BS crystal

phase (JCPDS no. 24-1035). In the case of composites (Fig. 3.10b), all features of the pristine BS were retained and there was no shift or broadening of BS peak, suggesting the crystalline structure of BS remained intact during melt compounding [89-90].

3.3.7. Radiopacity of EVA/BS composites

All EVA/BS composites (25-75% BaSO₄ loading) were completely thermoplastic and melt processable. To evaluate the composition, thickness and VA content dependence of the radiopacity of EVA/ BaSO₄ composites, sheets (0.7 mm) of different EVA/ BaSO₄ composites were stacked to give different thickness (up to 2.8 mm) and were arranged on a radiochromic film: columns represent the thickness in decreasing order and the rows represent different compositions (Fig. 3.11a). A diagnostic X-ray machine was used to monitor the radiopaque behavior of the composites and aluminum sheets of thickness 0.5 and 1 mm were used for the comparison. The addition of BaSO₄ and the stack thickness had a significant impact on the radiopacity (Fig. 3.11a). It increased with an increase in thickness as well as with an increase in the filler loading. At even 50 % loading, the composite of 0.7 mm thick composite showed more radiopacity than a 0.5 mm aluminum sheet; at the higher filler loading, the difference in the radiopacity with aluminum sheets was profoundly increased. To quantify the radiopacity, a gray scale was used after subtracting the background; it may be noted that higher value of gray scale reflects higher radiopacity [91]. As evident from the figure, aluminum sheets have considerably lower value as 50% filled composites (Fig. 3.11b). These results are of high practical relevance,

considering the fact that compared to aluminum film, EVA/ BaSO₄ films are highly flexible, stretchable and can be easily transformed to any shape [92]. The mechanical and rheological characteristics, as discussed in the subsequent sections, established VA content dependent complex melt viscosity, mechanical hysteresis and stretchability of EVA/ BaSO₄ composites. Gray value is expected to be the highest for composite with the highest filler content and show a thickness dependent variation. Interestingly, however, at 75% BaSO₄ loading, the thickness variation was not obvious because the stack of two sheets attained maximum radiopacity, and a further increase in the thickness was of no consequence (Figure 3.11a). Nevertheless, at 50 wt% loading, composites showed systematic thickness dependence, and at all thicknesses, VA₂₅BS₅₀ showed highest radiopacity (Figure 3.11b). For a thickness of 0.7 mm, the gray values were 58, 71 and 60 for VA₁₂BS₅₀, VA₂₅BS₅₀ and VA₄₀BS₅₀ respectively. To understand the atomic composition dependence of radiopacity, the mass energy absorption coefficient (μ_{en}/ρ) of both the phases in the composite i.e. BS and EVA were calculated [93]. (μ_{en}/ρ) decreases with increase in radiation energy (Figure 3.11c). Inset of figure 3.4c shows (μ_{en}/ρ) for BaSO₄; unlike EVA, BaSO₄ exhibited photo-electric peaks in the energy range 1 to 100 keV. There was, however, no significant difference in mass attenuation coefficient of x-rays between VA₁₂, VA₂₅, and VA₄₀ in the energy range of diagnostic X-rays (40 keV-140 keV). Therefore, at a fixed BaSO₄ loading (50%), the 22% higher radiopacity of VA₂₅BS₅₀ than that of VA₁₂BS₅₀ could be due to the variation in the morphology and the polymer-filler interactions. It was evident from SEM

micrographs that VA₂₅BS₅₀ had the most homogeneous filler dispersion and distribution among all VA contents. Even more important than this gain in the radiopacity is the improvement in the mechanical and melt Rheology that can be obtained by varying the VA content, allowing development of highly flexible, melt processable and lightweight radiopaque formulations, which can be used in various forms. In the following sections, physico-mechanical properties, aggregation – disaggregation dynamics of BS in the composites and its interaction with VA₁₂, VA₂₅, and VA₄₀, are discussed in detail. These are critical for establishing morphology-property correlations.

3.3.8. Physico-mechanical properties and mechanical hysteresis of EVA/BaSO₄ composites

Higher BaSO₄ loading can often compromise mechanical attributes; conversely, high radiopacity demands the high loading of BaSO₄ in the composites. Stress-strain profiles of the different composites with different VA content and at fixed 50 wt% BaSO₄ loading is presented in Figure 3.12a. It can be seen that by just varying the VA segment ratio, mechanical properties can be tailored and in VA₄₀, even after 75% BaSO₄ loading, good mechanical integrity is maintained, as exemplified from high elongation at break (Figure. 3.12b). Stress-strain loops shown in Figure 3.12c represent the effect of BaSO₄ (50 wt%) addition on the mechanical hysteresis of the composites during five cyclic deformations; with an increase in the number of cycles, the hysteresis loops become smaller. VA₄₀BS₅₀ exhibited the least hysteresis. It may be noted that the cyclic deformation induced break down and the re-aggregation of BaSO₄ are the prime factors contributing to the observed high hysteresis [94]. It was found that

residual stress decreased with increase in VA content (first stress-strain cycle, residual stress: VA₁₂BS₅₀: 4.5 MPa, VA₂₅BS₅₀:1.9 MPa, VA₄₀BS₅₀: 0.23 MPa). To get a quantitative estimate of hysteresis, the work done (ΔW^c) during first, fifth cyclic deformations were evaluated and the hysteresis characteristic of composites was assessed from the recovery parameter (R) defined as [95]

$$R = \frac{\Delta W^{c5}}{\Delta W^{c1}} \quad (3.15)$$

Where ΔW^{c5} is the work done in the fifth cycle and ΔW^{c1} is the work done in the first cycle. Recovery parameter was calculated to be 0.51 for VA₁₂BS₅₀, 0.52 for VA₂₅BS₅₀ and 0.45 for VA₄₀BS₅₀. It increased within the filler loading, owing to the high density of BS; its correlation with BS structural breakdown are discussed later [96]. Elongation at the break increased with increasing the VA content. For 75% loading, VA₁₂ had the elongation at break of 12% whereas VA₄₀ had the elongation at the break >1000% (Figure 3.13b). The elastic modulus was highest for VA₁₂ and increased further with BaSO₄ loading. Most importantly by increasing the BaSO₄ content from 50% to 75% there was 7.5% increase in the modulus for VA₁₂; whereas, for VA₄₀ the increase in the modulus was 93.1% (Fig. 3.13c). This suggests changes in the filler loading capacity of the matrix with the change in the VA content. The shore A hardness increased with an increase in the filler content and decreased with an increase in VA content (figure 3.13d). As observed in the case of elastic modulus, the increase in the hardness was highest for VA₄₀ when filler content increased from 50% to 75%.

3.3.9. Effect of VA content and of BS loading on dynamic Rheology

Rheology of molten polymer composites provides critical information about the polymer-filler and filler-filler interactions within the matrix, which in turn determine mechanical, physical and combinatorial attributes such as radiopacity and flexibility of the composites. For all pristine copolymers and their composites, the complex viscosity showed frequency dependence, this varied with changes in VA content or in BS loading (Fig. 3.14a). Almost over the entire frequency range (0.1-100 rad/s), VA₄₀BS₅₀ showed lower complex viscosity than VA₂₅BS₅₀ and VA₁₂BS₅₀. The relative increase in complex viscosity of the composites with respect to that of pristine polymers was the least for VA₂₅BS₅₀ (inset figure 3.14a). At 100 rad/s, 50 wt% composites of VA₁₂BS₅₀ had 4.2 fold increase, VA₄₀BS₅₀ had 3.7 fold increase and VA₂₅BS₅₀ had 3.2 fold increase over their respective pristine polymers, while at 1rad/s, VA₁₂BS₅₀ and VA₄₀BS₅₀ had almost 5.3 fold increase and VA₂₅BS₅₀ had only ~ 4.3 fold increase. This peculiar behavior of VA₂₅BS₅₀ composite was also manifested in radiopacity, structural breakdown and morphology of the composites. Possible factors contributing to such a behavior include (i) changes in the polymer-filler interactions due to the variation in polar/non-polar segments in the copolymer with increase in VA content (ii) changes in the disordered/lamellae domains as copolymer architect changes with changes in VA content and (iii) overall changes in segmental motions in VA and ethylene domains due to entanglement effects [97].

Variation of storage modulus and loss modulus with angular frequency is presented in figure 3.14. VA₄₀ pristine sample exhibited a liquid-like behavior, showing G'' values higher than G' over the most of the frequency range; however, after 50 wt% loading, a crossover was observed around 125 rad/s. In the case of VA₁₂ and VA₂₅, even for pristine systems, a crossover was noted. In VA₂₅, the crossover was at 19 rad/s and for filled VA₂₅ the crossover was at 4.5 rad/s. VA₁₂ crossover was at 7.25 rad/s and for filled it was just at 1.2 rad/s (Figure 3.15). This finding again confirms the critical role of disordered phase (entangled) and ordered phase (lamellae) ratio in the EVA copolymer melts, which varies with VA content. These results also demonstrate the complex interactions and between VA domains in the copolymers and BaSO₄ suggesting segmental dynamics was more restricted in VA₁₂ and VA₂₅. In the terminal frequency region, the frequency dependence for G' was $\omega^{0.49-0.98}$ and in the higher frequency range, it was $\omega^{0.38-0.71}(r^2 \sim 1)$. For linear homopolymers, generally liquid-like behavior ($G' \propto \omega^2$) is reported and G'' is expected to be lower than G' in the terminal frequency region [98]. In the terminal region, a plateau was observed only in VA₁₂BS₅₀, which can be attributed to geometrical synergism between ordered PE domains and BS micro-particles which impede liquid-like flow i.e. increase in the melt viscosity [99]. It may be noted that with the increase in VA content, the complex viscosity of the melt decreased and the melt flow index (MFI) increased substantially. VA₁₂, VA₂₅, and VA₄₀ had MFI of 8g/10 min, 19g/10 min and 57g/10 min respectively at 190 °C. VA₂₅ did not display emergence of solid-like behavior as observed in VA₁₂, though it showed

enhanced moduli matching that of VA₁₂ at high frequency. For the unfilled systems, the frequency dependence was higher than it was for the filled system.

With the addition of BaSO₄, all composites showed an increase in the storage modulus (Table 3.3); the unfilled system did not show any rubber-like behavior and the solid-like plateau or zero shear viscosity was not observed in any of the systems (Figure 3.16). However, with the addition of BS, a reduction in frequency dependence in the low-frequency region was observed which may be attributed to the reduction in relaxation behavior of polymer chains (Figure 3.15). Interestingly, though, complete frequency independence was not observed for any of the composites. The storage modulus increased both with the addition of filler and with the VA fraction. The highest modulus was for VA₁₂ and the lowest was for VA₄₀ over the entire frequency range. However, for the same percentage of BS loading, the difference in storage and loss modulus was more pronounced in the lower frequency region. The difference was particularly notable in the case of VA₂₅ and VA₁₂, for which G' and G'' values overlapped till 10 rad/s and then diverged significantly. This difference at low frequency points out the significance of physical interactions between BS particles and the copolymer segments, mainly the ethylene domains. It is understood that higher the BS content, the higher will be the restriction to the molecular motions in the polymer chain. At 1 rad/s, the reinforcement for VA₄₀, VA₂₅ and VA₁₂ composites was observed to be 860%, 512%, and 418% respectively, further confirming criticality of VA content to the melt Rheology. The dispersion and the location of filler in the matrix are important to explain the effect of BS

loading on the storage modulus. Cole-Cole plot showed a marked departure from semicircular behavior, reflecting that molten system do not follow a Maxwellian behavior (Figure 3.16c). Notably, VA₂₅BS₅₀ showed the highest amplitude in the Cole-Cole diagram, which might be interpreted as the constrained molecular mobility of polymer chains [100-101]. This seems to contradict the relative change observed in the complex viscosity (Figure 3.16a); however, when one looks at the Cole-Cole diagram of the unfilled copolymers, it is clear that VA₂₅ had the highest amplitude. Thus, the relative change in VA₂₅ on the composite formation was not substantial, interestingly, though; the behavior of VA₁₂ and VA₄₀ was markedly changed in filled and unfilled state. Such an inference was also supported by the DMTA, time temperature superimposition and apparent activation energy of molecular motion discussed later. Essentially, these results indicate that a change in VA domain in the copolymer (EVA) itself has a marked effect on constraining molecular motion. They further suggest that the VA and BaSO₄ are non-interacting (chemically) systems, and the Rheology and other properties mainly rely on the mechanical (physical) interactions governed by the morphology and the interface. A detailed investigation on the filler-filler aggregation dynamics and filler structural breakdown was therefore conducted.

3.3.10. Filler-filler contact break, polymer-filler interface breakdown in EVA/BaSO₄ composite

To further understand the interaction between the polymer (EVA) and the filler (BS), the Payne effect [102] i.e. the dependence of storage modulus on

strain amplitude was investigated under shear strain (molten state) and under tensile strain (solid state). It can be seen in figure 3.17(a) that all systems exhibit Payne behavior, albeit VA content has marked influence on it. The VA₁₂BS₅₀ system showed structural breakdown at much lower strain than observed for VA₂₅BS₅₀ and VA₄₀BS₅₀. This significant increase in strain for structural breakdown with VA content, suggests better filler-polymer interactions in VA₂₅BS₅₀ and VA₄₀BS₅₀ composites; it may be noted that normalized magnitude of the Payne effect (ΔG_n) is strongly correlated with the polymer-surface interaction and can be measured using the following relation

$$\Delta G_n = \frac{G'_\infty - G'_0}{G'_0} \quad (3.16)$$

Where G'_0 shear storage modulus at low is strain; G'_∞ is the shear storage modulus at the very high strain. These values correspond to the minimum (plateau) and the maximum strain (plateau) values respectively during amplitude sweep experiments. The magnitude of Payne effect was found to be 22.1, 17.1 and 15.2 for VA₁₂BS₅₀, VA₂₅BS₅₀ and VA₄₀BS₅₀. The power law was followed in the structural breakdown region by all composites and $G(\gamma) \sim \gamma^{-1.05}$ for VA₁₂BS₅₀, $G(\gamma) \sim \gamma^{-0.98}$ for VA₂₅BS₅₀ and $G(\gamma) \sim \gamma^{-0.89}$ for VA₄₀BS₅₀ was deduced. These results clearly indicate that increase in VA content improves structural breakdown characteristics. This observation of a reduction in the structural breakdown with an increase in VA content was also corroborated with the significantly higher elongation at break and morphology described earlier. To further understand filler-filler contact breakage and polymer-filler interface

breakdown [103-104]; the amplitude sweep data was fitted to phenomenological quantitative Kraus model which rely on agglomeration and de-agglomeration of filler networks under strain.

$$G'(\gamma) = G'_\infty + \frac{G'_0 - G'_\infty}{1 + \left(\frac{\gamma}{\gamma_c}\right)^{2m}} \quad (3.17)$$

$G'(\gamma)$ is the shear storage modulus at shear strain γ ; G'_0 and G'_∞ are as described above, γ_c is the critical strain at which $G'(\gamma)$ decreases to a value half of $G'_0 - G'_\infty$. Magnitude of structural breakdown is often gauged in terms of $G'_0 - G'_\infty$ or ΔG_n . Such a loss in shear modulus is attributed to the presence of excess force between filler particles or between polymer and filler as the contacts are broken [105]. Where m is related to the fractal dimension and depends on the geometric quality of filler network, but is independent of specific polymer type and filler. As the filler network grows to smaller and smaller unit with growing strain, at the low strain, the elastic contribution of filler network is dominant whereas at higher strain, hydrodynamic and polymer-filler interactions dominate. The fitting parameter of the Kraus model to the experimental data is presented in Table 3.4. The experimental data for all three VA content fitted well with the Kraus model (in all cases: $r^2 > 0.99$). This implies dominance of filler-filler disaggregation over polymer-filler interaction in contributing to the structural breakdown. The value of m, which is expected to be close to 0.5 and suggestive of strain sensitivity of matrix, reflects that BS aggregation and disaggregation dynamics in VA₁₂ is significantly different from that in VA₂₅ and in VA₄₀. The critical frequency which is a suggestive polymer-filler interaction and overall

dispersion of the filler in the matrix was considerably lower in VA₁₂. This indicates that overall filler-disaggregation and aggregation dynamics in VA₁₂ matrix is considerably different than that in VA₂₅/VA₄₀. A possible factor might be variation in the polar content with the increase in VA fraction. Such a change is expected to affect polymer-filler interaction and segmental dynamics. It may, however, be noted that this analysis was done in the molten state, which does not account for crystalline domains, which are major determinants of the properties of polymer composites.

To understand the structural breakdown in the solid state, the strain dependence of elastic storage modulus (E') was also monitored. It can be seen from figure 3.17b that the highest structural breakdown was observed in VA₁₂ composites. Kraus model was applied to dynamic mechanical data, replacing shear storage modulus (G') with elastic modulus (E') and angular shear strain with uni-axial tensile strain in the equation (iii). The fitting was excellent in all the cases and it was found that critical strain was lowest for VA₁₂ and was significantly higher for VA₂₅ and VA₄₀ (Table 3.3). The critical strain was about 4 times higher in VA₂₅BS₅₀ than it was in VA₄₀BS₅₀. As reflected from the XRD results discussed later, VA₁₂ and VA₂₅ both have much higher crystalline content than VA₄₀. The lower structural breakdown in case of VA₂₅BS₅₀ is, therefore, suggestive of better dispersion and interfacial interaction [105]. These results establish that even in the solid state the filler disaggregation dynamics, filler dispersion and polymer-filler interaction greatly changed with a variation in the VA content.

3.3.11. Visco-elastic master curve and fractional free volume of composite melts in EVA/ BaSO4 composites

Time-temperature superimposition (TTS) master curves of VA₁₂, VA₂₅ and VA₄₀ and their composites were generated by monitoring shear Rheology as a function of angular frequency at different temperatures (Figure 3.18(a,b)). The reference temperature was 140°C. Both G' and G'' increases with frequency for all the composites. The Williams–Landel–Ferry (WLF) model was used to analyze the time (t) - temperature (T) behavior of composites [99,106]. It can be described as

$$\log a_T = \frac{-C_1(T-T_0)}{C_2+(T-T_0)} \quad (3.18)$$

Where, a_T is horizontal shift factor, C_1 and C_2 are constants, T_0 is reference temperature. Dependence of a_T and its fitting to WLF model is shown in Figure-3.19 a. WLF model fitted well with VA₁₂BS₅₀ and VA₂₅BS₅₀; however, it could not describe the t-T behavior of VA₄₀BS₆₀ composite. The value of C_1 and C_2 are tabulated in Table 3.5 for VA₁₂ and VA₂₅ composites.

C_1 and C_2 are related to fractional free volume (f_0) and its coefficient of thermal expansion (α_f) by following relations

$$C_1 = \frac{B}{2.303 f_0} \quad (3.19)$$

$$C_2 = \frac{f_0}{\alpha_f} \quad (3.20)$$

Where B is a constant. f_0 was found to be 49.5 and 30.4, and α_f was 0.05 and 0.04 in VA₁₂BS₅₀ and VA₂₅BS₅₀ composites respectively. The fractional free volume represents the ratio of free volume to the total volume of melt [107] and a considerably lower fractional free volume of VA₂₅BS₅₀ than that of VA₁₂BS₅₀

suggests strong polymer-filler interaction or better dispersion of BaSO₄ in VA₂₅BS₅₀, corroborating well with the structural breakdown results discussed in the previous section. As WLF fails to represent VA₄₀BS₅₀ composites, apparent activation energy (E_a) of molecular motion was estimated by Arrhenius equation for all pristine polymers and their composites

$$E_a = R \frac{d \ln a_T}{d(1/T)} \quad (3.21)$$

The Arrhenius equation fitted well with all the composites and pristine polymers (Fig. 3.19 b). The activation energy was found to be 45.3 kJ/mol, 62.4 kJ/mol and 63.5 kJ/mol for VA₁₂, VA₂₅ and VA₄₀ respectively. It is clear that activation energy for molecular motion is much higher in VA₂₅ and VA₄₀ than that in VA₁₂. Such a difference in E_a reflects a critical effect of polar interaction originating from VA domains. On addition of BaSO₄, the apparent activation energy of compounds was 68.0 kJ/mol, 63.7 kJ/mol and 88.3 kJ/mol for VA₁₂BS, VA₂₅BS and VA₄₀BS respectively. These results reflect the contribution of BaSO₄ agglomerates in hindering the molecular motion. With respect to unfilled systems, in VA₁₂BS₅₀ and VA₄₀BS₅₀ a substantial increase in the E_a was observed, whereas, in VA₂₅BS₅₀ there was a small change. Therefore, if the increase in apparent activation energy is considered, it can be concluded that the molecular motion is considerably restricted in all composites after BS loading, except for VA₂₅. This result corroborates the complex viscosity results presented earlier. It may be noted that that even at a fixed loading of BaSO₄, a significant variation in the fracture and topographic morphology of the composites was found with variation in VA content and BaSO₄ agglomeration was more

prominent in VA₁₂ and VA₄₀ than in VA₂₅, as exemplified from the results of phase imaging, morphology and roughness analyses. It is also worthy to note that the Kraus model was fitted well with all composites, reflecting critical role of filler aggregation and disaggregation dynamics over this polymer-filler interfacial characteristics. These results suggest that contribution of filler networks in either VA₁₂ or in VA₄₀ provide more steric hindrances to the system than that was in VA₂₅. Density (ρ_c) of the composites is also expected to provide an idea about free volume, voids, and interfacial compatibility. ρ_c of the composites was calculated experimentally and was compared with the values calculated theoretically using following relations describing the rule of mixture (upper bound) and the inverse rule of mixture (lower bound)

$$\rho_c = (1 - x) \cdot \rho_{EVA} + x \cdot \rho_{BS} \quad (3.22)$$

$$1/\rho_c = x/\rho_{BS} + (1 - x)/\rho_{EVA} \quad (3.23)$$

where x is the fraction of BS, and ρ_{BS} and ρ_{EVA} are the densities of BS and EVA respectively. All composites showed higher values than those predicted by the inverse rule of mixture (data not reported) and lower values than that predicted by the rule of mixture (Table-3.3). The difference between theoretical (rule of mixture) and experimental values ($\Delta\rho$), which reflects increased free volume in the matrix, was found to be highest in case of VA₁₂ (162 kg/m³), whereas in case of VA₂₅ and VA₄₀ the $\Delta\rho$ was just 127 kg/m³ and 124 kg/m³ respectively. This observation supports the results obtained on fractional free volume obtained in the molten condition. It can be reasonably concluded that VA₂₅BS₅₀ composites

offer lower structural breakdown, lower fractional free volume and lower deviation from the density predicted by additive rules.

3.3.12. Dynamic thermo-mechanical analysis of EVA/ BaSO₄ composites

The dynamic mechanical properties of the composites were found to be affected by the vinyl content as well as by the BaSO₄ loading; with an increase in the BS content, the storage modulus increased while the loss tangent decreased (Figure 3.20a). Furthermore, an increase in the VA fraction led to a significant decrease in the elastic modulus and increase in the loss factor. In the glassy region, the difference in the storage modulus between VA₁₂ and VA₂₅ was not significant; however, in the rubbery region at 30 °C, VA₄₀ and VA₂₅ had a storage modulus of 140 Pa and 70 Pa respectively. VA₄₀ showed the most significant effect of temperature on the elastic modulus, which decreased from ~1.7 kPa in the glassy region to just 8 Pa at 30°C. With the increase in filler content, from 50% to 75%, in the VA₁₂ composites, there was more than 100% increase in storage modulus at 30 °C; whereas for the VA₄₀, a similar increase in BaSO₄ loading resulted only in a marginal increase of 35% in the storage modulus. The difference in the storage shear modulus in the molten condition described in the previous section and the storage tensile modulus in solid condition is very critical; as the former considers only molten visco-elastic behavior where no accounting was made for crystallinity and macromolecular reorganization during beta transitions. Variation in the $\tan \delta$ with an increase in the temperature has been shown in the figure 3.20b. The glass transition was observed at – 21 °C and is suggestive of the amorphous domain of vinyl acetate

segments. It was interesting to note that even at higher loading, no major shift in the glass transition was observed; the little variations observed in storage modulus with BaSO₄ loading can be attributed to the chain pinning introduced by BaSO₄. It further suggests that the VA content related differences are mostly due to the morphology of the composites rather than due to chemical interactions between VA segments and BaSO₄ domains, as hypothesized in previous sections. This also explains the excellent fitting of the structural breakdown data to phenomenological quantitative Kraus model which mainly relies on filler-filler aggregation and disaggregation dynamics and not on polymer-filler interface dynamics. Based XRD, morphological, rheological data and other data reported in this manuscript, it can be concluded that even at the same percentage of BS loading, different morphological arrangements in EVA/ BaSO₄ composites are possible which can offer distinct radiopacity and mechanical behavior (Figure 3.21). These radiopaque composites are completely flexible, thermoplastic, non-biodegradable and offer tunable radiation attenuation behavior. The constituents in these radiopaque composites are already in biomedical applications and are expected to be biocompatible; however, dedicated *in-vitro*/ *in-vivo* studies might be needed for precisely ascertaining the cyto-compatibility profile of EVA/ BaSO₄ composites, as deemed appropriate for the targeted application/organ.

3.4. Summary

Irradiation by gamma can be effectively used to crosslink the composites containing large amounts of high Z fillers and such polymer composites have potential as flexible radiation shields for ²⁴¹Am γ radiation. The

specific gravity of the composites followed the rule of mixture closely up to 50 wt % loading; slight deviation at higher loading was assigned to agglomeration within the matrix Bi_2O_3 reinforces the PDMS matrix was well corroborated with the mechanical properties. EB decreased with radiation dose as well as with filler loading, while Young's modulus increased significantly and was found to deviate from the Nielsen's micromechanical model. Interestingly the deviation was positive, suggesting formation of Bi_2O_3 network within PDMS. Attenuation of gamma ^{241}Am at 70 wt% filler loading was observed to be 90%. Thermal stability of composites significantly improved with the addition of filler. The study establishes that radiation cross-linked matrices can be excellent choice for developing lead free flexible shielding. However further understanding of morphology-attenuation correlation and attenuation coefficients of PDMS/ Bi_2O_3 for gamma rays of different energies are needed to use such composites in advanced applications. It was also established that tailoring of vinyl content can ascertain high radiopacity even at higher loading of BaSO_4 . Such effects translated in better gray values than those obtained from the aluminum sheets of comparable thickness, while retaining markedly high elongation at break, low mechanical hysteresis and complete flexibility. EVA/ BaSO_4 composites displayed a complex interplay of the morphology, the crystallinity and the copolymer architecture. VA content of 25% displayed unique attribute in most of the rheological, mechanical and dynamic thermo mechanical properties. The power law was followed by all composites in the structural breakdown region and the filler-filler structural breakdowns was found to be a key factor in non-

linear strain behavior, which was dependent on VA content. Time-temperature super-imposition study also showed a difference in fractional free volume with a change in vinyl acetate content. These results are expected to be highly useful in designing radiopaque polymer composites for medical and other applications with predetermined physico-mechanical and radiation opacity behavior.

Table 3.1: Percentage deviation from Nielsen's model at different doses

Weight fraction (Bi₂O₃)	(%) Deviation (100kGy)	(%) Deviation (200 kGy)	(%) Deviation (400 kGy)
0.00	0.00	0.00	0.00
0.05	-12.60	-12.23	-12.29
0.10	-33.48	-2.88	0.87
0.30	-51.09	-22.55	-7.07
0.50	-53.30	-75.71	-44.98
0.70	-104.96	-89.22	-100.23

Table 3.2: Effect of Bi₂O₃ on thermal degradation of PDMS

Weight fraction (Bi₂O₃)	Onset temperature (°C) (step 1)	Temperature (°C) 10% weight loss	Onset temperature (°C) (step 2)
0.0	406.5	451.7	451.4
0.1	419.5	476.5	464.5
0.3	417.7	471.4	486.6
0.7	448.1	495.3	491.2

Table 3.3: Small amplitude oscillatory shear and dynamic thermo-mechanical properties of EVA copolymers and EVA/BS composites

Composition	*G' at 0.2 rad/s (Pa)	*G' at 1 rad/s (Pa)	#Glass transition (° C)	#Loss factor (tan δ)
VA ₁₂	2028	4313	-18.6	0.15
VA ₂₅	1170	3516	-24.5	0.25
VA ₄₀	165	455	-23.9	0.52
VA ₁₂ BS ₅₀	14468	24495	-21.6	0.14
VA ₂₅ BS ₅₀	4815	18029	-24.2	0.19
VA ₄₀ BS ₅₀	1246	3894	-24.0	0.53

* Data from small amplitude oscillatory shear experiments

Data from dynamic thermomechanical analysis

Table 3.4: Parameters of phenomenological quantitative Kraus model fitting to non- linear oscillatory melt shear rheology (angular shear strain) and to solid dynamic mechanical analysis (uniaxial tensile strain) data of EVA BS composites

	Composition	G'_0 (Pa)	γ_c	m	r^2
Oscillatory shear strain (Melt rheology)	VA ₁₂ BS ₅₀	42376.11	20.60±1.27	0.43	0.99
		±449.08		±0.02	
	VA ₂₅ BS ₅₀	18330.54	44.87±2.57	0.48	0.99
		±131.68		±0.02	
	VA ₄₀ BS ₅₀	7244.42	71.20±3.50	0.46	0.99
		±31.44		±0.01	
		E'_0 (MPa)	γ_c	m	r^2
Oscillatory tensile strain (DMTA)	VA ₁₂ BS ₅₀	319.02	3.80±0.10X 10 ⁻³	0.58	0.99
		±1.28		±0.02	
	VA ₂₅ BS ₅₀	104.72	16.80±4.00 X 10 ⁻³	0.44	0.99
		±0.45		±0.02	
	VA ₄₀ BS ₅₀	9.77	32.50 ±4.00 X 10 ⁻³	0.41	0.99
		±0.03		±0.02	

Table 3.5: WLF parameters, fractional free volume and experimental and theoretical densities of pristine EVA copolymers and EVA/BS composites

	C₁	C₂ (K)	f₀ (T ₀ =140 °C)	a_f (K ⁻¹)	ρ_{exp} (kg/m ³)	ρ_{theo} (kg/m ³)	\$Un fille d syst ems , the oret
VA ₁₂	9.4	234.5	21.6	0.09	933	--\$	
VA ₂₅	13.7	318.4	31.6	0.10	948	--\$	
VA ₄₀	12.2	238.0	28.0	0.12	960	--\$	
VA ₁₂ BS ₅₀	21.5	957.0	49.5	0.05	1530	1779	
VA ₂₅ BS ₅₀	13.2	629.0	30.4	0.05	1572	1800	
VA ₄₀ BS ₅₀	--#	--#	--#	--#	1580	1818	

ical values are same as experimental values.

WLF fitting of the data was poor and the coefficient were considered unreliable.

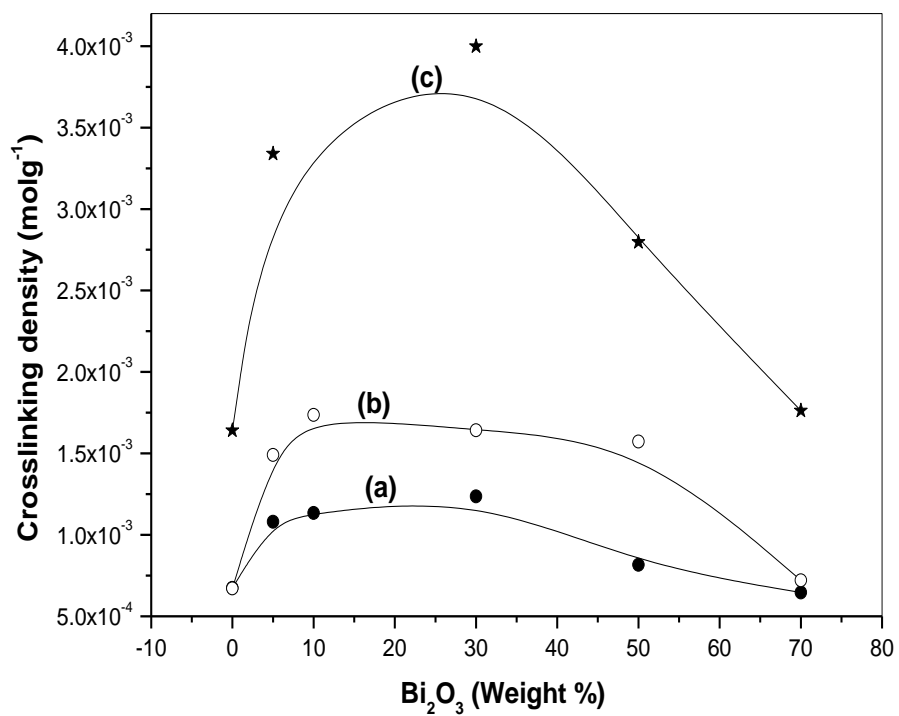


Figure 3.1: Variation in cross-linking density of composites with absorbed dose (a) 100kGy (b) 200kGy (c) 400 kGy

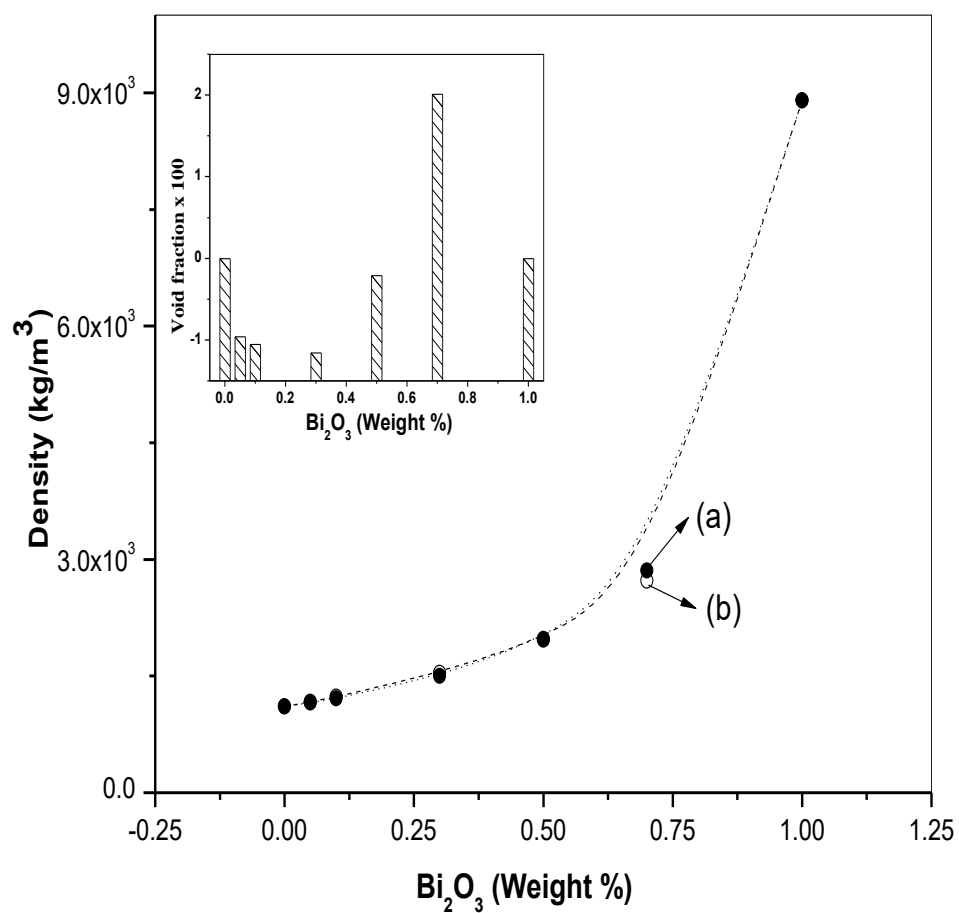


Figure 3.2: Variation in density of composites with absorbed dose.
(a)Experimental values (b) Theoretical values theoretical. Inset:
Percentage changes in density with the loading of Bi₂O₃ (Weight %)

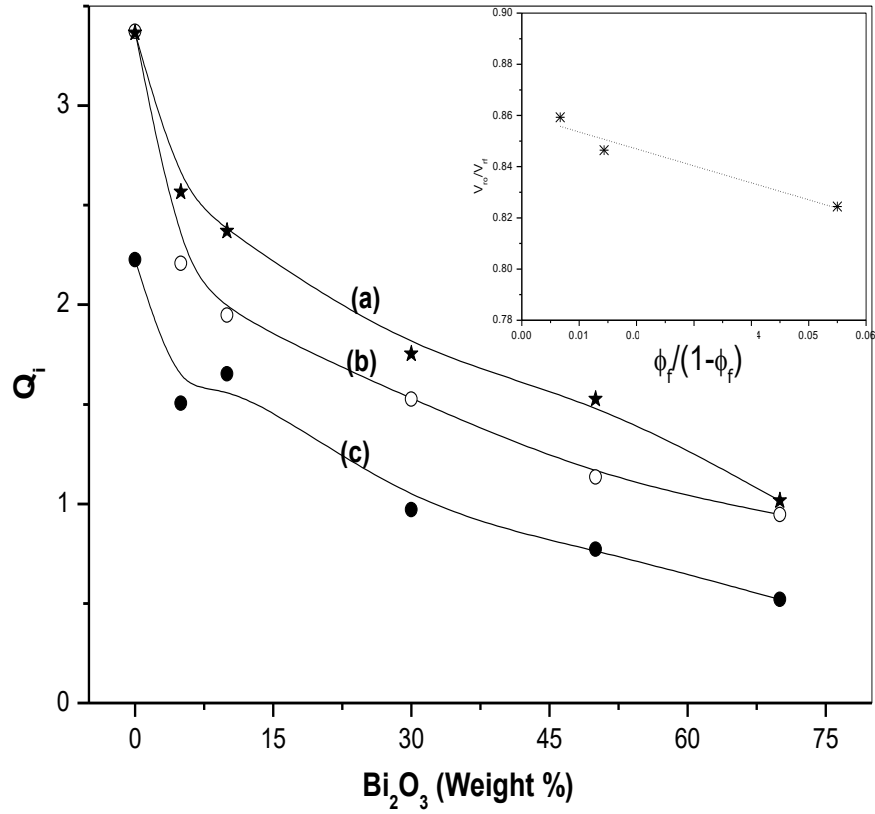


Figure 3.3: Variation of swelling ratio [$Q_i = (\text{Swelled weight}/\text{initial polymer weight})$] of composites with absorbed dose (a) 100 kGy (b) 200 kGy (c) 400 kGy Inset: Kraus plot for PDMS/ Bi_2O_3 composites

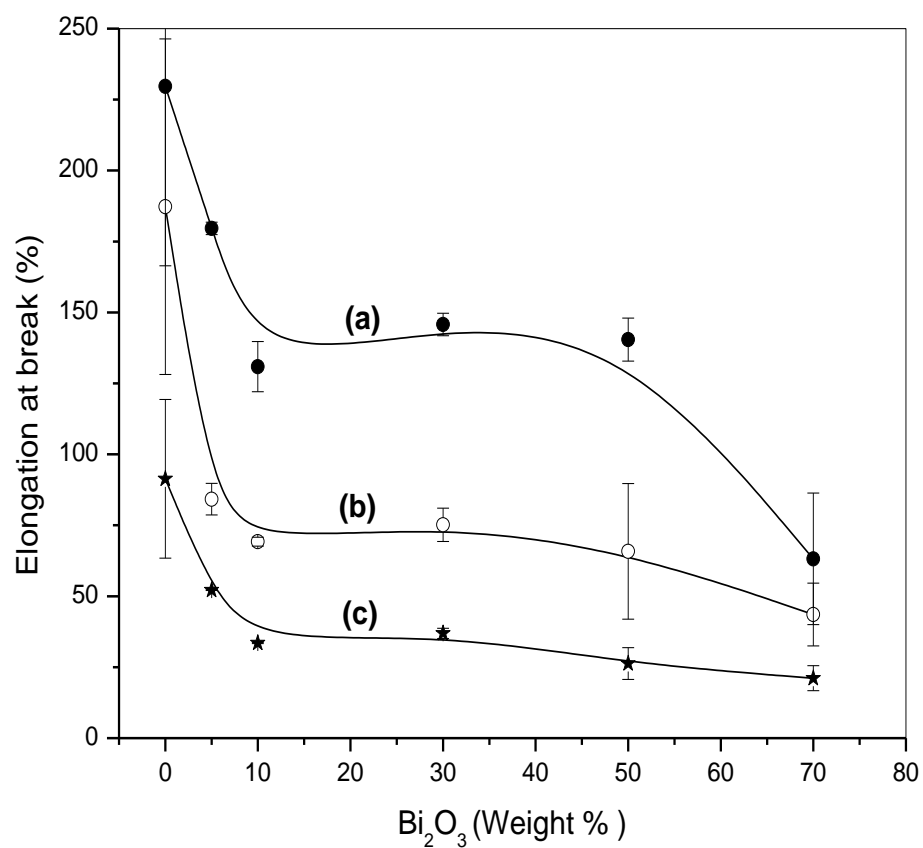


Figure 3.4; Variation in elongation at break of composites with absorbed dose (a) 100 kGy (b) 200 kGy (c) 400 kGy

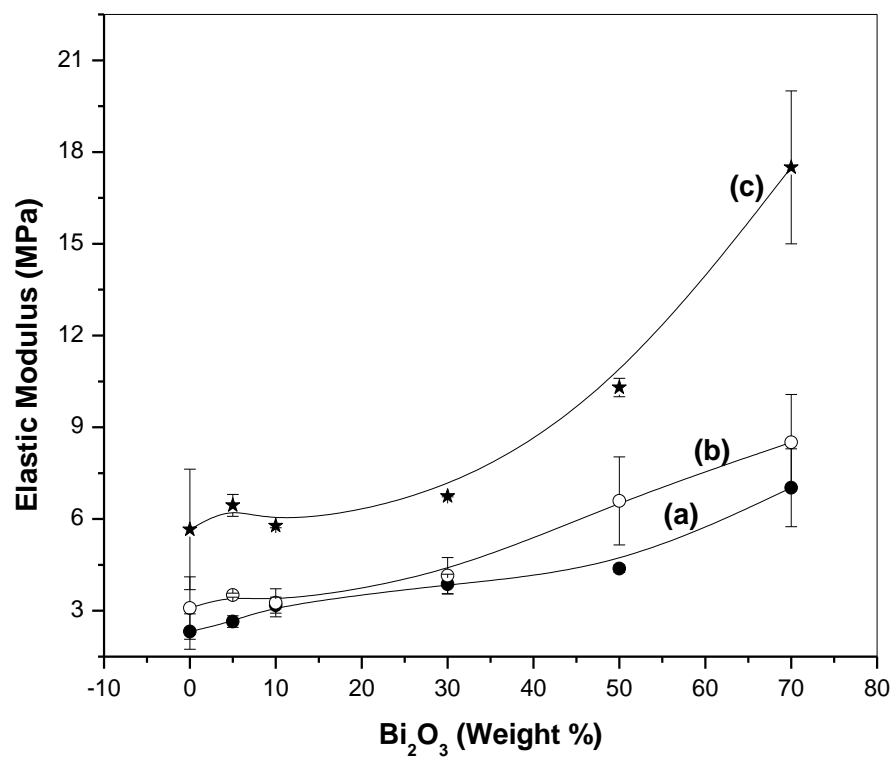


Figure 3.5: Variation in elastic modulus of composites with absorbed dose (a) 100 kGy (b) 200kGy (c) 400kGy

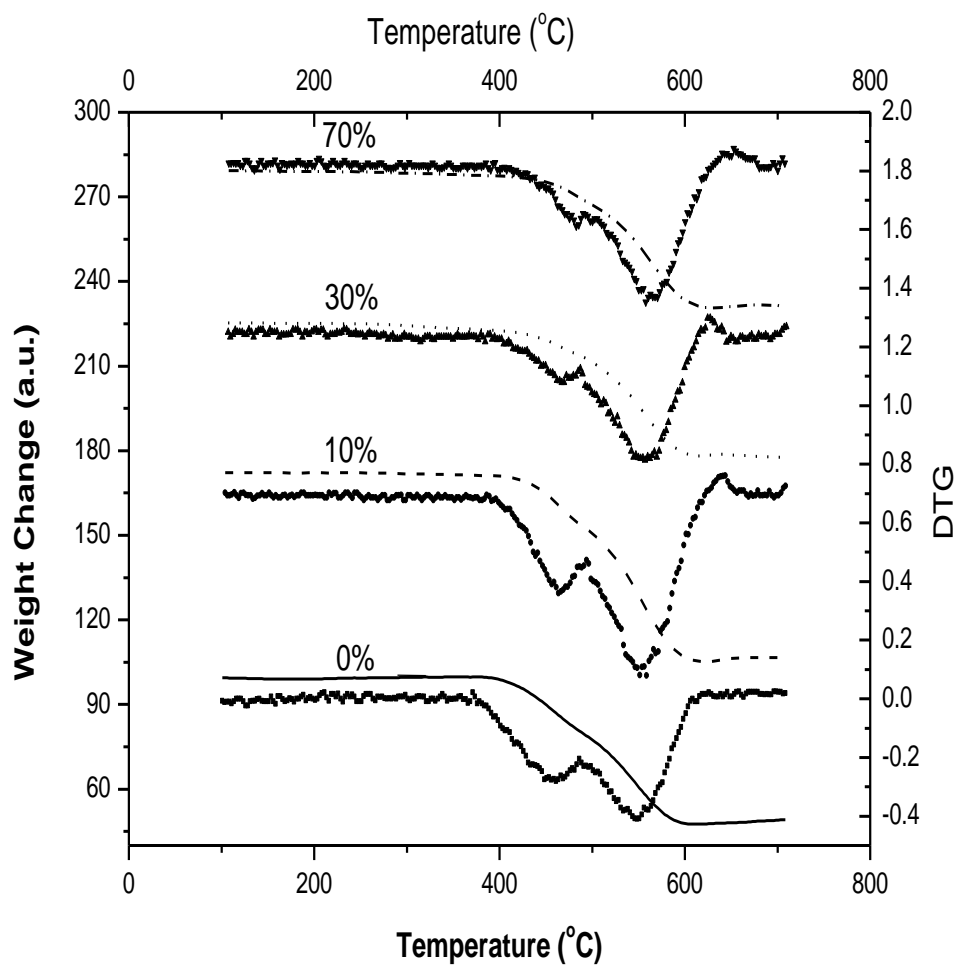


Figure 3.6: Thermo-gravimetric profiles of composites containing different percentages of Bi₂O₃ (profiles have been offset for better clarity)

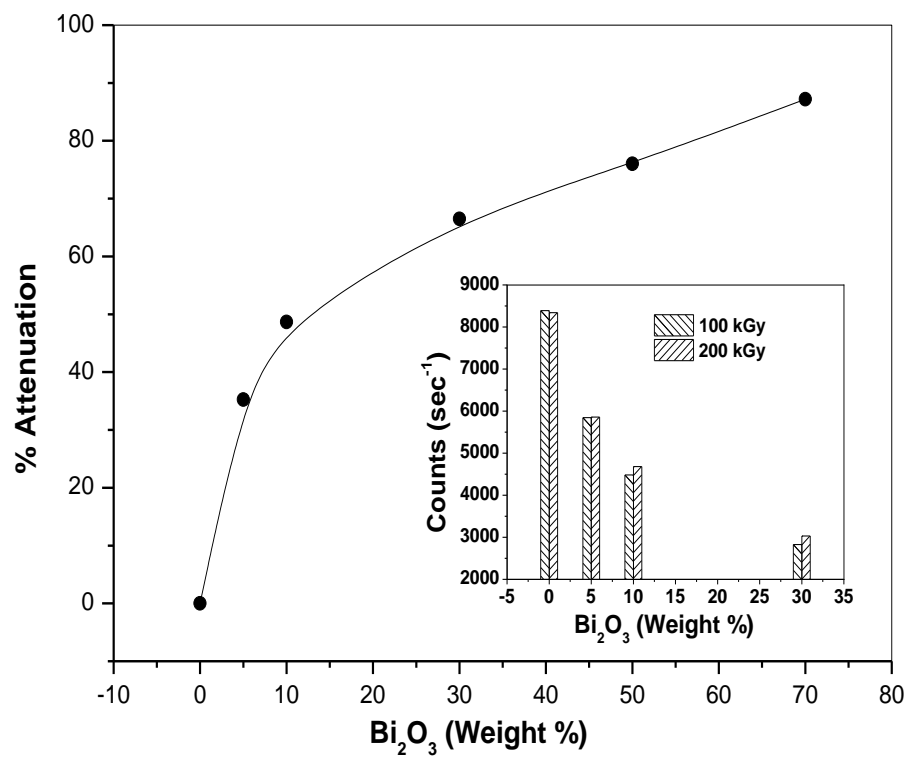


Figure 3.7: Variation in attenuation of different composites irradiated to different doses. Inset: Variation in counts with Bi_2O_3 (Weight %) at two different radiation doses.

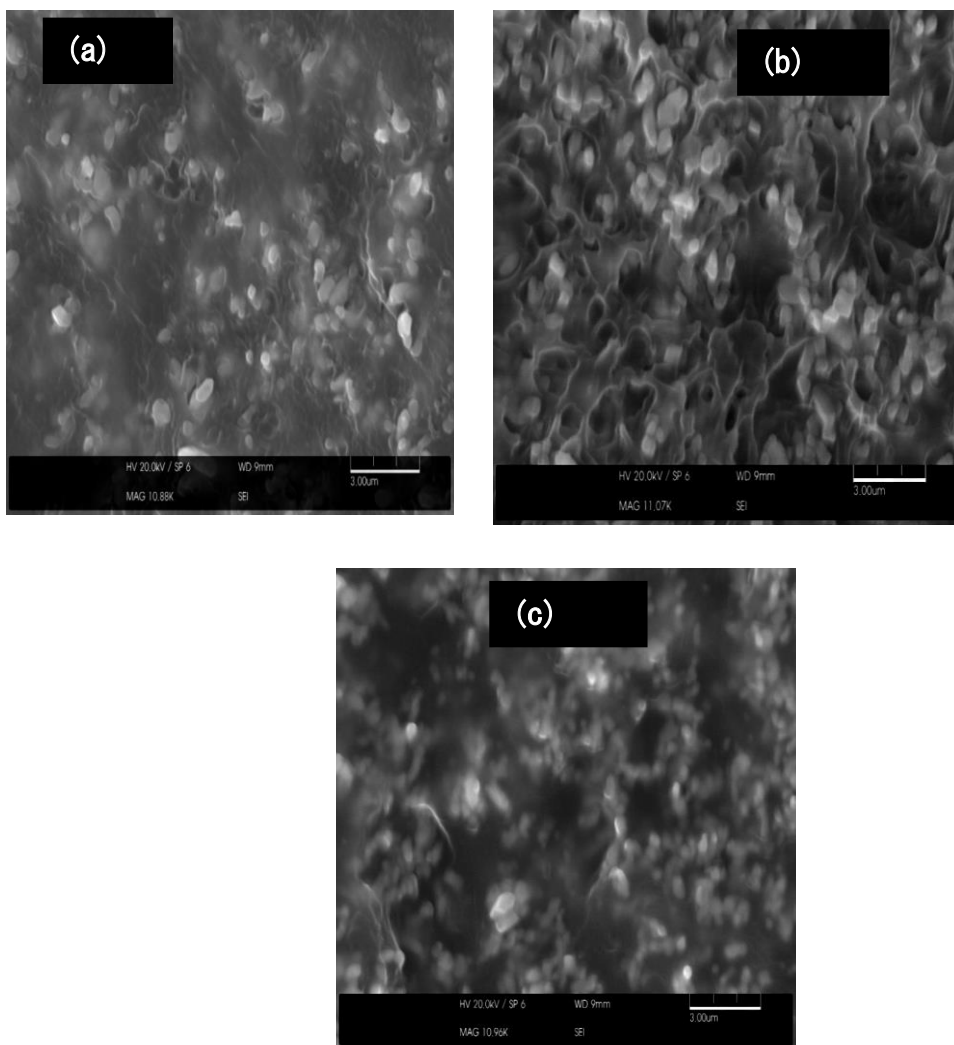
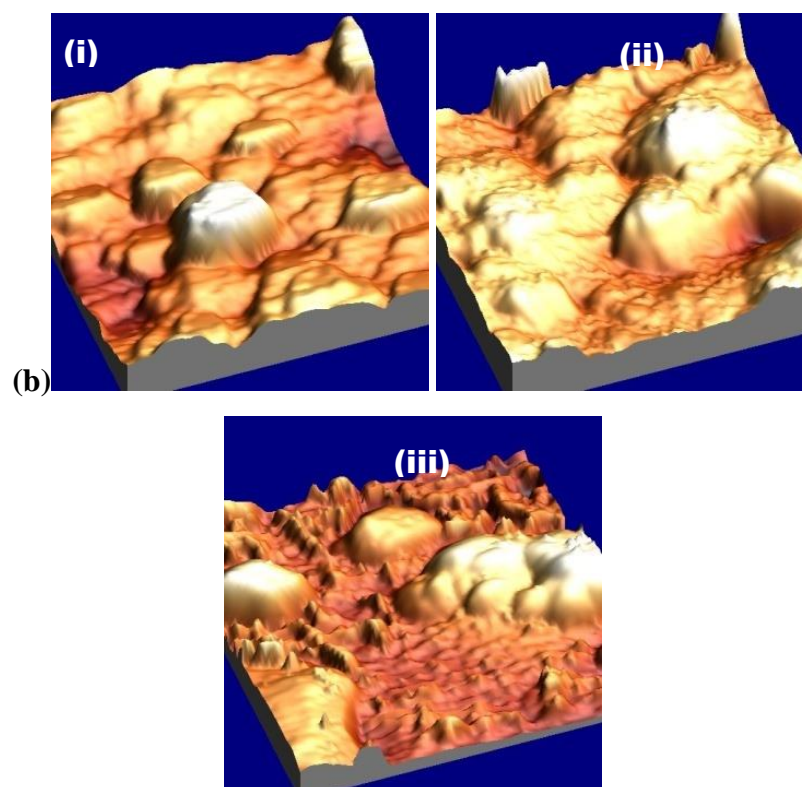
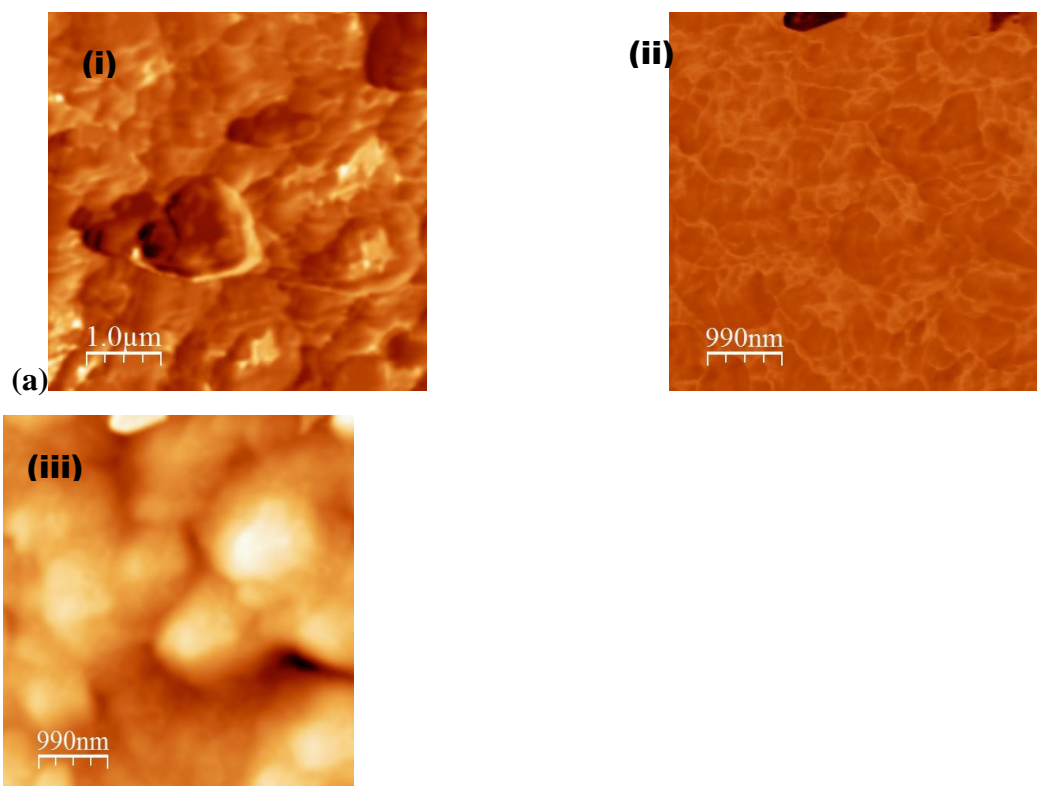


Figure 3.8: Scanning electron micrographs of cryogenic fracture surfaces of EVA/ BaSO₄ composites (a) VA₁₂BS₅₀ (b) VA₂₅BS₅₀ (c) VA₄₀BS₅₀.



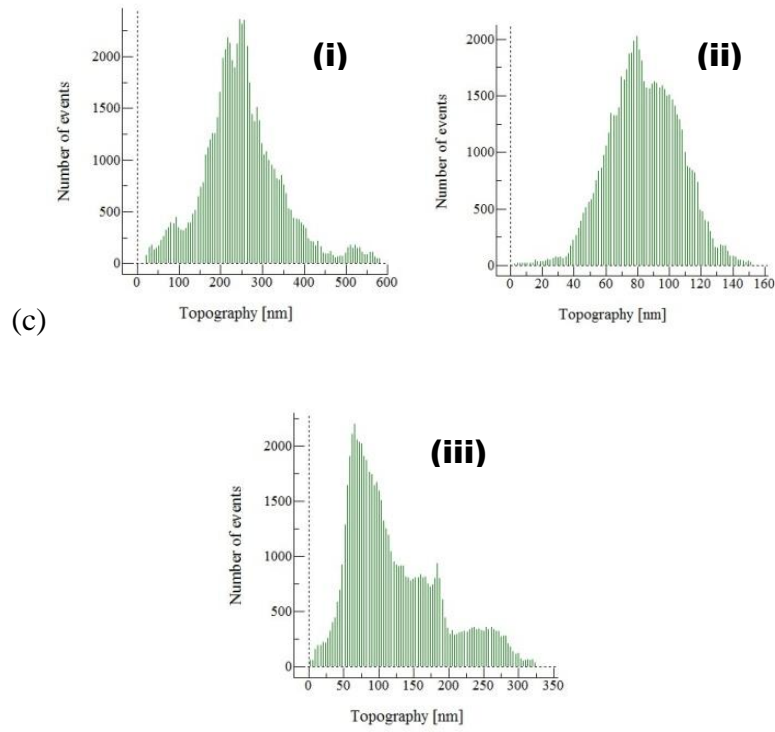


Figure 3.9: Atomic force microscopy of the composites (a) Phase image of (i) VA₁₂BS₅₀ (ii) VA₂₅BS₅₀ (iii) VA₄₀BS₅₀ (b) topographical images of (i) VA₁₂BS₅₀ (ii) VA₂₅BS₅₀ (iii) VA₄₀BS₅₀ (c) histograms of surface roughness (i) VA₁₂BS₅₀ (ii) VA₂₅BS₅₀ (iii) VA₄₀BS₅₀

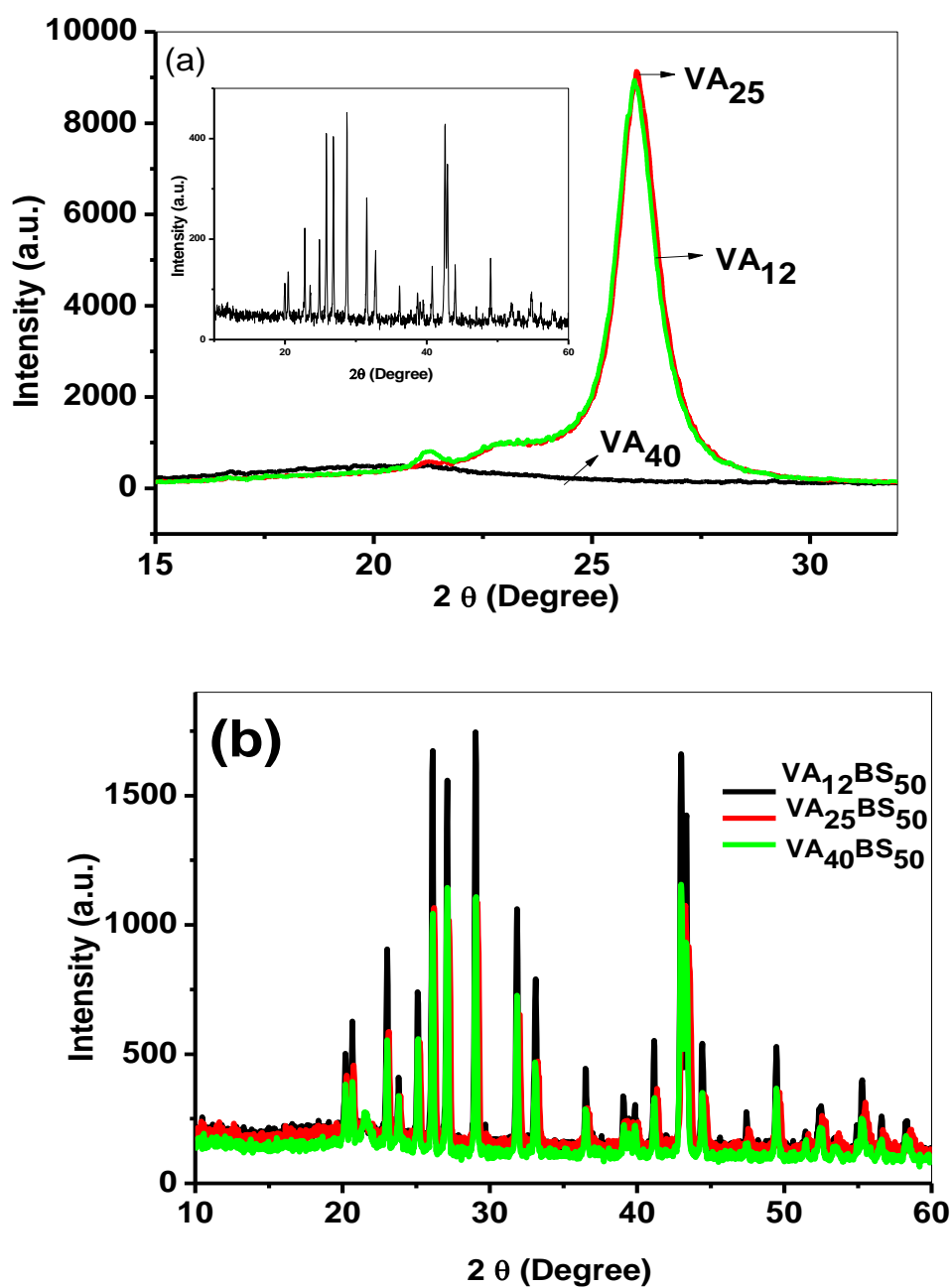


Figure 3.10: X-ray diffractograms of (a) EVA with different VA content 12 % (VA₁₂), 25% (VA₂₅) and 40% (VA₄₀) [Inset: X-ray diffractograms of BS] (b) VA₁₂BS₅₀, VA₂₅BS₅₀ and VA₄₀BS₅

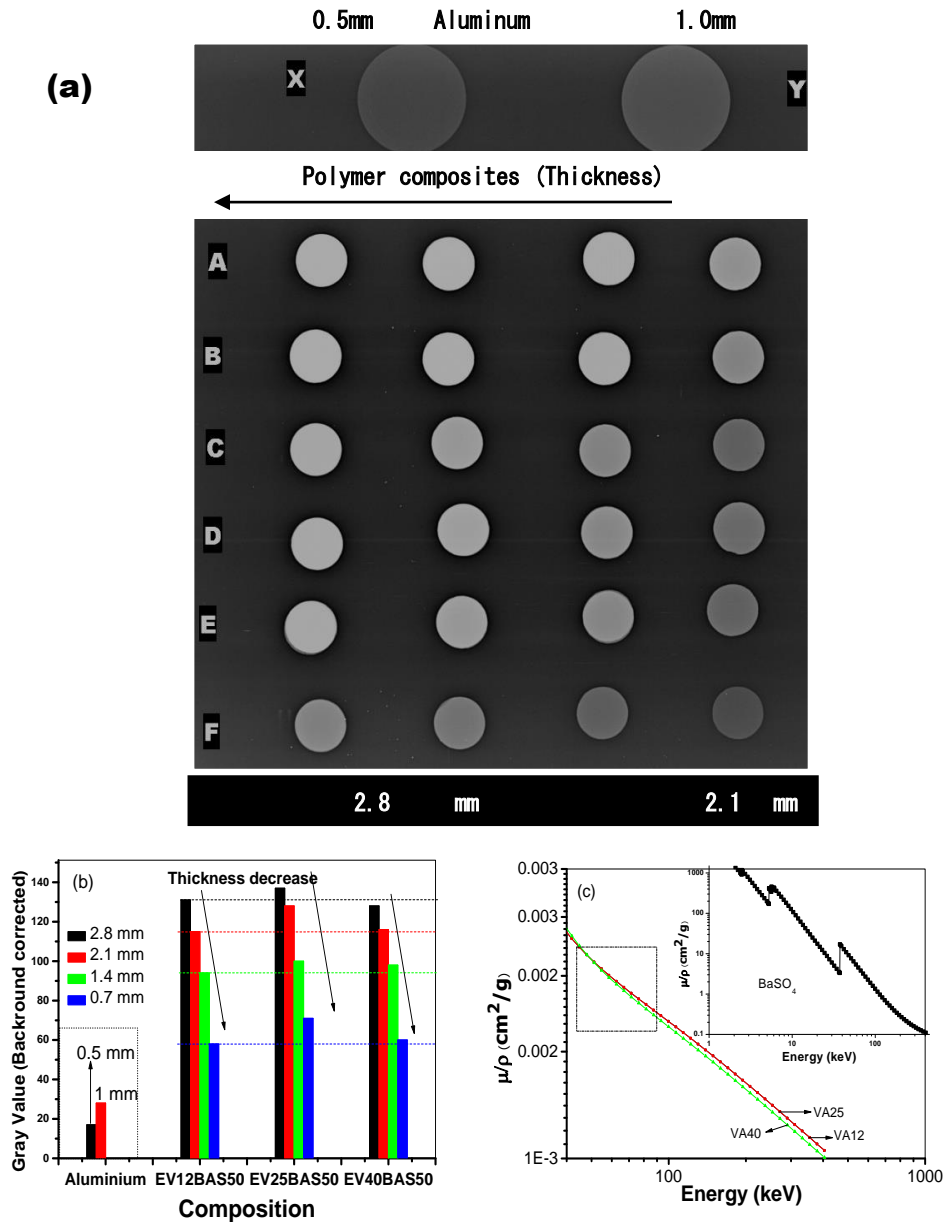


Figure 3.11: Radiopacity of the composites (i) actual x-ray radiographs of different composites, A: VA₁₂BS₇₅, B: VA₄₀BS₇₅, C: VA₁₂BS₅₀, D: VA₂₅BS₅₀, E: VA₄₀BS₅₀, F: VA₁₂BS₅₀ (ii) variation in gray values for composites with composition; dotted block presents gray values for aluminum sheets (iii) variation in mass attenuation coefficient variation of VA₁₂, VA₂₅ and VA₄₀ with x-ray energy (Inset: variation in the mass attenuation coefficient of BS with x-ray energy)

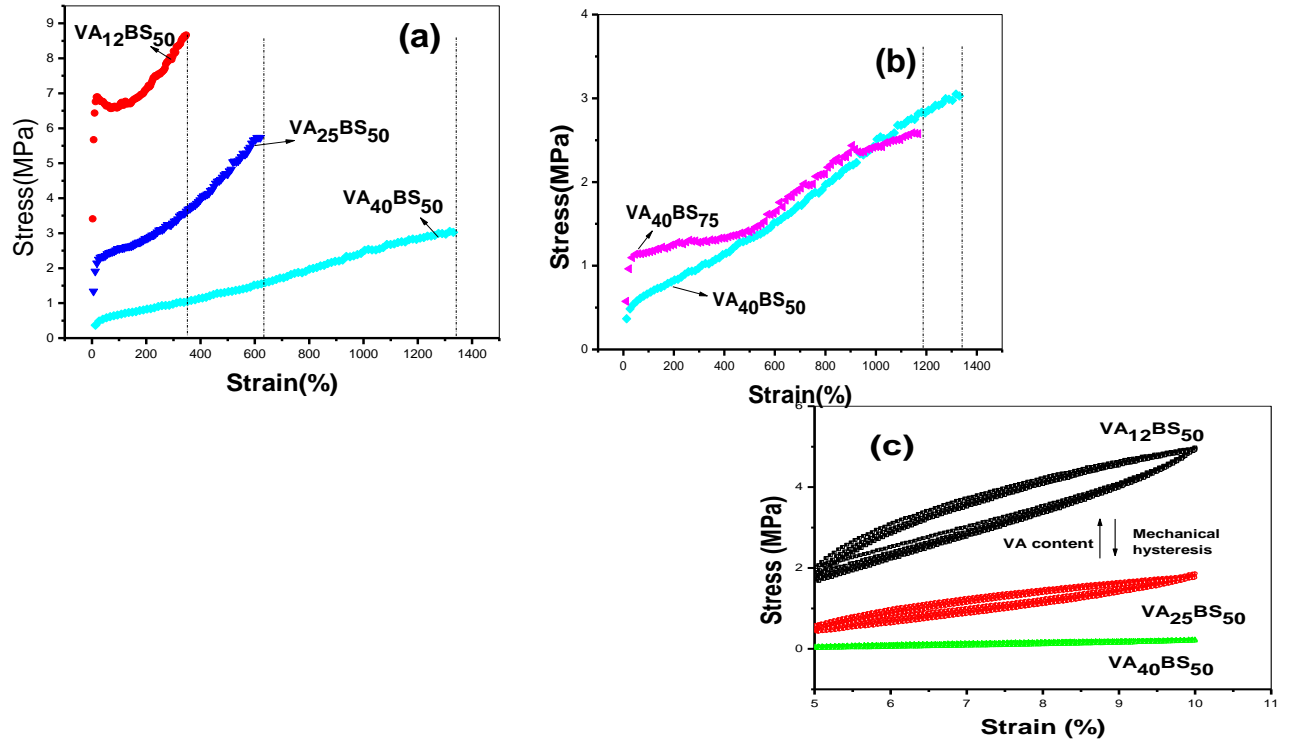


Figure 3.12: Effect of VA content on mechanical properties (a) Stress-strain profile (Left panel VA_{12} composites; right panel VA_{40} composites) (b) Mechanical hysteresis in the composites during five cyclic deformations of 5% (5-10%) strain. The arrows show mechanical hysteresis reduces with increase in VA content.

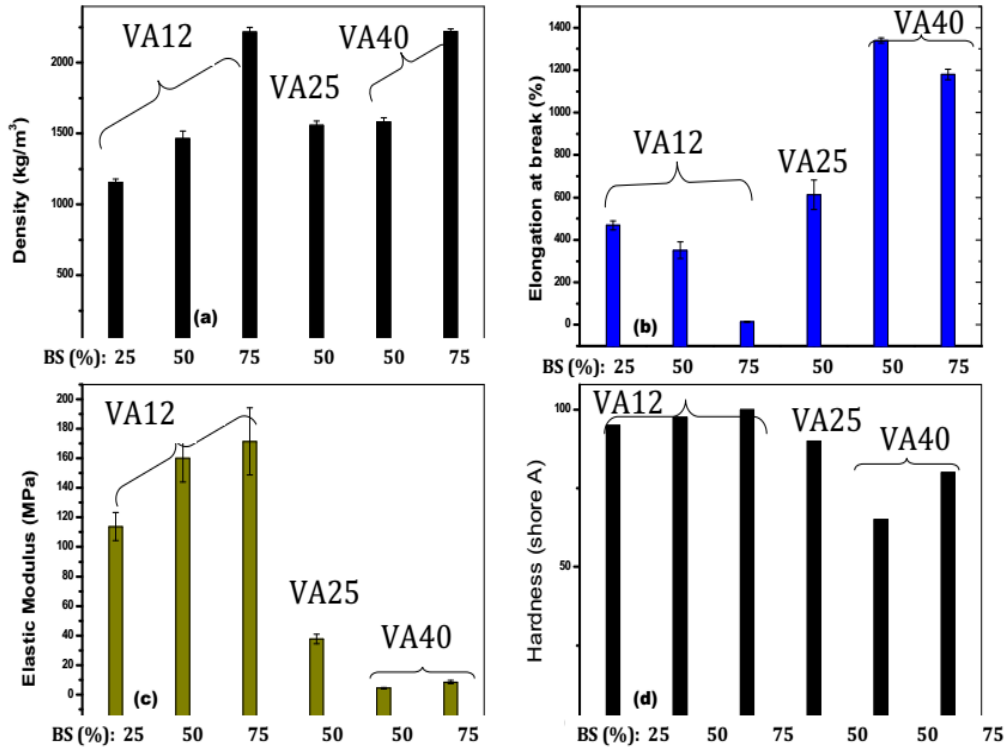


Figure 3.13: Physical and mechanical properties of the EVA/BS composite
(a) Density (b) Elongation at break (c) Elastic modulus (d) Hardness (shore
A). The properties are presented for different BaSO₄ content (%) and for
different VA content

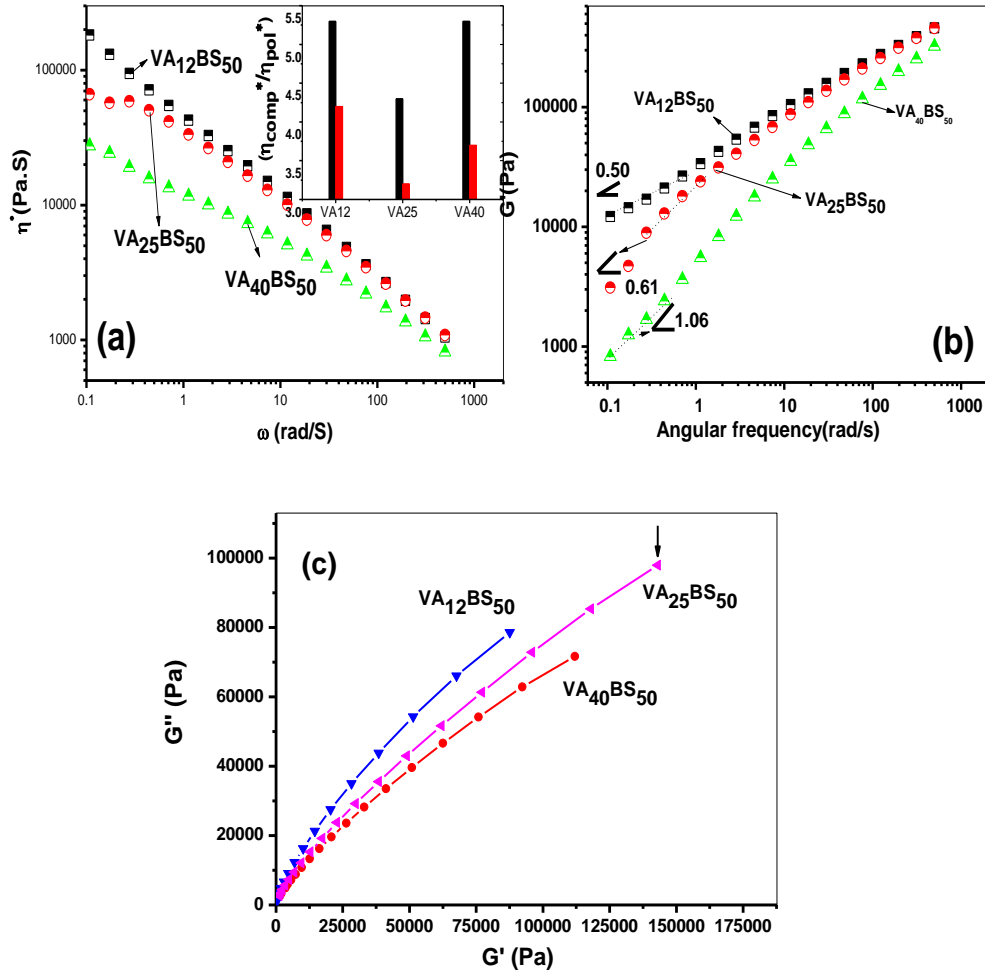


Figure 3.14: Effect of the VA content and the filler loading on (a) dependence of the complex viscosity (η^*) on angular frequency (ω) in the linear visco-elastic regime [Inset: Fold increase in complex viscosity on filler addition; defined as the ratio of complex viscosity of filled system (η_{comp}^*) to the unfilled one (η_{pol}^*)] (b) dependence of the storage modulus (G') on the angular frequency in the linear visco-elastic regime (c) Cole-Cole representations for different EVA/ BaSO₄ composites in the linear visco-elastic regime. $T=140.0$ °C, $\gamma=1\%$

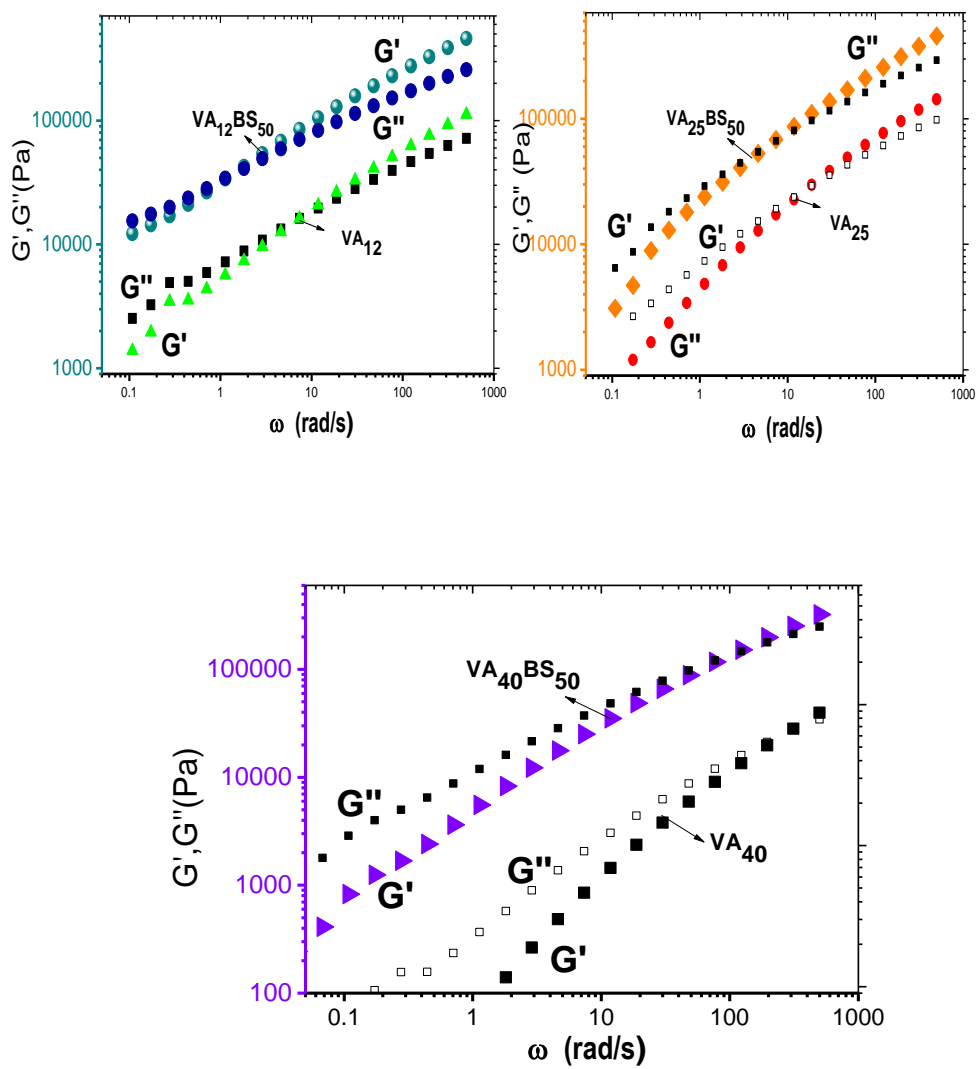


Figure 3.15: Storage (G') and loss modulus (G'') crossover for different EVA/ BaSO₄ composites. T=140.0 °C, γ =1%

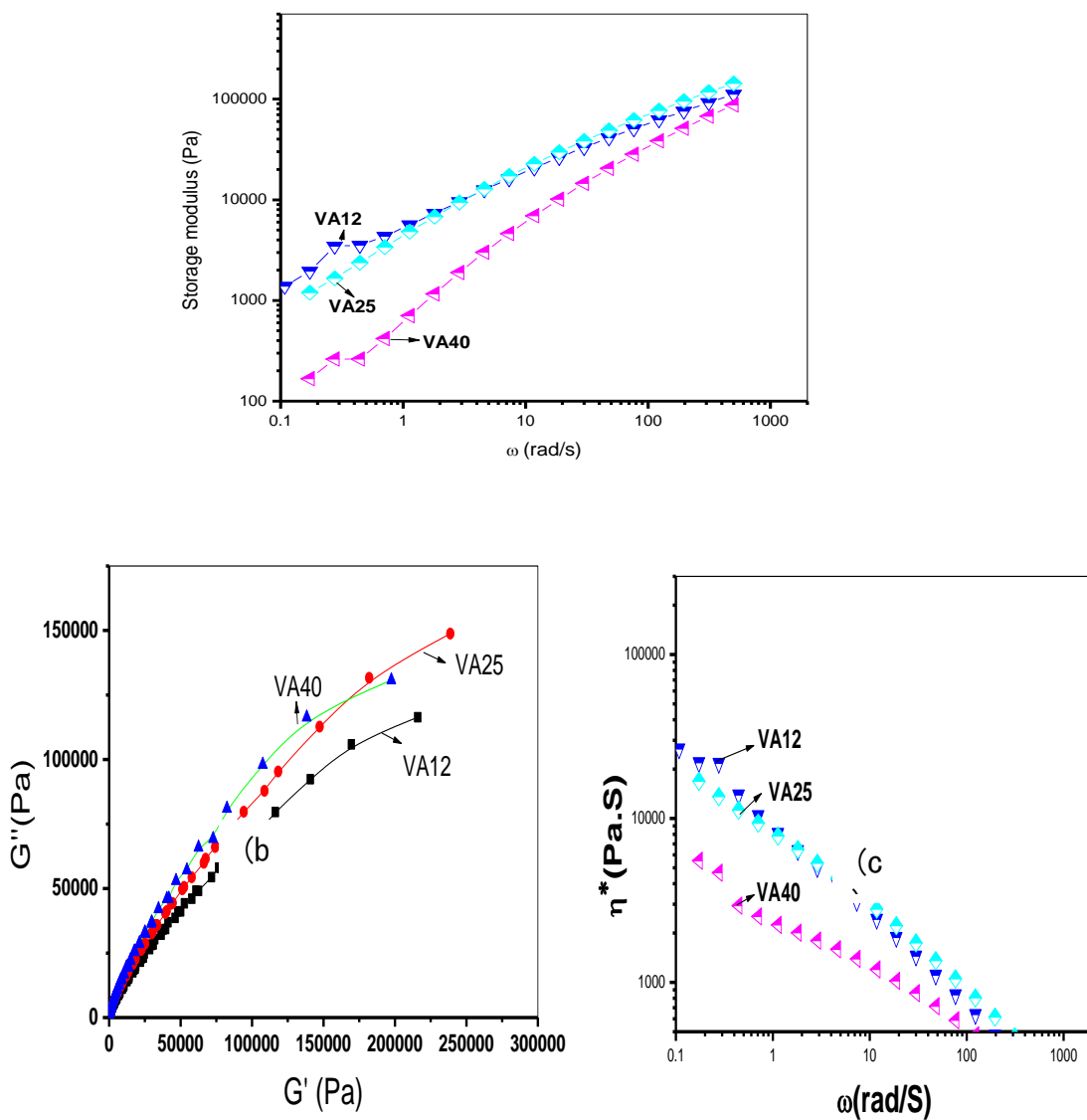


Figure 3.16: Melt rheology of unfilled systems (a) dependence of the complex viscosity (η^*) on angular frequency (ω) in the linear viscoelastic regime (b) dependence of the storage modulus (G') on the angular frequency in the linear viscoelastic regime (c) Cole-Cole representations for different EVA in the linear viscoelastic regime. $T=140.0\text{ }^{\circ}\text{C}$, $\gamma=1\%$

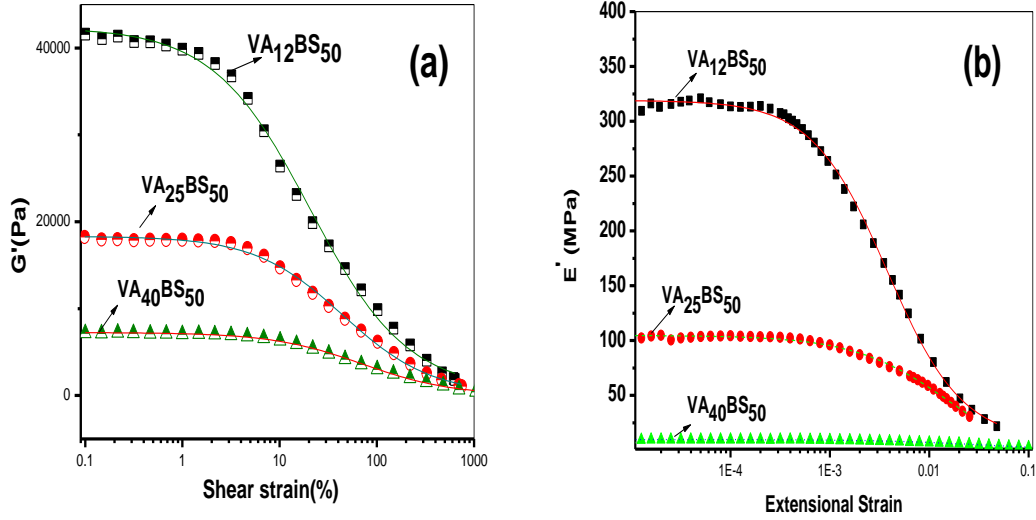


Figure 3.17: Structural breakdowns in EVA/BS composites in molten and solid states (a) dependence of the storage modulus on the small amplitude oscillatory shear strain (molten) [$\omega = 1$ rad/s, $T = 140^\circ\text{C}$] (b) dependence of the storage modulus on the dynamic tensile strain (solid) [$f = 1$ Hz, $T = 30^\circ\text{C}$]. Dotted lines represented best fit of the experimental data to phenomenological quantitative Kraus model.

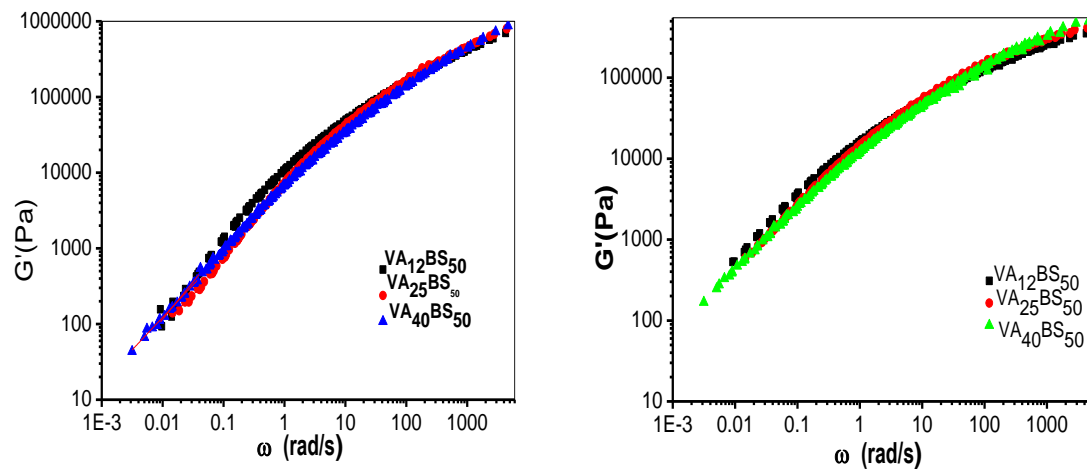


Figure 3.18: Time temperature (t-T) superimposition curves of storage and loss modulus for different EVA/ BaSO₄ composites. Reference temperature- 140°C, $\gamma=1\%$

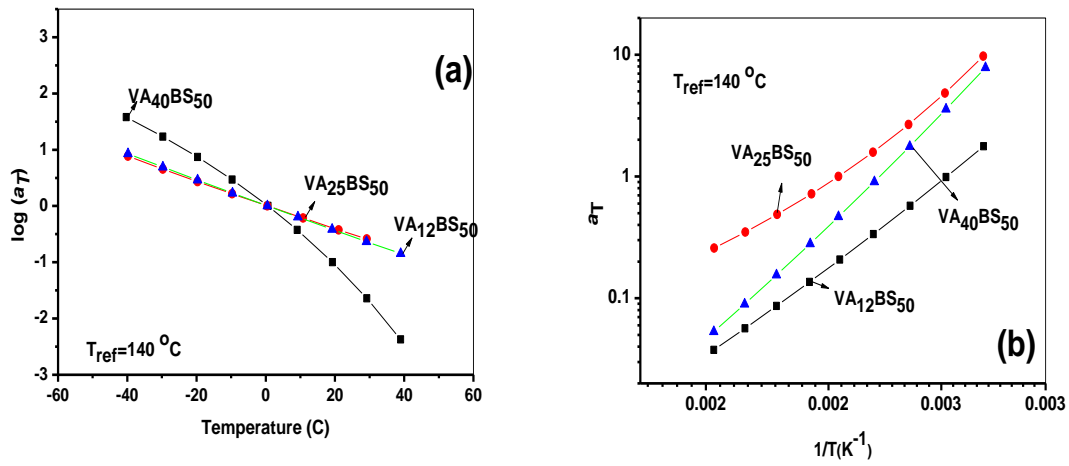


Figure 3.19: Temperature dependence and model fitting of horizontal shift factors (a_T) of EVA/ BaSO₄ composites (a) WLF model (b) Arrhenius model

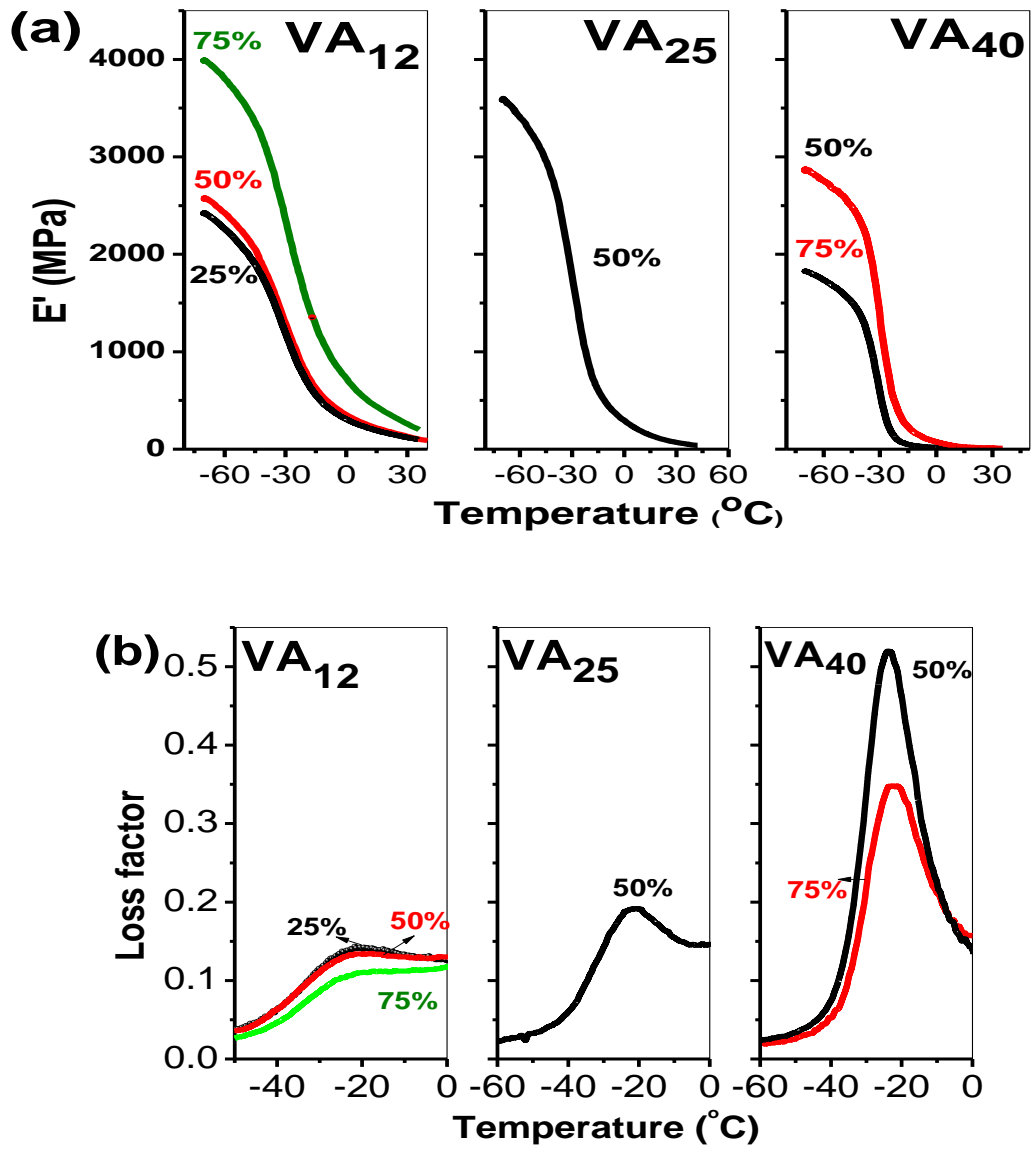


Figure 3.20: Dynamic thermo-mechanical changes in EVA/ BaSO₄ composites with the change in vinyl acetate content and BS loading (a) storage modulus versus temperature (b) loss factor ($\tan \delta$) versus temperature [% depicts percentage loading of BaSO₄ in the respective composite]

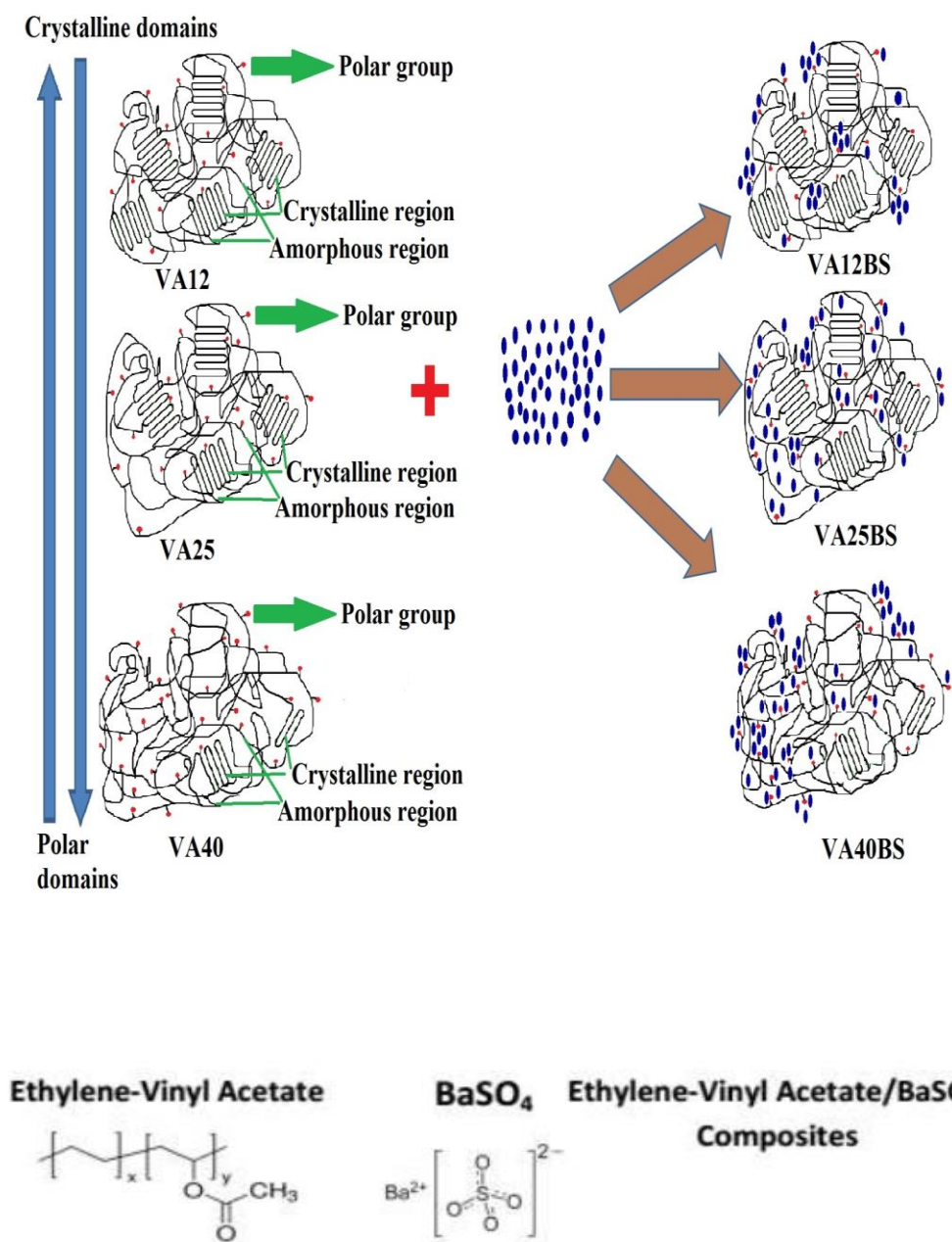


Figure 3.21: Scheme depicting interplay of crystalline domains, vinyl acetate groups, and BaSO_4 particles distribution in the matrix.

CHAPTER-4

SYNTHESIS OF A FLEXIBLE POLY(CHLOROPRENE)/METHYL RED FILM DOSIMETER USING AN ENVIRONMENT-BENIGN SHEAR COMPOUNDING METHOD

4.1. General Introduction

A detailed account of radiation attenuation and radiopacity is presented in Chapter-3 while this chapter mainly emphasises the quantification of radiation induced changes and their utilization for the estimation of radiation dose. There are many large scale facilities and research laboratories available worldwide where high energy radiation is extensively used [108,109,110]. For all such applications precise and easy measurement of radiation dose is essential to get the desired properties. However, most of the dosimeters available today suffer from many drawbacks such as expensive cost, difficulty in usage, rigid nature or involve use of hazardous air pollutants (HAPs) and volatile organic solvents (VOCs) during their synthesis [109,111-114]. To overcome these, there is a pressing need for developing low-cost, flexible radiation dosimeters synthesized through a solvent free route with reliable absorbed dose response.

Polymer film based dosimeters are widely used in radiation processing. Such dosimeters generally contain a transparent polymer matrix doped with dyes [115-119] which are either radio-chromatic (i.e. its λ_{max} shifts with radiation treatment) or undergo bleaching due to radiolytic transformations in the chromophoric group present in the dye thereby leading to decrease in absorbance. In a recent study, Soliman et al. have explored Leuco crystal violet/poly (vinyl butyral) film for high radiation dosimetry [120] wherein a linear response in the dose range 0-20

kGy and a non-linear response at higher doses up to 100 kGy is reported. Similarly, Kattan et al. have explored the feasibility of Bromocresol purple dyed polyvinyl chloride (PVC) films for dosimetric studies and reported linear response up to 50 kGy [116].

Methyl red (MR), an azo dye, forms one of the most extensively studied dyes for radiation dosimetric applications mainly due to its low cost and dose dependent linear bleaching [118, 121]. Ajji has explored the use of aqueous methyl red solution for gamma radiation dosimetry [121]. As MR is a pH sensitive dye, they have used both alkaline and acidic solutions to analyze the effect of pH on dosimetric parameters and reported a remarkable difference in the response of MR solution in acidic and alkaline conditions. Al Zahrany et al. have used polyvinyl butyral (PVB) dyed with MR as a radiation dosimeter [122] while Barakat et al. used MR doped poly(methyl methacrylate) (PMMA) for such applications [123,124]. Although these studies have revealed very promising results, they involve use of solvents and complex procedures [110,114,117-119,121-122,124-127] which are not preferred.

Shear/melt compounding is a routine process used for mixing polymers with desired ingredients. It is a solvent free process in which polymer mix is heated above melting point of the polymer with continuous shearing [109,125,127]. Such processes can be used for solvent-free mixing of dyes and polymers for dosimetric applications; however, in addition to various complexities associated with the degradation/radiochromic behavior of dyes in a solid-matrix, the dispersion and distribution of dye in polymer matrix are major challenges in developing dosimeters through melt compounding route [109,126]. To the best of our knowledge, no report is available where this process has been used to synthesize radiation dosimeters.

The present study reports the synthesis of a novel film dosimeter using shear compounding. The polymer matrix used is polychloroprene (CR) which is highly flexible in nature enables dosimetric application both

in multi-dimensional as well as in complex shapes and geometries [128,129]. Different concentration of dyes were incorporated in PC and their applicability as a gamma dosimeter was investigated. Efforts have been made to analyze the morphology post irradiation stability and colorimetric parameters of these systems.

4.2. Material and methods

4.2.1. Dosimeter preparation

PC and ethylene propylene diene monomer (EPDM) were procured from local suppliers (Polychloroprene M-40, Mooney viscosity 48 ± 5 , manufactured by Denki Kagaku Kogyo Kabushiki Kaisha, Japan; EPDM ethylene content 55%, manufactured by DSM, The Netherlands). Methyl red (MR) (MW 269.3) from Aldrich was used without further purification. Fig. 4.1 shows the molecular structures of CR and MR. A series of CR/MB mixtures were prepared by homogeneously mixing CR and MR at 60°C in a Brabender Plasticorder (Brabender GmbH, Duisburg, Germany). Three five-minute mixing-and-cooling cycles were used to minimize dehydrochlorination and degradation of the components. The weights of the components were carefully chosen based on their bulk density to achieve the desired contributions from the constituents to the total volume, which ensured proper filling of the mixing chamber. The homogeneous mix was cut into small pieces, which were compressed into 0.1-mm-thick $12 \times 12 \text{ cm}^2$ sheets with a compression-molding machine (150 kg/cm^2 pressure for 5 min at 60°C). In the following text, the concentrations of the dye are expressed in millimoles of the dye per 100 g of the resulted mixture.

4.2.2. Radiation source

A Co^{60} gamma radiation source Gamma Chamber GC-5000 (BRIT, India) with the dose rate of about 1.5 kGy h^{-1} (Fricke dosimetry) was used. Lead attenuators made it possible to reduce the dose rate to 0.75 and 0.375 kGy h^{-1} . Another gamma chamber, GC-900 was used to irradiate the films

at a dose rate of 3.5 kGy h⁻¹.

4.2.3. Spectrophotometer

The absorbance changes were measured with a Shimadzu UV-2500 spectrophotometer at $\lambda_{\text{max}} = 515$ nm. For each data point, four replicate measurements were made, and the average value was reported as the percentage change in the absorbance (RCA)

$$RCA = \frac{(A_{ui} - A_i)}{A_{ui}} \quad (4.1)$$

Where A_{ui} is the absorbance of an un-irradiated film and A_i is the absorbance of the irradiated film. Average of two samples for each data points has been reported. For reproducibility studies, a large number of samples were irradiated to various doses (10 samples per dose), and the relative standard deviations of the responses (RSD) were calculated.

4.2.4. Colour measurements

Reflectance measurements were performed with a Minolta CM-3600D spectrophotometer (Konica Minolta Sensing, Inc., Osaka, Japan). The reflectance in the spectrum range from 360 to 780 nm was recorded at the wavelength interval of 10 nm. A D₆₅ lamp was used as the reference light source, and the detector was oriented at an angle of 10° with respect to the light source. The equipment was calibrated before use with a standard white tile and a black box for 100% and 0% reflectance. The data were analysed with the JayPak 4808 Colour Management Software (Version 1.2; JayPak, Malaga, WA, USA).

4.2.5. Humidity standardization

The dosimeters were stored at different relative air humidities in closed vials containing saturated solutions of lithium chloride (11% R.H.),

magnesium chloride (33%R.H.), magnesium nitrate (53%R.H.), sodium chloride (75%R.H.), ammonium sulfate (80%R.H.), and potassium nitrate (94%R.H.) at 25°C.

4.3. Results and discussion

4.3.1 Effect of dye concentration and dehydrochlorination on the spectral features

Figure 4.2 shows visible spectrum of CR doped with different concentrations of MR. Pristine CR showed no significant absorption in the range 400-650 nm, whereas the polymer doped with methyl red showed strong absorption with λ_{max} at 515 nm with a small shoulder appearing at 500 nm. The absorbance increased with increase in MR concentration without any shift in peak position. The observed λ_{max} for CR /MR is very different from those of other reported systems. For PVB/MR system, λ_{max} has been reported to be around 497 nm, whereas Barakat et al., reported λ_{max} at 493 nm for PMMA/MR matrix [123]. In another system, where we have used EPDM, the λ_{max} was also observed at 495 nm (unpublished observation). The variation in the λ_{max} of the MR in CR and other matrices may be due to the fact that MR being a pH sensitive dye, its absorption profile depends to a larger extent on the pH (protonation of carboxylic group) [121]. The protonation, in presence of CR can be attributed to the presence of labile chlorine atom, which generates residual HCl in CR matrix [130]; such phenomenon, however, is not expected to play any role in EPDM, PMMA or PVB matrices.

Gamma irradiation is expected to crosslink the chloroprene matrix and also induce dehydrochlorination [131]. However, in the dose range studied here, crosslinking of the matrix is expected to be insignificant while dehydrochlorination is expected to take place in a dose dependent fashion during irradiation [132,133]. Arakawa et al. have reported an almost linear increase in the HCl release upto 1000 kGy of absorbed dose. It is interesting to note that even after irradiating to a dose of 30 kGy, the λ_{max} of the films didn't shift much which suggests that the amount of HCl released to a dose of 30 kGy does not have any significant effect on the protonation of methyl red. This corroborates our assumption for the observed λ_{max} ; because in the absence of residual HCl or labile chlorine, the release of HCl during irradiation would have significantly altered the pH of the system which in turn, would influence protonation and spectral features of MR significantly. For CR-MR matrix irradiated to different absorbed doses, the λ_{max} did not shift with increase in dose, though the absorbance decreased in dose dependent manner and finally disappeared at ~48 kGy. Various studies have been reported on the bleaching behavior of MB in different solvents and polymer matrices [121,123,134]. The effect of ionizing radiation induced bleaching of azo dyes is expected to be irreversible as it is attributed to cleavage of azo group. Most of the studies on azo dyes highlight that dose range and the rate of bleaching strongly depend on the solvent or polymer matrix used [121,130].

4.3.2. Effect of composition on dose range and sensitivity

Polymer matrices of different CR-MR compositions were exposed to different absorbed doses of gamma radiation. The relative changes occurring in the absorbance of the samples is presented in figure 4.3 and its inset showing relative change in absorbance with dose of the film containing 0.12 mM of MR/100 g of CR. In the blank CR and at lower (<0.06 mM/100g of CR) MR concentration, no consistent measurable change in the absorbance was observed (Table 4.1) and was therefore ignored. For higher concentrations of MR, the initial absorbance was very high thereby limiting their application in transmission mode. Dehydrochlorination is supposed to impart yellowing in the CR matrix due to conjugated double bond formation [131]. However, in the dose range studied no such yellowing was observed. Contrary to the reported results of Al Zahrany et al., [122] who used polyvinyl butyral films containing different concentrations of MR, we did not observe any improvement in the sensitivity even with the increase in dye concentration for all CR-MR compositions within the studied concentration range [122]. This may be due to the difference in the basic process followed during synthesis as well as due to inherent differences in the radiation chemistry of the base matrix [118]. To get further insight into color developed/disappeared during radiation treatment, color coordinates of the CR/MR dosimetric films were investigated.

4.3.3. Effect of radiation dose on color coordinates

The change in color of CR-MR matrices was studied in terms of CIE (International Commission on Illumination) color spaces. The parameters used were CIE L^* (Lightness), a^* (Redness), b^* (Yellowness) and overall color difference (ΔE). L^* denotes the amount of light or luminance of the sample. The symbols a^* , b^* precisely denote the values in a green to red and a blue to yellow color scale, respectively. These color indices are based on opponent theory of color vision and have a huge impact on the perception of color. We use these indices to quantify overall perception of color. For the matrix containing 0.06 mM of MR/100 g of CR with $a^*=5.22$, $b^*=1.43$ and $L=5.5$ the value changed to 4.22, 1.35 and 4.50 respectively on exposure to the dose of 10kGy. Both samples(un-irradiated and irradiated) showed high positive value of a^* suggesting the presence of redness even in the sample irradiated to 10 kGy, though there was a reduction of about 20% in absorbance value. Overall perception of color was assessed by determining overall color difference using following relation

$$\Delta E = \sqrt{(\Delta L^*)^2 + (\Delta a^*)^2 + (\Delta b^*)^2} \quad (4.2)$$

where ΔL^* , Δa^* and Δb^* are the differences in the value of L^* , a^* , and b^* of test sample from the reference sample, respectively. ΔE at 10 kGy was found to be 1.26. With the same radiation dose, changes in the pristine CR were negligible and no color was developed. However, at higher doses

(>50 kGy), yellowing and browning of films were observed suggesting that these films might not be suitable for dose greater than 50 kGy. It may however be noted that, color changes at dose greater than 50 kGy were intense and there was deterioration in the transparency of the films. This observation suggests the potential applications of CR/MR films as dosimetric labels for high dose applications. These results including the implications on dosimetric studies involving high dose labels will be published in detail in the next part of the study.

4.3.4. Reproducibility of radiation response

The sensitivity was evaluated from linear dose versus absorbance curve by determining slope and regression coefficient value. The coefficient of variation (CV) was defined as

$$CV = \frac{100s}{k} \quad (4.3)$$

Where s is standard deviation and k is specific optical absorbance at 520 nm wavelength [135]. The slope and regression coefficient for all compositions are presented in the Table 4.1 and % precision and CV values for different compositions are shown in Table 4.2. Which clearly reveals the suitability of CR/MR films in the field of radiation dosimetry.

4.3.5. Effect of dose rate

Dose rate is known to affect the recombination of primary radicals generated during radiolysis as well as change the spur chemistry. It is therefore, important to see whether there is any change in the response of

CR /MR films when exposed to gamma radiation at different dose rates. The effect of dose rate was investigated using different lead attenuators in Co-60 gamma chamber. The dose rate was varied from 0.375 kGy/hr to 3.5 kGy/hr. Dosimetric film containing 0.06 mM MR/100g CR was irradiated to a fixed dose of 10 kGy at room temperature. It can be seen from figure 4.4a that the response of the dosimeter was independent of the dose.

4.3.6. Effect of humidity and temperature

To understand the effect of humidity during radiation, the vials were exposed to 25 kGy of radiation dose. It can be seen from inset figure 4.4 that there is no appreciable change in the response up to 53% relative humidity, while there was a slight change at 75% and significant changes thereafter. On the other hand, no significant effect of temperature in the range 25-70°C was observed. Similar findings have been reported earlier for other polymer/dye based dosimetric systems [137-138]. It may be noted that the glass transition temperature of polymer used lies in sub-room temperature range (~-50°C); therefore, macromolecular dynamics would not lead to any profound change particularly in the temperature range under study. Moreover, CR being an amorphous polymer shows change in the absorbance with increase in temperature due to the melting of crystallites which are not expected to contribute to the optical parameters of the films [125,138].

4.3.7. Effect of storage duration

The dosimeter containing 0.06 mM MR/100g PC was irradiated to 10 kGy and kept under normal laboratory light. There was no significant decrease in the absorbance during storage (figure 4.4). The relative changes in the absorbance were measured periodically over a certain number of days which was found to be less than 5% although there was no specific trend followed. This suggested that the observation was an experimental variation rather than bleaching of dye under the influence of laboratory light conditions.

4.3.8. Processing parameters and optical microscopy

Unlike solution mixing, in shear compounding [139], it is very difficult to achieve good distribution and dispersion of dye in a polymer matrix. In this study, the mixing program was designed in a way so as to avoid (or minimize) degradation of dye or polymer matrix due to the heat generated during shear compounding. Maximum torque generated during the mixing was 5 Nm. Optical micrographs of different films have been shown in figure 4.5. It can be seen that up to 0.30 mM of MR/100g of CR, the distribution was quite good homogeneous. This phenomenon was interesting in the sense that good dispersion demands good polymer-dye interaction. In another system, which involves EPDM elastomer (figure 4.5 a,b,c, d), it was found that that even at 0.06 of MR/100g of polymer, agglomeration could be seen and at 0.30 mM of MR/100g of polymer, highly inhomogeneous distribution of MR was observed. This observation reflects the importance of selection of suitable polymer-dye system for

dosimetric applications. MR being polar, has limited miscibility with EPDM, whereas its miscibility with polar PC is quite good, making it a good choice for dosimeter. Figure 4.6 shows photographs of irradiated (30 kGy) and un-irradiated films, containing 0.06 mM MR/100g PC. It can be seen that such films can also be used as dosimetric labels.

4.4. Summary

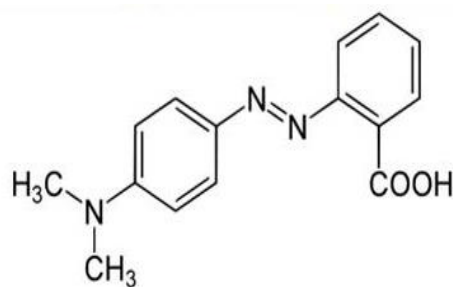
Radiation effects on a dye doped polymer composite were elucidated. The composite showed dose dependent decoloration upto 30 kGy. Optical micrographs suggested good dispersion of dye in the polymer matrix. The effect of various parameters such as variation of dose rate, temperature etc. was investigated and the same was found to be insignificant. The precision of CR/MR film dosimeters was very good and the percentage fluctuation was less than 5% over the entire range of dose studied. It can be inferred that such systems find good potential as a prospective dosimeter in the field of radiation dosimetry.

Table 4.1: Linear fitting parameters for PC/MR dosimetric films

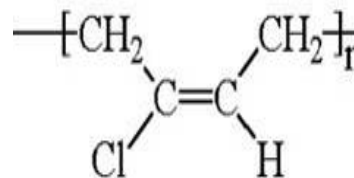
Composition mM/100g of polymer	Slope (kGy⁻¹)	Intercept	Regression coefficient
0.04	0.07	0.01	0.88
0.06	2.18	0.00	0.98
0.12	1.44	0.45	0.99
0.14	1.54	-0.05	0.99

Table 4.2: Reproducibility of relative change in absorbance at different doses (0.12 mM of MR /100g PC)

Dose (kGy)	SD	% precision	Coefficient of variance (CV)
10.6	0.42	3.97	28.2
18.5	0.56	3.04	16.3
23.4	1.12	4.79	12.8
29.6	1.36	4.60	10.1



Methyl red



Polychloroprene

Figure 4.1: Molecular structures of Methyl red and Polychloroprene

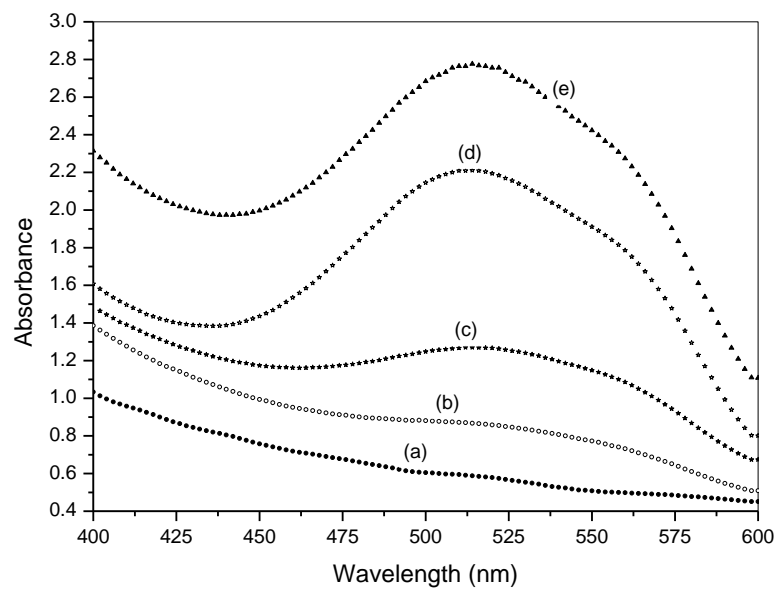


Figure 4.2 : Visible spectrum of CR doped with different concentrations of MR/100g CR (a) 0 mM (b) 0.02 mM (c) 0.04 mM (d) 0.06 mM (e) 0.12 mM

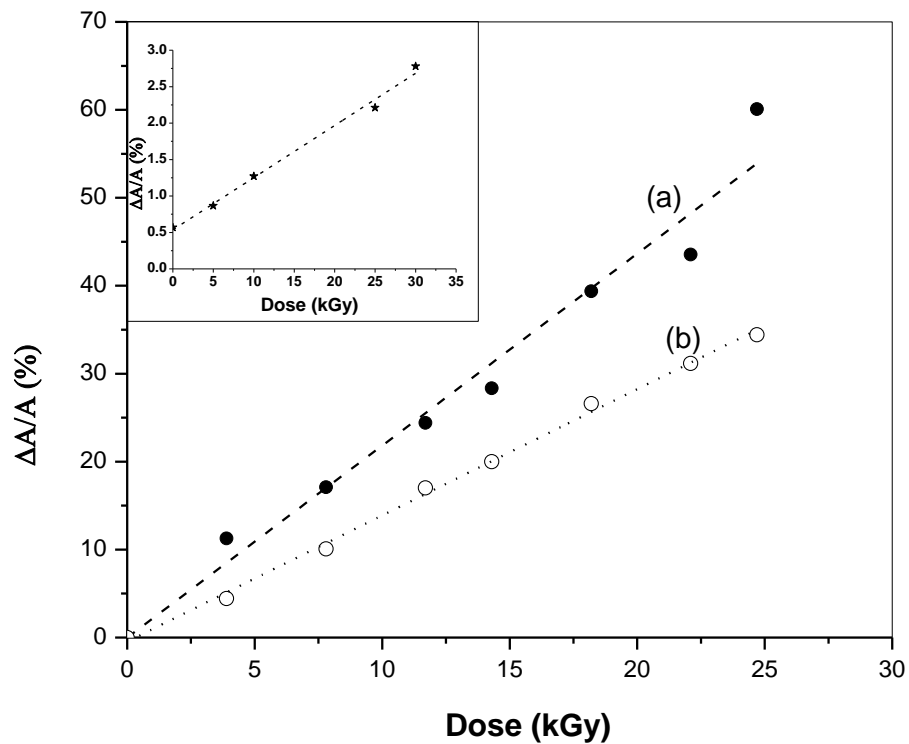


Figure 4.3: Relative change in absorbance with radiation dose for the film containing (a) 0.04 m M of MR/100 g of CR (b) 0.06 mM of MR/100 g of CR. Inset: Relative change in absorbance with radiation dose for the film containing 0.12 mM of MR/100 g of CR

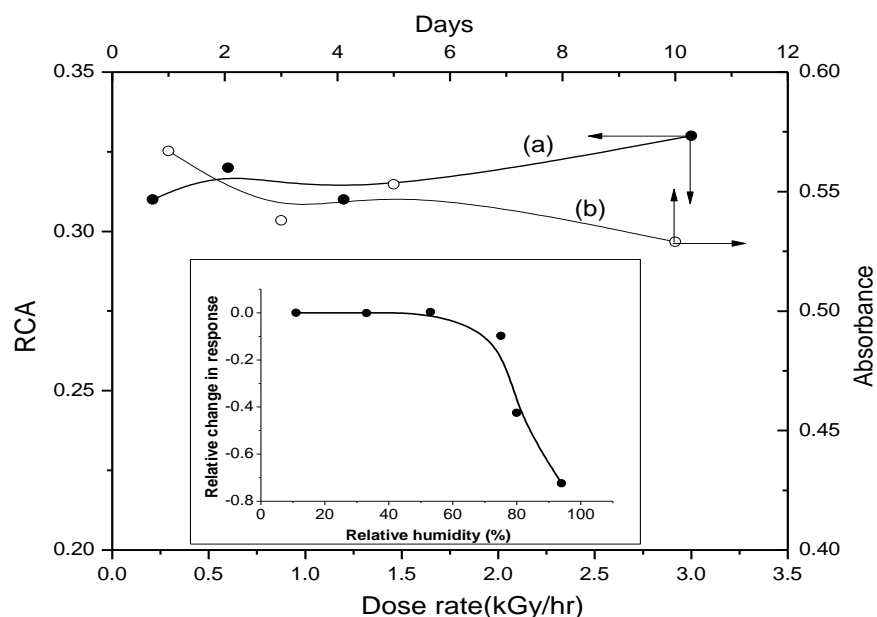


Figure 4.4: Changes in polymer films (0.06 mM of MR/100 g of CR) irradiated to 10 kGy. (a) Relative change in absorbance $[(RCA \text{ at } 0.21 \text{ kGy/hr} - RCA \text{ at specific dose rate}) / RCA \text{ at } 0.21 \text{ kGy/hr}]$ at different dose rates. (b) Relative change in absorbance kept under laboratory light conditions. Inset: Relative change in absorbance $[(RCA \text{ at } 11\% \text{ humidity} - RCA \text{ at specific humidity}) / RCA \text{ at } 11\% \text{ humidity}]$ for polymer films (0.06 mM of MR/100 g of CR) irradiated to 10 kGy at different humidity

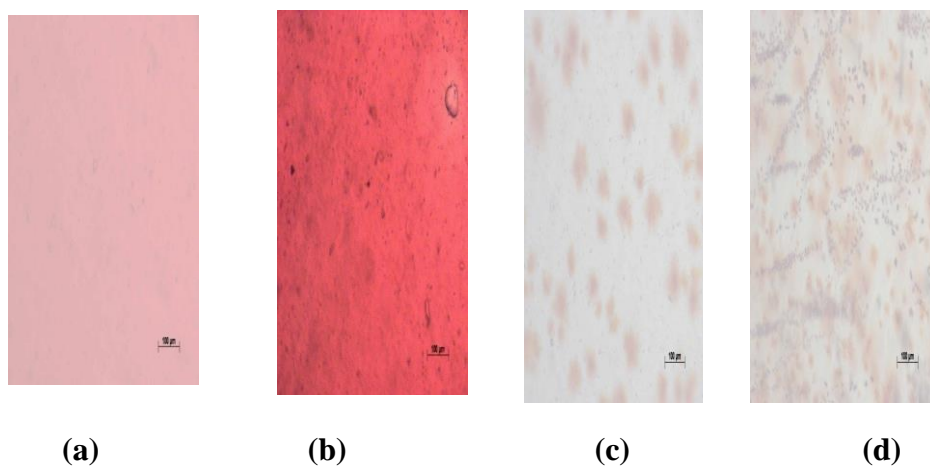


Figure 4.5 Optical micrograph of polymer films made using two different polymer systems and two MR concentrations (a) 0.06 mM of MR/100g PC (b) 0.30 mM of MR/100g PC (c) 0.06 mM of MR/100g EPDM (d) 0.30 mM of MR/100g EPDM [The scale bar shows 100 micrometer]

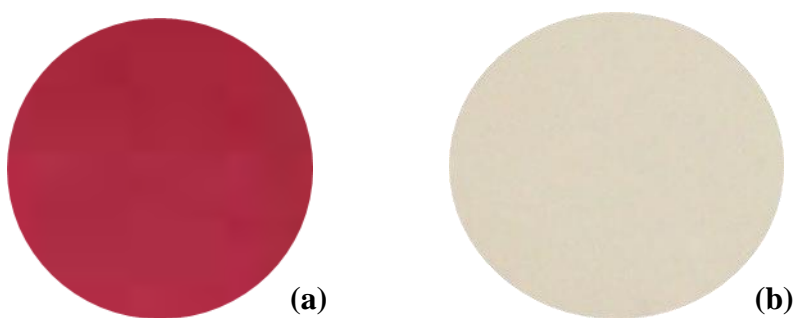


Figure 4.6: Photograph of films loaded with 0.06 mM of MR/100g CR (a) unirradiated (b) irradiated to 30 kGy

CHAPTER-5

Melt compounded ethylene vinyl acetate / magnesium sulfate composites as flexible EPR dosimeters: mechanical properties, dose response and processability

5.1 General Introduction

Easy and accurate assessment of radiation dose is critical in radiation processing and radiotherapy applications [108,140-143]. Previous chapter discussed the effect of radiation in a dye doped polymer composite with a view to exploring its suitability as a radiation dosimeter. For radiation dosimetry, EPR has gained prominence due to higher sensitivity and stability and alanine based EPR is considered as gold standard in dosimetric applications [144-146]. However, alanine suffers from its not very high sensitivity, largely because the area of alanine ESR signal shared by many lines of the complex spectrum. That decrease the intensities of ESR signal lines and, accordingly, the signal-to-noise ratio. That is why a quest for dosimetric material with fewer spectral lines continues and there is an increasing interest in exploring newer dosimetric material which has less complex ESR signal [147].

Lelie et al. investigated the suitability of lithium formate hydrate in EPR dosimetry [148] whereas Nakagawa et al. studied radical produced in sucrose for dosimetric applications [149]. Sulfate radicals have been

explored by several authors in such applications [150-151]. Strontium sulfate has been studied by Rushdi et al. and was found suitable for the dosimetric measurements in the dose range 1-100 Gy [152]. Tani et al. [153] investigated the EPR signal of irradiated magnesium sulfate heptahydrate. It was seen that these radiation induced ions have relatively simpler EPR spectrum, with good stability and broad dose range [150-151,153].

Most of the approaches used for synthesis of dosimeter materials are either in powder form or binder based [154-156]. Such technique involves batch process and use of toxic VOCs in the synthesis [157]. Melt compounding is an additive free approach that can be used in such applications; however, very few reports exist in literature citing the exploration of this technique for the synthesis of radiation dosimeters [158-159]. The major constraints associated with this method are the dispersion and processability of such composites [160]. A filler may agglomerate when loading exceeds a certain threshold value, which depends on its inherent characteristics of filler and interaction of filler with the polymer matrix. Also, introduction of filler may drastically change temperature and torque requirement for mixing, which may make the process technologically unfeasible [80].

This study reports the development of novel polymer based dosimeters for radiation processing applications. Mechanical, physical and processing properties of the composites were investigated and dosimetric response was analyzed. Further, efforts were made to understand water equivalence and reproducibility of these dosimeters.

5.2. Materials and method:

5.2.1. Material and sample preparation

MGS and EVA (VA content 40%) were procured from Aldrich, and used as such. A series of EVA/MGS composites were prepared by melt compounding in Brabender plasticorder at 100°C. The homogeneous mix was cut to small pieces and compressed into sheets of size 20×20 cm² of different thicknesses using compression-molding machine at 150 kg/cm² pressure for 5 minutes at 100°C.

For ESR studies the sheets formed (with MGS content of 50%) were cut into small pieces using a household scissors. The cut mass was put in melt flow index tester heated up to 120°C having suitable exit orifice. On putting a load of 5 Kg, melt fracture free composite in form of smooth cylindrical thread of diameter 4mm was obtained. The thread so obtained was cut into pieces of length 5mm irradiated to desired doses and used for ESR studies.

5.2.2. Radiation source

Gamma chamber GC-5000 with ⁶⁰Co gamma-source, supplied by M/s BRIT, India was used for irradiation purpose with suitable lead attenuators. The gamma chamber (GC) has an irradiation volume ~5000 ml with height=20.5 cm and diameter =17.2 cm. The irradiation shell of GC is made of stationery source pencils, cylindrically placed stainless steel (SS) pencils containing Co-60 gamma source put vertically to form irradiation space of cylindrical geometry. The source remains stationery

enveloped in lead shielding. GC is equipped with vertically moving SS shaft arrangement which has space (irradiation volume) to load samples. After sample loading shaft is moved down and the irradiation space perfectly sits in the cylindrical gamma source assembly for irradiation for desired time. The dose mapping of the gamma chamber was done using Fricke dosimetry. The details of Fricke dosimeter preparation and measurement are well documented elsewhere [161]. In order to map the absorbed dose in the irradiation space nine glass vials containing about 6-7 ml of Fricke solution were fixed to a rectangular thermocole sheet (which could fit into the centre of irradiation chamber vertically). Three vials equidistant from each other were placed at upper and lower ends and three along the horizontal axis. This arrangement was done in order to determine the dose variation in the radiation chamber along vertical and horizontal axis. Three sets of dosimeters were irradiated for different duration of times and absorption due to Fe^{3+} ions generated radiolytically was measured immediately after irradiation. The radiation dose at the centre of the gamma chamber was found to be $1.12 \pm 0.03 \text{ kGy hr}^{-1}$. In comparison to the dose in centre significant difference in dose rate was observed at other 8 points chosen. However no observable difference in dose rate was observed in the horizontal plane of 8mm radius around the centre of the gamma chamber. As far as possible, samples of the developed dosimeter were irradiated at the centre of gamma chamber and the dose at the center of the gamma chamber was assumed to be the dose delivered to

the samples. For present study for each dose 5 samples of almost same dimensions were irradiated in such a way that all samples were in same horizontal plane around central axis during irradiation.

5.2.3. Physico-mechanical properties

For tensile strength measurements at least five dumbbell shaped specimens were cut out from nano-composite sheets using a sharp edged steel die of standard dimensions. The thickness of the samples were determined to the nearest of 0.1 mm. The tensile strength and elongation at break were measured using a universal testing machine supplied by M/s HEMETEK, Mumbai, INDIA at crosshead speed of 100 mm/min at room temperature. Density of the samples was determined by displacement method as per the ASTM D792-08.

5.2.4. ESR studies

For ESR studies samples were irradiated in sealed microfuge polypropylene tubes to desired doses and at least five samples were irradiated for each dose. ESR signal was recorded within 2-3 hours of irradiation. In between the irradiation and signal measurement microfuge tubes were kept as such under room condition (Temp 24-26°C).

The ESR spectra was recorded using a Bruker EMX series spectrometer (EMM-1843) operating at X-band frequency (9.5 GHz) with 100 KHz field modulation having amplitude low enough to get distortion free line shape. The microwave power was adjusted so as to obtain unsaturated first order derivative ESR spectra. DPPH was used as

g-marker. For dosimetric studies, identical set of parameters were used: the central field: 3360 G, microwave power 0.586 mW; microwave frequency: 9.37 GHz; modulation width 500 G and time constant 20.48 ms.

5.3 Results and discussion

5.3.1. Mechanical properties, melt flow index and density

The elongation at break, tensile strength and elastic modulus of composites containing different loading of MgSO_4 (MGS) is shown in figure 5.1. It is evident that elastic modulus increased significantly, whereas tensile strength and elongation at break decreases. Up to 40 wt% loading, the rise in elastic modulus was around 100%; however at 80 % loading, the elastic modulus increased about 2100% suggesting a significant reinforcement of the matrix. Elongation at break, however, decreased significantly at 80% loading; it was around 600% at 40 wt% loading and just 4% at 80% loading.

Melt flow is a good indicator of processability [162]. Though, EVA used in this work is thermoplastic in nature, addition of MGS is expected to affect its flow behavior by affecting melt viscosity [110]. Figure 5.2 shows melt flow index of composites containing different loading of MGS. It can be seen that there is a significant reduction in melt flow index. The nano-composites containing more than 50% of MGS had extremely low melt flow index and therefore was deemed unsuitable. There was 10%, 18% and 50% reduction in melt flow index at the concentration of 10%, 20% and 40% MGS. However with further 10% increase in MGS content, the MFI decreased to almost 80% of the initial value. Since, for dosimetric applications, the content of MGS should be as high as possible, 50 wt% MGS composites were used. Variation in density along with increase in MGS content is shown in figure 5.3. The

density increased sharply after 40% loading of MGS. The density of the polymer composites can be predicted in terms of weight fractions of the component and their intrinsic densities, as depicted by following equation

$$1/\rho_c = w_{MGS}/\rho_{MGS} + (1 - w_{MGS})/\rho_{EVA} \quad (5.1)$$

where ρ_c is the theoretically determined density of the composite whereas ρ_{MGS} , ρ_{EVA} are the densities of the MGS and the EVA respectively; w_{MGS} is the weight fraction of the MGS[123,163]. Dotted line in figure 5.3 depicts the values predicted by the above equation. It can be seen that the experimental values matched well with the calculated values over the entire composition, suggesting good interaction between components and absence of void formation [82-83]. It must be mentioned here that, at higher loadings (≥ 50 wt %) slight negative deviation was observed in the density which can be attributed to the agglomeration of MGS with increase in its volume fraction.

5.3.2. ESR signal and power dependence

The ESR spectra of irradiated and un-irradiated composites are shown in figure 5.4. It can be seen that the un-irradiated composite did not have any signal as against the irradiated samples that showed good signal in a dose dependent fashion. The signal observed was isotropic with a g value of 2.0036 and a peak-to-peak width of 0.4 mT. With an increase in the radiation dose, there was no change in the peak position suggesting no new radical centers are created with an increase in the dose. The signal was assigned to sulfite radical ($SO_3^{\cdot-}$) on irradiation, a vacancy of oxygen is created in SO_4 - tetrahedron leading to the formation of $SO_3^{\cdot-}$. The unpaired electron occupies sp^3 hybridized orbital centered on the sulfur atom. This assessment matches well the recent study carried out by Tani et. al on the dosimetric relevance of hydrated magnesium for the

estimation of age of formation of icy material on Europa's surface [153]. Intriguingly however, the observed signal is slightly different from the perfectly signal-line spectrum reported by Morton et. al [151]. One possible reason for this disagreement could be the fact that, Morton et al. have used anhydrous magnesium sulfate; however in the present case there is a less but unavoidable possibility of moisture absorption during processing viz compounding. It must be emphasized that symmetry of magnesium sulfate varies with the degree of hydration, for example it changes from orthorhombic to monoclinic with the loss of just one water molecule. The dose dependence of the signal is discussed in the subsequent sections.

The effect of microwave power on the peak-to peak height (H_{PP}) of the dosimeter is shown in figure 5.5. The figure presents variation in the signal intensity with the square root of microwave power. The signal intensity increases with increase in power almost linearly up to 0.58 mW and saturates thereafter. Microwave power of 0.58 mW was therefore used for all studies.

5.3.3. Linearity, fading and reproducibility

The effect of radiation dose on H_{PP} is shown in figure 5.6 a and b. MGS signal has been reported to saturate around 10 kGy, therefore the gamma irradiation dose range of investigation was limited from 3 Gy to 4 kGy. The optimization and validation of the dosimeter for low dose and high dose measurements will be a part of another study. The dose-signal response of the dosimeter was found to be linear between 18 Gy to 4 kGy, and the response between 3 Gy to 18 Gy was not dose dependent (sublinear). The lower limit of dose determination found in this study is higher reported by Morton et. al [151], which is not surprising because our dosimeter contains only 50 wt%, MGS. Nevertheless, the materials appears to be suitable for dose measurements in the range from 18 Gy to 4

kGy which can be useful in various radiation processing applications, especially in food processing.

Fading characteristics of the dosimeter are shown in figure 5.7. The loss in the signal (H_{pp}) w.r.t reduction in signal intensity was monitored for a period of around 140 days. There was just 20% of fading in 32 days which further increased to around 40% over a period of about 140 days. To check the reproducibility of the dosimeter, ten dosimeters were irradiated at a fixed dose of 4 kGy. The relative standard error in the dose measurement was found to be 6 % at a 95 % confidence level. A more detailed analysis of the same dosimeter left intact in the cavity was 0.7%, the RSD of 5 measurements of the signal of the same dosimeter with rotation of the sample tube in 75° of intervals was 1.3% and the RSD of the signals of the same dosimeter taken out and put back into immobile sample tube was 0.7%. The results indicate that such dosimeters have good reproducibility and fading characteristics, though fading characteristics are not as good as reported in alanine dosimeters.

5.3.4. Water equivalency

In the dosimetric assessment, it is important that the dosimeter has water equivalency in the targeted energy range [145, 164]. The mass energy absorption coefficient (μ_{en}/ρ) of both the phases in the composite i.e. MGS and EVA were calculated and compared with μ_{en}/ρ of water [145, 150, 164]. It can be seen from figure 5.8 that (μ_{en}/ρ) decrease with increase in radiation energy and there was a good overlap between (μ_{en}/ρ) of EVA and of water over the entire energy range. Figure 5.9 shows (μ_{en}/ρ) for MGS and water; unlike EVA, there was a significant difference in (μ_{en}/ρ) of MGS and of water, in the energy less than 100 KeV. This might be attributed to the presence of relatively higher atomic number elements in MGS. Nonetheless after 100 keV energy, there was perfect overlap between water and MGS as well, suggesting that such dosimeters can be

considered water equivalent for used for ^{60}Co and ^{137}Cs processing and might not be suitable for low energy applications ($<100\text{ KeV}$).

5.3. Summary

Melt compounded EVA/MGS composites were developed using melt compounding and their application in radiation dosimetry was demonstrated. Mechanical properties greatly influenced with the addition of MGS in EVA matrix, indicating improvement in the elastic modulus and decrease in the elongation at break. Composites greater than 50 wt % of MGS did not show flow behavior during melt flow measurement and the specific gravity of the composites increased with an increase in MGS content. The dosimeter displayed linear response between 20 Gy and 4 kGy. The response was reproducible with around 20% fading in 32 days period. The composite was water equivalent for the energy greater than 100 KeV. These results underscore the suitability of melt compounded EVA/MGS composites for radiation processing applications.

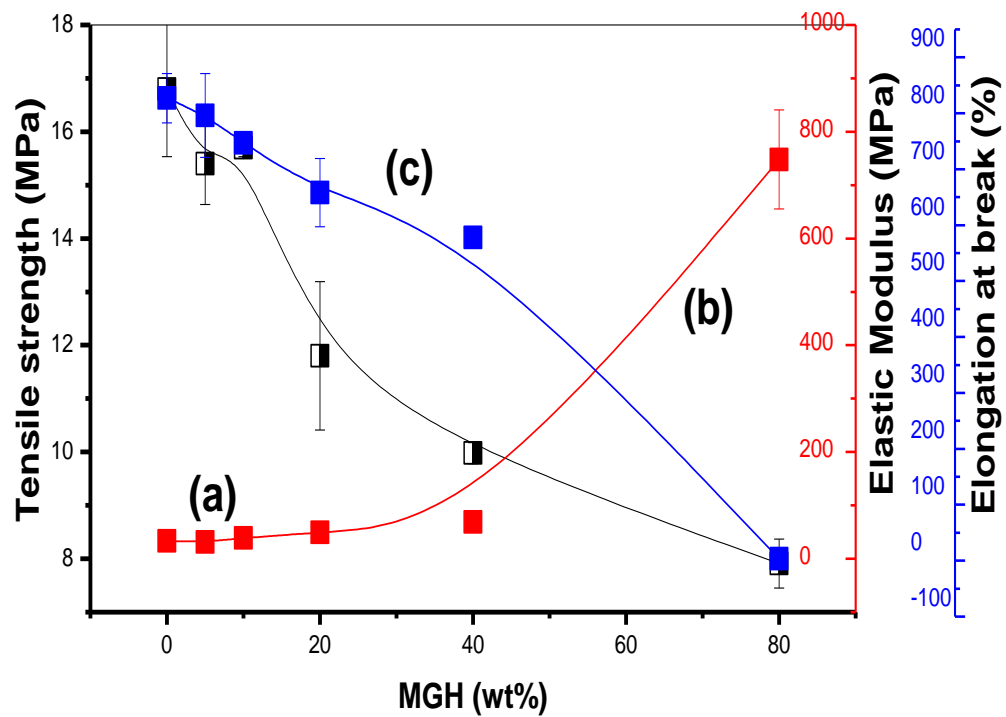


Figure 5.1: Variation in the mechanical properties with increase in MGS weight percentage (a) Tensile strength (b) Elastic modulus (c) Elongation at break

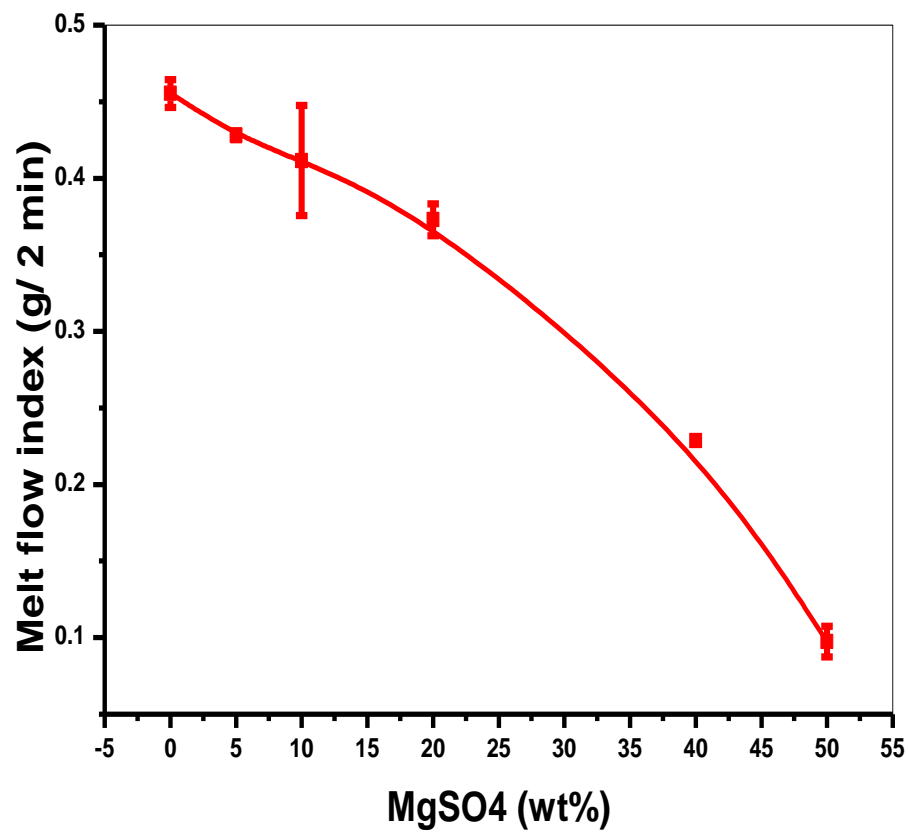


Figure 5.2: Variation in the melt flow index with increase in MGS weight percentage

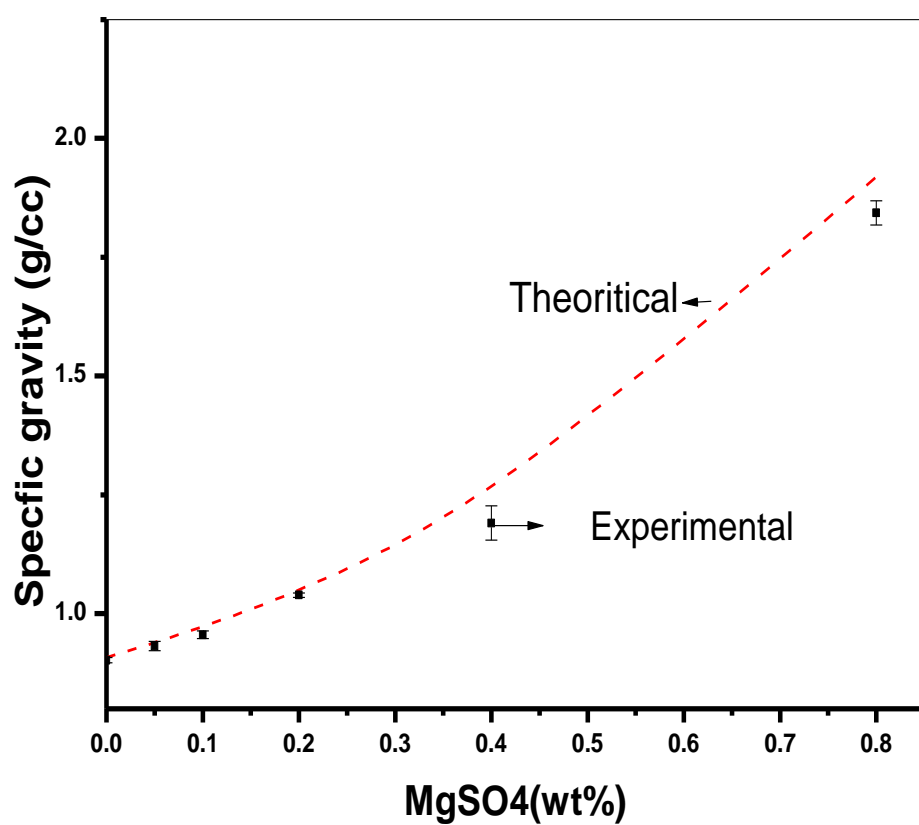


Figure 5.3: Variation in the density with increase in MGS weight percentage (dotted line depicts values calculated using equation 5.1)

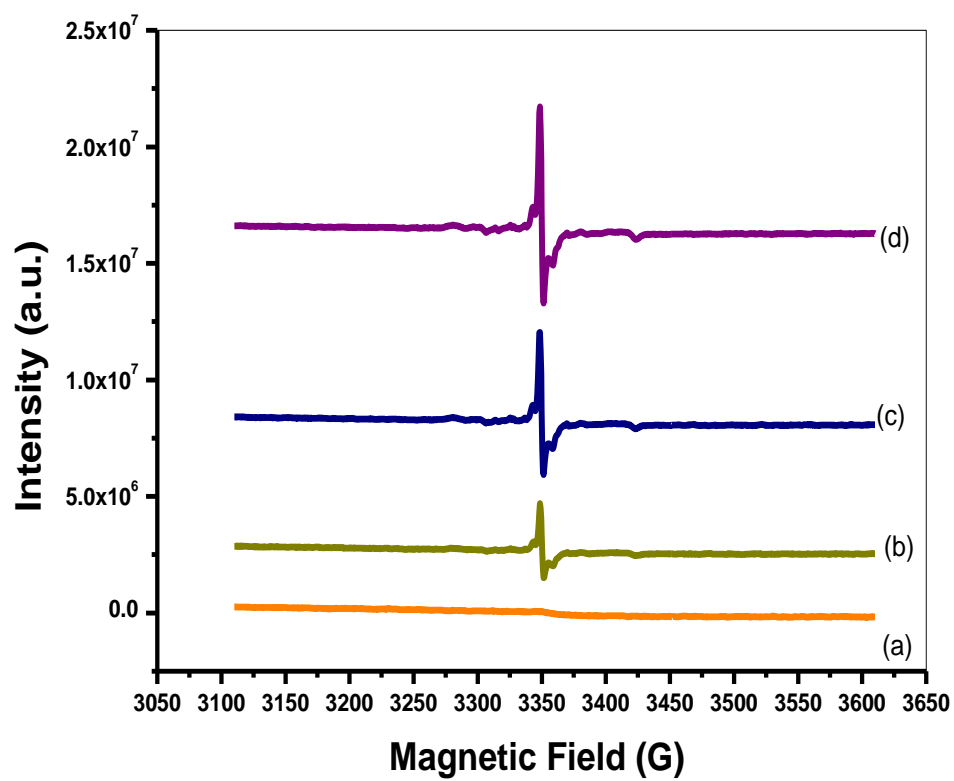
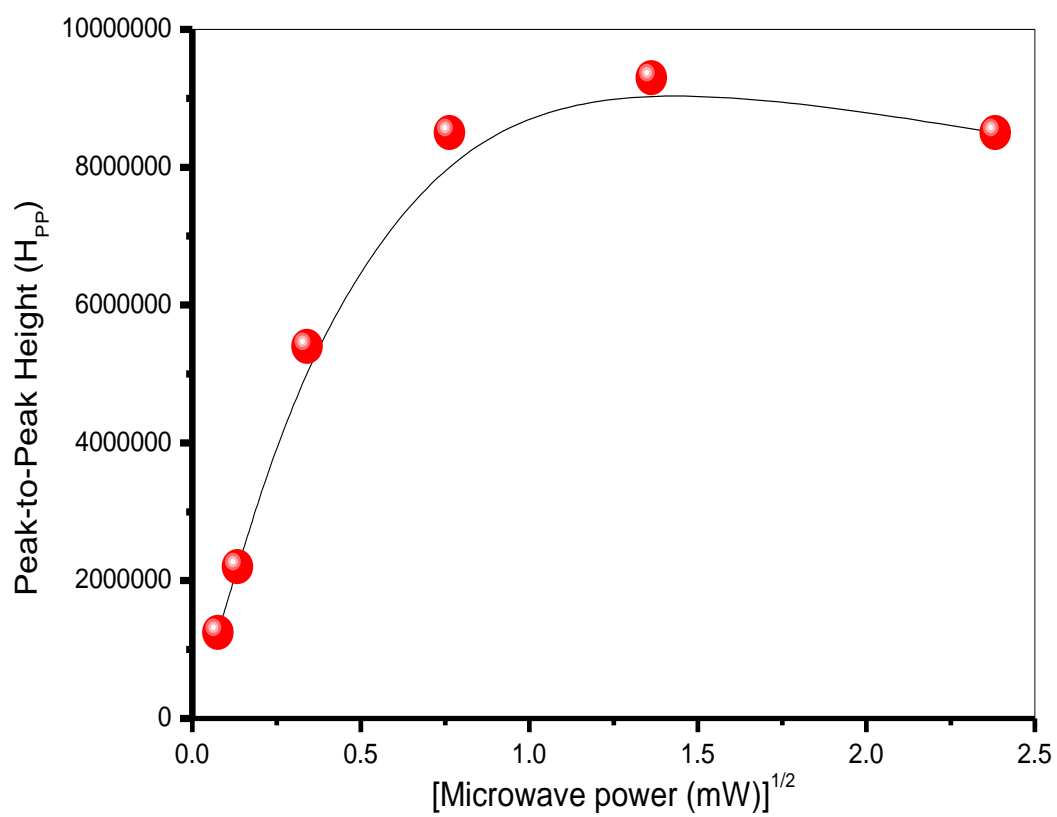


Figure 5.4: ESR spectra of un-irradiated and irradiated composites

(a) 0 kGy (b) 1.1 kGy (c) 2.2 kGy (d) 3.3 kGy



**Figure 5.5: Variation in the H_{PP} with increase in microwave power
(square root)**

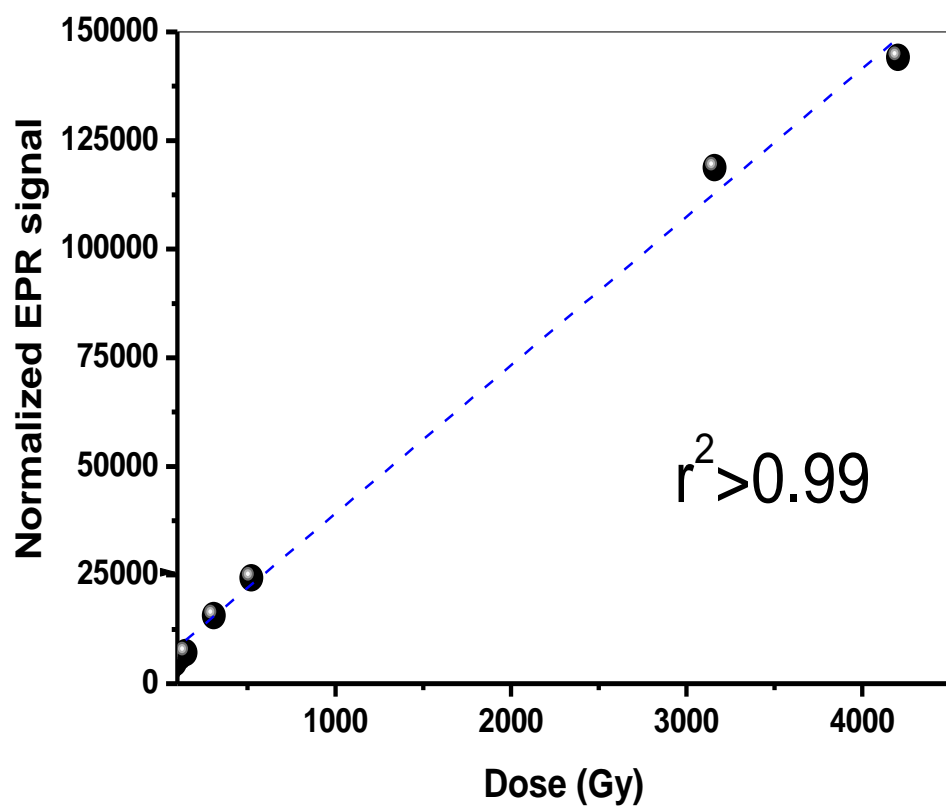


Figure 5.6(a): Variation in the signal height (H_{pp}) increase in radiation dose (100 Gy-4000Gy)

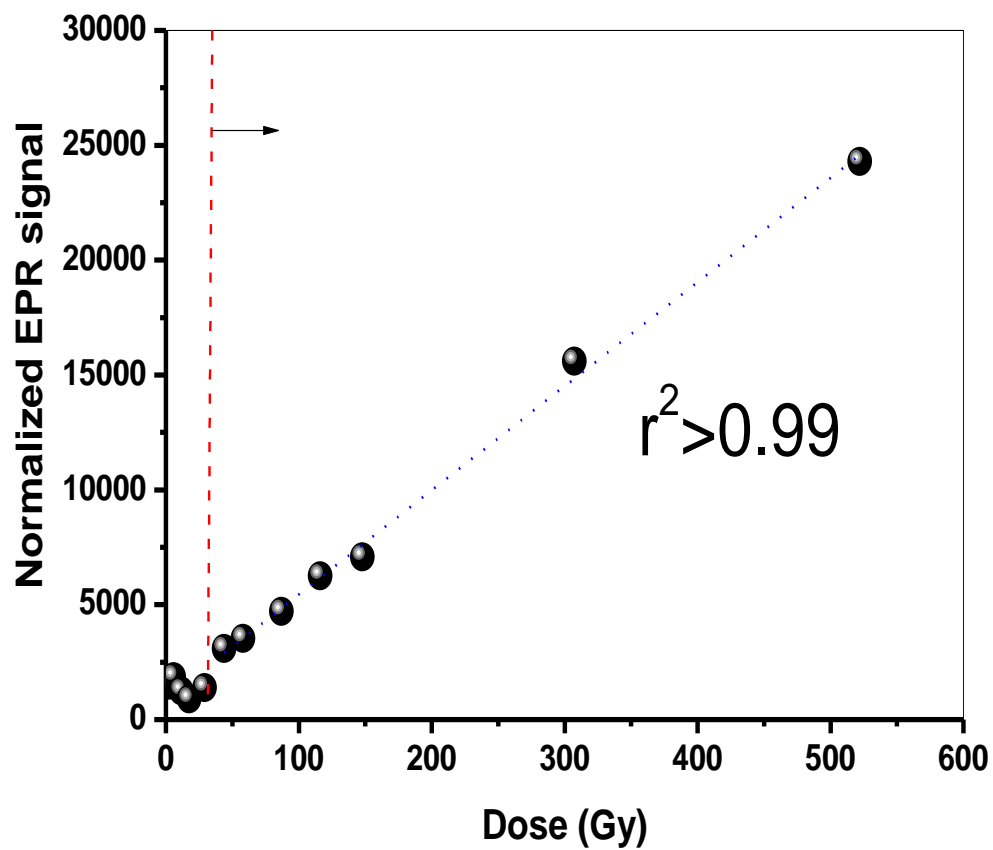


Figure 5.6 (b): Variation in the signal height (Hpp) increase in radiation dose (2Gy-600 Gy)

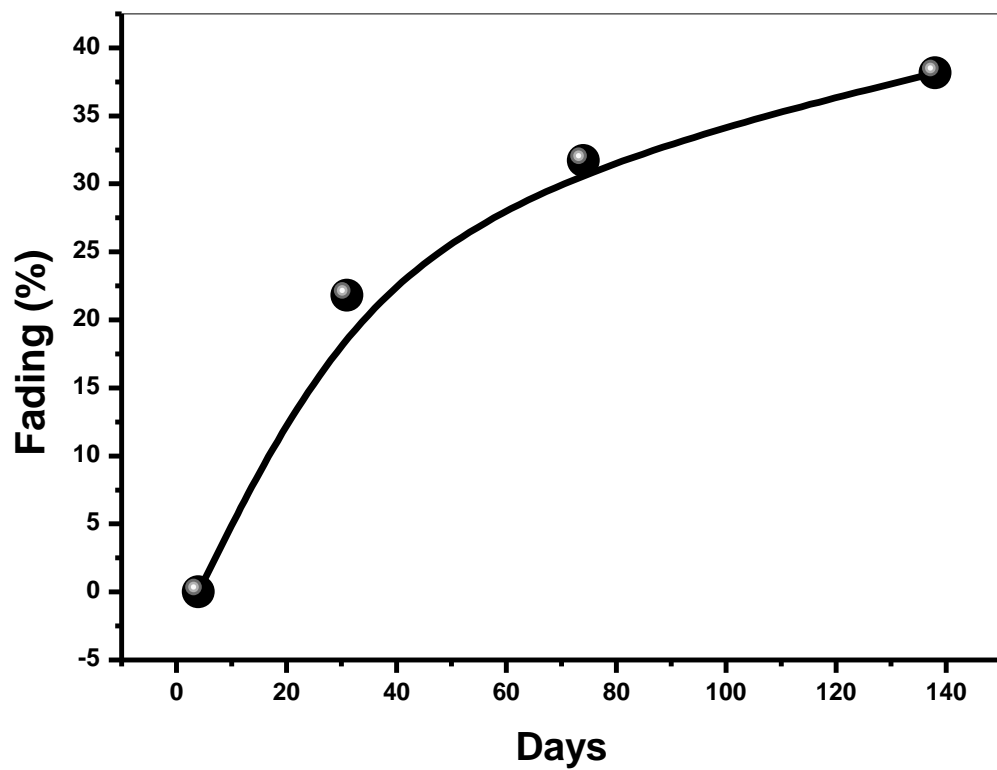


Figure 5.7: Variation of fading of signal with increase in the storage time.
Fading was expressed as the percentage of decrease in the signal intensity of the initial signal.

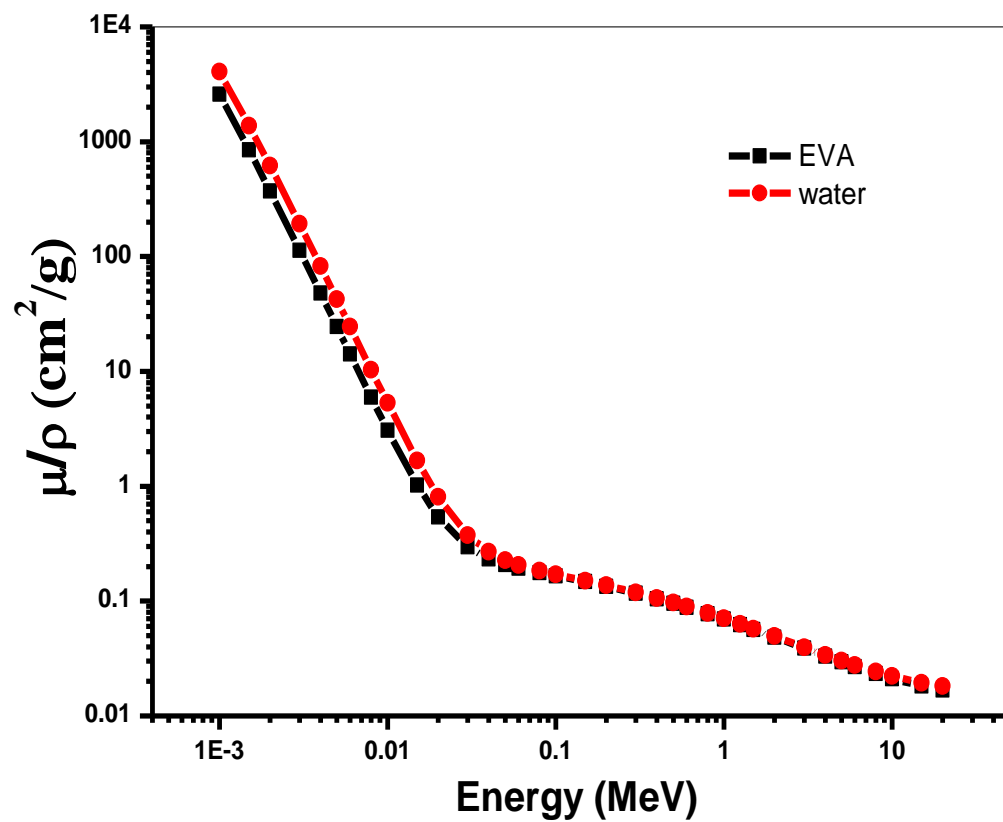


Figure 5.8: Variation in mass energy absorption coefficient (μ_{en}/ρ) of EVA and water with increase in energy

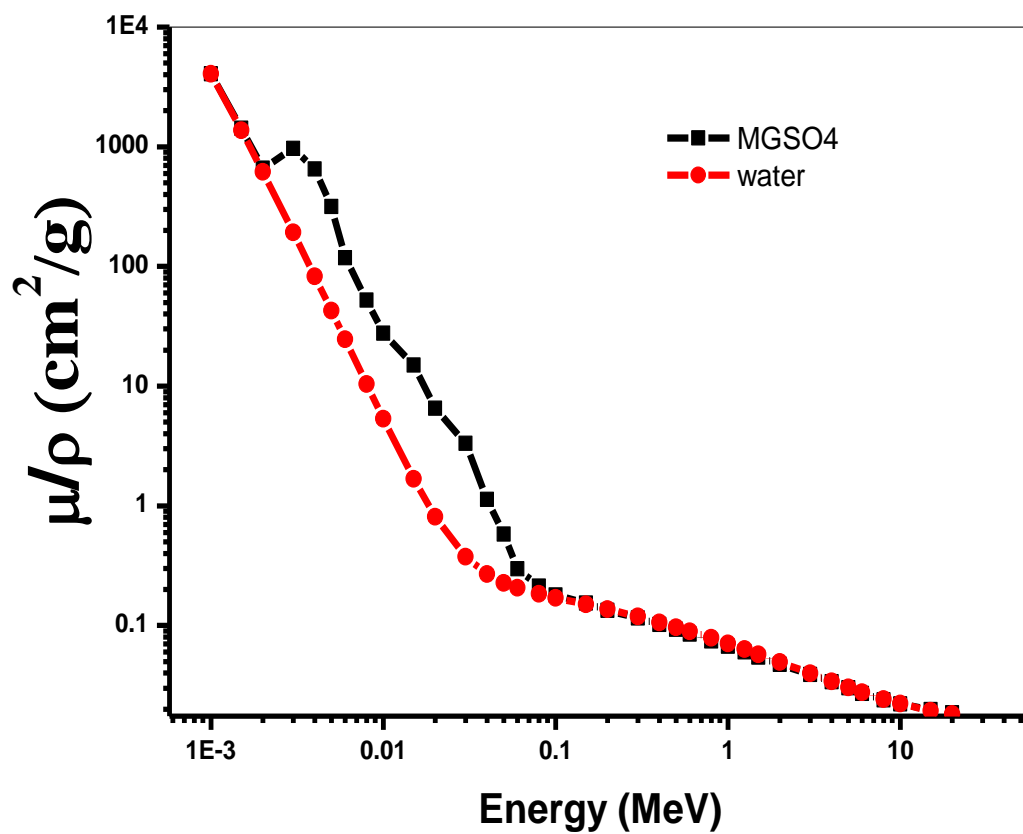


Figure 5.9: Variation in mass energy absorption coefficient (μ_{en}/ρ) of MGS and water with increase in energy

CHAPTER-6

Europium doped Barium sulphate as a perspective dosimeter: Studies based on ESR, TSL and PL techniques

6.1 Introduction

Radiation induced radicals are often very stable in crystalline solid materials. These radicals can be detected and quantified by means of ESR. The signal intensity is proportional to the concentration of paramagnetic species (at least up to kGy doses) and is therefore also proportional to the absorbed dose received due to ionizing radiations. The ESR dosimetry has been applied to a number of fields including radiation therapy, radiation processing, quality assurance, radiation dose reconstruction, the identification of irradiated food and archeological dating (Desrosiers and Schauer, 2001) [165-170]. ESR technique is used as tool for getting crucial information like identification of free, radiation induced-radicals formed and their role in thermally stimulated luminescence processes [171-172]. The main advantage of this method is the linearity of dose response over more than three orders of magnitude which is often present in high radiation field (10 Gy-100 kGy). Polycrystalline samples alanine and methyl alanine has been used for ESR dosimetry for almost two decades, but suffers from low sensitivity for applications in radiation therapy. Lithium formate monohydrate and potassium dithionates are another proposed materials used for ESR dosimetry. It is two to six times more sensitive than alanine and they exhibit simple ESR spectrum consisting of few ESR lines. It may be noted that though there is extensive work carried out on organic systems not many reports exists in the literature on the use inorganic compounds. Important criteria for selecting systems for ESR dosimetry are (a) tissue equivalence with regard to attenuation and scattering of ionizing radiation; (b) stability of radicals with time; (c)

linearity of signal over long range of dose; and (d) large slope for the dose response curve (for very low dose large increase in the intensity of free radicals). The first criteria excludes materials containing heavy elements while the two latter must be verified experimentally.

The aim of the present investigation is to enhance the ESR dosimeter sensitivity, where the first order derivative ESR spectrum of the organic radicals becomes increasingly difficult to evaluate for dosimetry. $\text{MgSO}_4\text{:Eu}$ appears to be an excellent candidate from the spectrometric point of view. On irradiation with ^{60}Co rays the stable radicals SO_4^- and SO_3^- are produced, whose ESR signal intensities increase linearly with dose up to about 10^3 Gy. The spectrum of SO_4^- and SO_3^- is a single line (not ok, change) at $g = 2.0048$ and $g = 2.0036$ respectively and line width of 0.5 mT, which are stable at temperatures up to at least 120°C . Using the conventional peak-to-peak method of dosimeter readout, the MgSO_4 dosimeter is somewhat more sensitive than the traditional alanine dosimeter of the same mass.

Radiotherapy and radiation processing demand proper dosimetry systems. Indeed, dosimetry is a central component of any quality assurance program for an irradiation facility. As a consequence, there is a demand for new dosimetry systems with improved performances. Thermoluminescence dosimetry (TLD) is widely employed for personal and environmental dosimetry but, seldom, for applications at higher doses. Ionizing radiation may induce paramagnetic centers in TSL materials which can be detected by ESR spectroscopy [173-175] This is the case for $\text{CaSO}_4\text{:Dy}$ phosphor, which was proposed as a dosimetric material for ESR dose assessment, mainly for radiation processing applications.

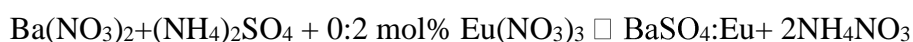
Many industrial applications of radiations, covering a large range of dose from few grays to over $10^6 - 10^7$ Gy, are now well established. A number of conventional high range dosimeters are adequate for radiation processing measurement purposes up to about 10^5Gy (see, for instance, alanine/EPR system) (ASTM, 1995). In the present study, BaSO_4

(undoped and Eu doped) was prepared and evaluated for its TL and ESR dosimetric properties, while photoluminescence studies were done to monitor oxidation state/ emission of Eu dopant ions.

6.2. Experimental

6.2.1. Sample preparation

Polycrystalline BaSO₄:Eu sample was prepared by the chemical co-precipitation method with 0.2 mol % Europium nitrate Eu(NO₃)₃ as the dopant taking in to account the following reaction:



Analytical reagent (AR) grade barium nitrate Ba(NO₃)₂ was dissolved in doubly distilled water. Europium nitrate Eu(NO₃)₃, 0.2 mol% of AR grade was then added to the solution. To control the size of particles to be produced on precipitation, ethanol was then added to the solution with constant stirring. Further, ammonium sulfate was added drop wise to the solution until the precipitation was complete. The mixture was centrifuged each time so that the precipitate settled at the bottom of the tube and a clear liquid was seen at the top. The liquid on the top was then decanted and the precipitate was washed repeatedly in distilled water and dried at 90 °C for two hours. The polycrystalline powder thus obtained was further annealed for 3 hours, at 550 °C, 750 °C, 900 °C under inert argon atmosphere in a quartz boat in a tube furnace and quenched by taking the boat out of the furnace and placing it on a metal block. Similarly un-doped samples were prepared without addition of Eu(NO₃)₃.

6.2.2 Sample Characterization

The phase purity of the prepared sample was investigated by powder X-ray diffraction (XRD) method using a Phillips instrument (PW1071) operating with Cu K_α radiation (λ=1.5405 Å) fitted with graphite crystal monochromator. The scan rate was kept at 0.05 Å^o/sec in the scattering

angle range (2θ) of $10-55^\circ$. Time Resolved Photo Luminescence Spectroscopy (TRPLS) investigations were done on an Edinburgh FLS-900 unit with CD-920 controller. The unit is equipped with a micro second xenon flash lamp as the excitation source and M 300 mono-chromator. TSL studies were carried out on an indigenously built unit. Glow curves were obtained at variable heating rates.

^{60}Co - GC 900 (dose rate - 17 Gy/min) and GC 220 (dose rate - 5.30 Gy/min) were used for gamma irradiation. The dose values were calibrated using a secondary standard system Fricke dosimetry as per the International Atomic Energy Agency's (IAEA) code of practice with a combined uncertainty of 0.45% for air kerma (K_{air}). The synthetic samples were sealed in small polythene capsules, 50 mg each, to be irradiate at room temperature with ^{60}Co gamma radiation to doses ranging from 5 Gy to 1 kGy before recording first derivative EPR spectra. ESR spectra were measured with on X-band spectrometer (EMX series spectrometer; EMM 1843) at room temperature using a standard rectangular cavity (4102 ST) operating at 9.60 GHz with a 100 kHz modulation frequency. The ESR parameters were chosen to provide the maximum signal-to-noise ratio for non-distorted signals. The microwave power and modulation amplitude were 2 mW and 1 G respectively. The response time constant was 40 ms with the field-sweeping rate of 100 G/164 s. The intensity of each sample was measured 10 times as the peak-to-peak height and average values of these measurements of first derivative ESR spectra were plotted. The standard deviation was about 0.5 % from the mean value. Standard samples of DPPH were used to calibrate the g-factor of the ESR signal.

6.3. Results and discussion

6.3.1. XRD results

XRD pattern of BaSO_4 sample prepared by annealing at different temperatures is given in Fig. 6.1. The XRD pattern suggested the formation of single-phase compound as XRD peaks due to impurity phases were found to be absent. The XRD pattern of BaSO_4 belongs to

orthorhombic space group and its lattice parameters were $a = 8.875 \text{ \AA}$, $b = 5.450 \text{ \AA}$, $c = 7.152 \text{ \AA}$ with $\alpha = \beta = \gamma = 90^\circ$ and it four formula units per unit cell. The XRD patterns of un-doped BaSO_4 and $\text{BaSO}_4\text{:Eu}$ samples were in good agreement with the reported data. The (h k l) values of each peak for europium doped BaSO_4 sample are given in the XRD pattern as shown in Fig. 6.1. BaSO_4 mineral consists of divalent cation Ba^{2+} and a divalent tetrahedral molecular anion, SO_4^{2-} . It has an orthorhombic crystal form. In the unit cell, the SO_4^{2-} and Ba^{2+} ions lie on the mirror planes and Ba^{2+} ions link the SO_4^{2-} ions in such a way that each Ba^{2+} ion is coordinated with twelve oxygen. Studies have shown the presence of Ba and SO_4 vacancies in the BaSO_4 lattice and concentration of these vacancies can be very high.

6.3.2. Thermally Stimulated Luminescence (TL) Studies

Figure. 6.2 shows the TL glow curve for gamma irradiated $\text{BaSO}_4\text{:Eu}$ sample at 100 Gy (heating rate of 5 K/s) which can be de-convoluted into two peaks. The irradiated sample was found to have a simple glow curve structure with prominent glow peaks at 450 K and 500 K. The area under the curve was used to determine the TL intensities. Moreover the intensities of the glow peaks were found to increase with increasing dose up to 500 Gy in gamma irradiated $\text{BaSO}_4\text{:Eu}$ sample prepared by co-precipitation method which has also been reported by Annalakshmi et al [176]. As the sample shows a wide linear TSL response even at high doses, it can be employed as a dosimeter for measuring relatively high range doses. This observation suggests that the number of trapping centers or luminescent centers increases with dose. TSL of gamma irradiated $\text{BaSO}_4\text{:Eu}$ samples annealed at 750°C recorded at heating rate of 2 K/sec had shown intense peak around 465 K with shoulder at 443 K.

6.3.3 Photo Luminescence (PL) studies

Photoluminescence spectroscopy is a powerful technique to probe the electronic structure, detection and characterization of defect, recombination mechanism and band gap determination. The PL spectra of europium doped BaSO₄ samples (Fig-6. 3) using excitation wave length of 261 and 298 nm. The emission spectrum consists of an intense peak at 384 nm, which is the characteristic emission of Eu²⁺ ions. Apart from this, two weak peaks at higher wave lengths that is at 590 and 615 were observed. The main emission peak at 384 nm may be ascribed to the transitions between the lowest band of the 4f⁶5d configuration and the ground state ⁸S_{7/2} of the 4f⁷ configuration of Eu²⁺ ion. The strong violet-blue emission exhibited by the Eu²⁺ ions can further be exploited for display applications. It is well known that the wavelength position of the emission band of Eu²⁺ strongly depends on the host lattice. In the crystal structure of BaSO₄, it can be interpreted that each Ba²⁺ atom is coordinated with twelve oxygen atoms. Moreover, Eu²⁺ ions are expected to occupy the Ba²⁺ lattice sites. The weak emissions at 590 and 615 nm wave lengths were attributed to ⁵D₀ → ⁷F_{1, 2} transitions of Eu³⁺. It was seen that the intensity of Eu³⁺ emission decreased in samples annealed at 750°C with concomitant increase in intensity at 384 nm suggesting more of Eu²⁺ incorporation at Ba²⁺ site. On further annealing, samples further at 900°C, intensity of Eu²⁺ decreased marginally. But the Eu²⁺/Eu³⁺ luminescence intensity ratio was higher in the samples annealed in argon atmosphere at higher temperatures. The gamma irradiated samples did not show significant changes in PL intensity of Eu²⁺. No change in the PL spectra was seen on gamma ray irradiation indicating that there is no Eu²⁺ → Eu³⁺ valence conversion occurring during gamma irradiation.

6.3.4 Electron Spin Resonance (ESR) studies:

ESR spectra of gamma irradiated BaSO₄ samples were recorded at room temperature. The ESR spectra for un-doped BaSO₄ and BaSO₄:Eu samples

were identical in their features. The ESR spectra appear to be arising from at least two free radicals. This fact was further supported by microwave power variation behavior and thermal annealing studies. It was seen that one of the free radical showed a line-shape characteristic of a species having nearly axially symmetric g-tensor. The observed principal g values are $g_{\parallel}=2.0406$ and $g_{\perp}=2.0084$ which were attributed to SO_4^- radical. The second free radical exhibiting an isotropic g factor, $g_{\text{iso}}=2.0028$ was identified as SO_3^- on the basis of reported g values.

In present investigations, we have annealed un-doped BaSO_4 and $\text{BaSO}_4\text{:Eu}$ at higher temperatures (550 °C, 750 °C, 800 °C and 900 °C). These samples (100 mg each) were irradiated to 500 Gy and their spectra were recorded at room temperature. The plots of ESR signal intensities for SO_4^- and SO_3^- radicals Vs annealing temperature is depicted in figure 6.5(A) and 6.5(B). From these plots it was concluded that

- (1) Intensity of SO_3^- radical increased drastically for un-doped BaSO_4 and $\text{BaSO}_4\text{:Eu}$ samples annealed up to 750 °C, on increasing the annealing temperature further there was gradual reduction in the intensity of SO_3^- radical was observed and also the rate of increase in the intensity of SO_3^- radical is more for $\text{BaSO}_4\text{:Eu}$ sample
- (2) increase in the intensity of SO_4^- radical was observed as annealing temperature was increased from 550 °C to 900 °C (increase is nearly 10 times for europium doped sample and 4 times for un-doped sample). Further, in both samples, SO_3^- signal was relatively sharp and therefore, un-doped BaSO_4 and $\text{BaSO}_4\text{:Eu}$ samples were annealed at 750 °C were investigated further for the dosimetric studies.

The appropriate setting of microwave power is necessary for the ESR measurement so as to obtained better signal to noise ratio and also less distorted signals for these radicals. Usually microwave power is kept below the saturation level of the radicals used for dosimetric measurements. ESR spectra were recorded at different microwave power

levels to confirm formation of more than one radical and also their saturation behavior. Figure. 6.6(A) and Figure. 6.6(B) depict the microwave power dependence of signal intensities of SO_3^- and SO_4^- radicals in un-doped BaSO_4 and $\text{BaSO}_4\text{:Eu}$ samples. The signal intensities of SO_3^- and SO_4^- radicals increases as a function of power upto 4.0 mW, and gets saturates with further increases in microwave power. Thus the optimum microwave power is 4.0 mW. It may be noted that increase in ESR signal intensity of SO_3^- radical is much drastic in case of $\text{BaSO}_4\text{:Eu}$ sample compared to un-doped BaSO_4 sample.

Fig. 6.4 presents a comparison between the dose response of irradiated un-doped BaSO_4 and $\text{BaSO}_4\text{:Eu}$ to different gamma doses. The changes in the peak-to-peak height of SO_3^- and SO_4^- radical were found to be linear in the range 2 – 1000 Gy. Beyond 1 KGy of gamma radiation, both samples saturate in ESR signal intensity [in contrast to alanine, which has dose – signal linearity in response extended to 100 KGy]. It is found that the slope of the dose response curve is almost same for both samples viz., un-doped BaSO_4 and $\text{BaSO}_4\text{:Eu}$, (Figure 6.7).

The dose – signal behaviour suggest that the sensitivity is almost same for both these samples. The linearity of the ESR response of this sample as a function of dose up to 1 KGy suggests that it will be a good material for low dose measurements. Particularly, if one considers the possible areas of use of this material, it will be very suitable for detecting small exposures of radiation associated with radiation therapy applications.

6.4. Summary

BaSO_4 and $\text{BaSO}_4\text{:Eu}$, samples in powder form, has been found to be responsive for ESR dosimetry. In BaSO_4 samples for SO_4^- signal ($g = 2.0014$) the linearity in dose – signal response is observed in the 10 – 1000 Gy dose range, while in case of $\text{BaSO}_4\text{:Eu}$ samples, the linearity in dose – signal response is observed for SO_3^- signal ($g = 2.003$) in the 10 – 1000 Gy dose range. It could find usage as dosimetric material in the intermediate dose range applications, as well BaSO_4 samples in pellet form could lead

to dose response at lower threshold dose. The dose response of SO_3^- radical ($g = 2.003$) was found to be poor for microwave power above 3.9 mW.

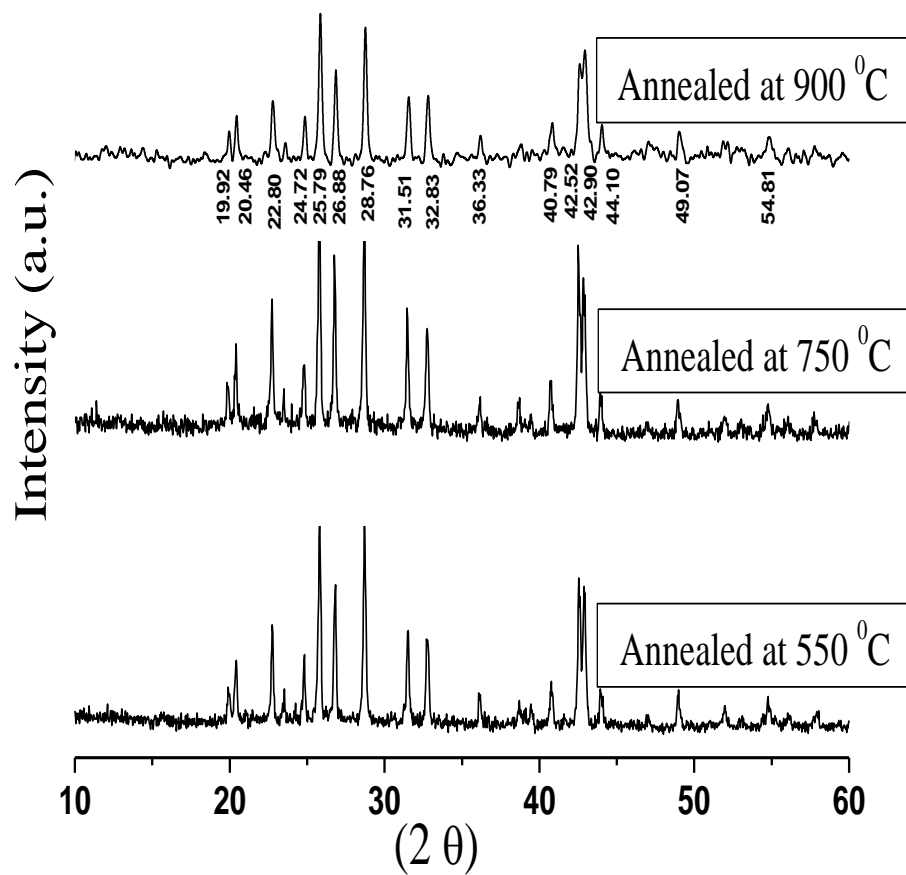


Fig. 6.1: XRD pattern of polycrystalline sample of $\text{BaSO}_4\text{:Eu}$ annealed at different temperatures

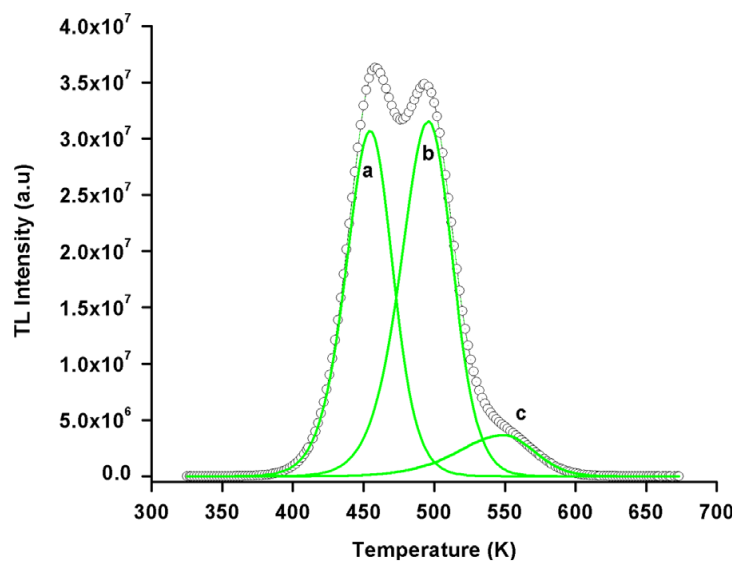


Figure 6. 2: TL glow curve for gamma irradiated BaSO₄: Eu

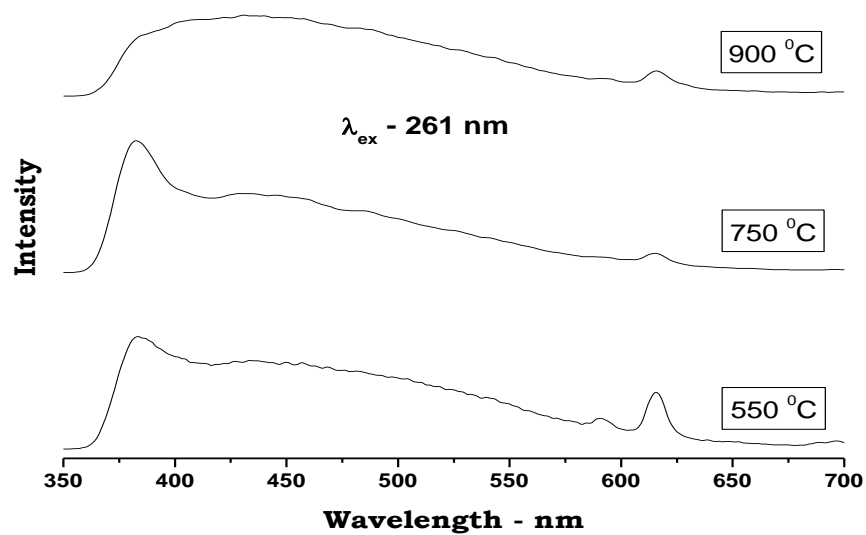


Figure 6.3-Photo Luminescence of BaSO₄-Eu at different annealing temperatures

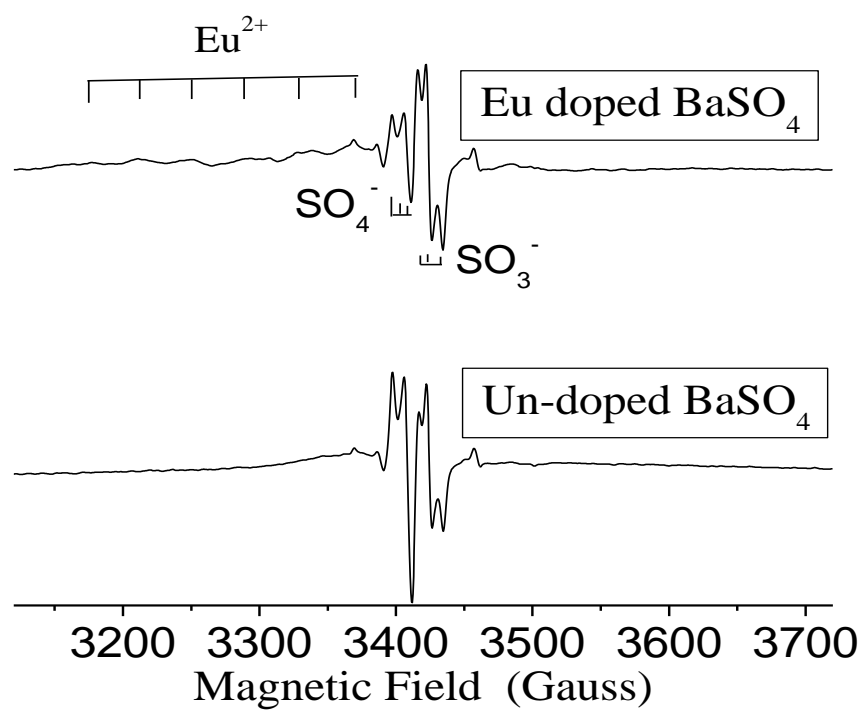


Figure 6. 4-ESR Spectra of Un irradiated Un doped and Europium doped BaSO₄

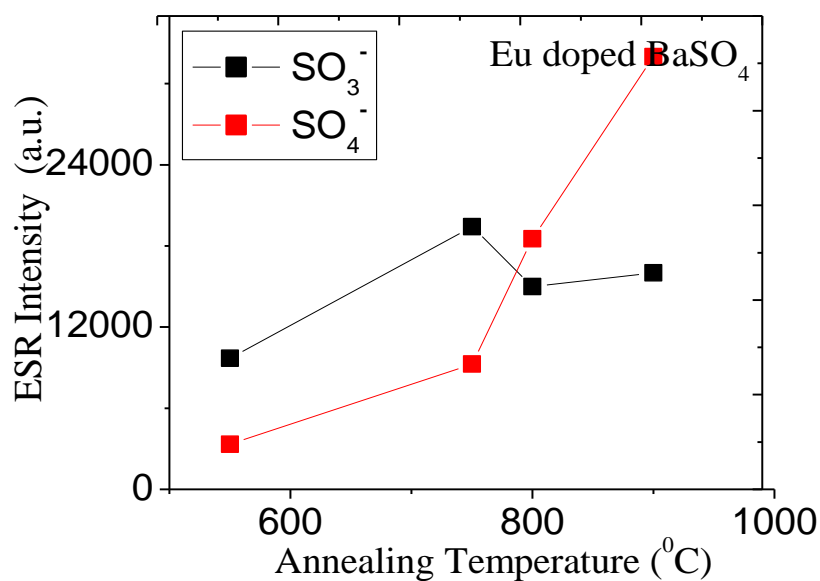


Figure 6.5(A): Changes in radical intensity of BaSO₄:Eu with temperature

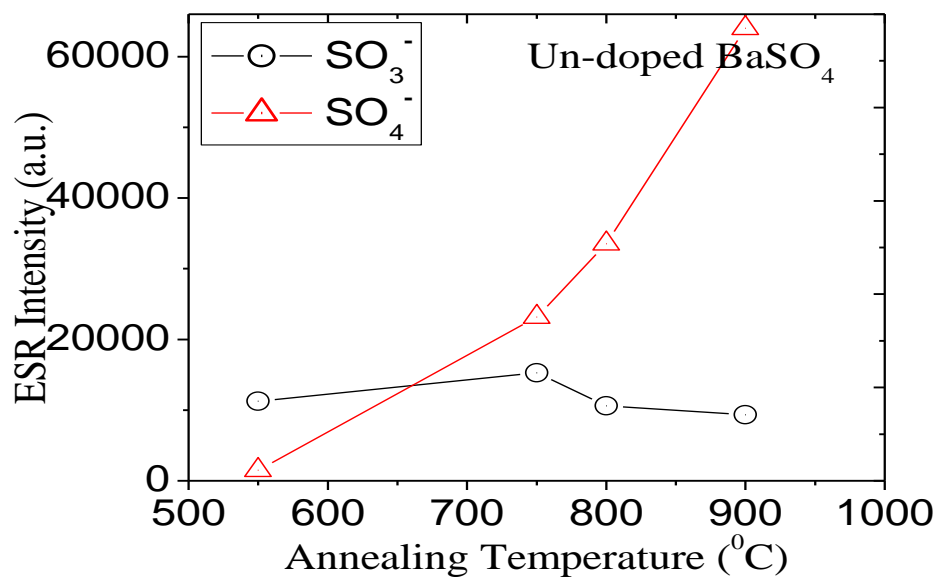


Figure.6.5 (B): Changes in radical intensity of un-doped BaSO₄ with temperature

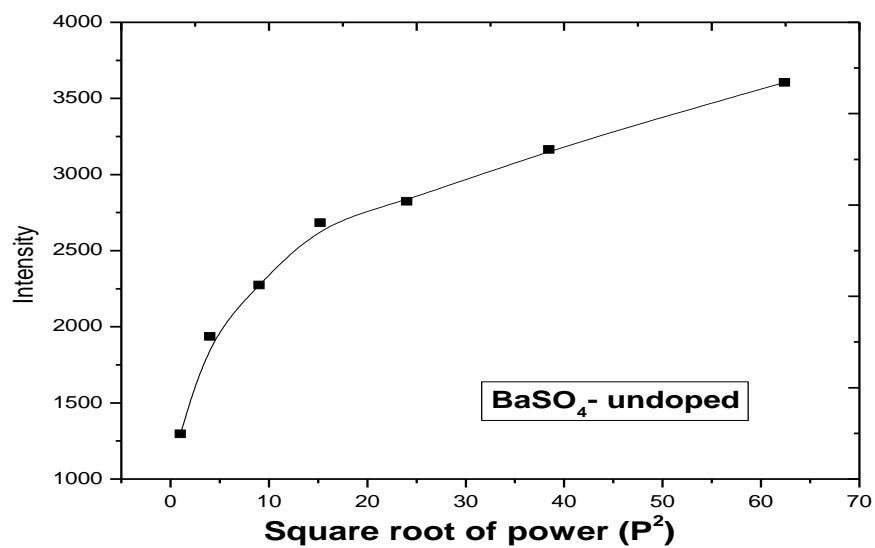


Fig.6.6 (A) Power dependence - Un-doped BaSO_4

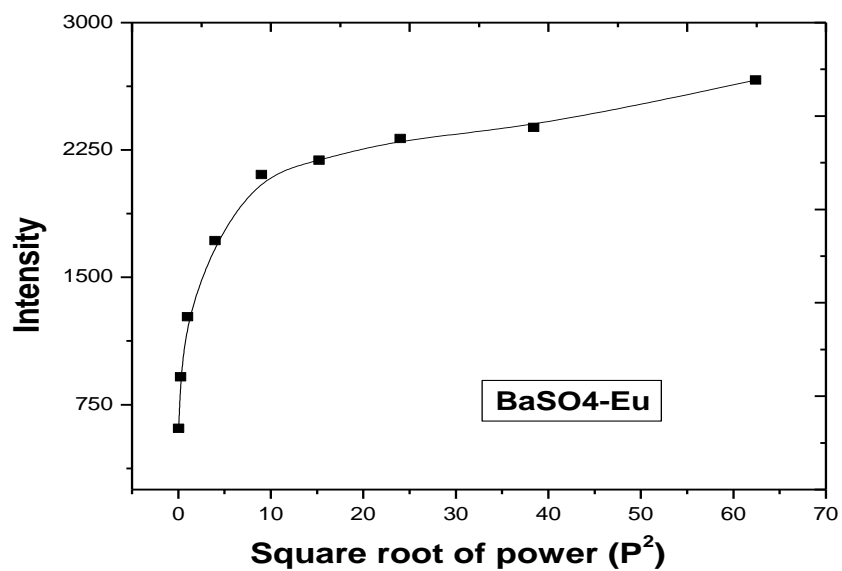


Figure 6.6 (B) Power dependence – Eu doped BaSO_4

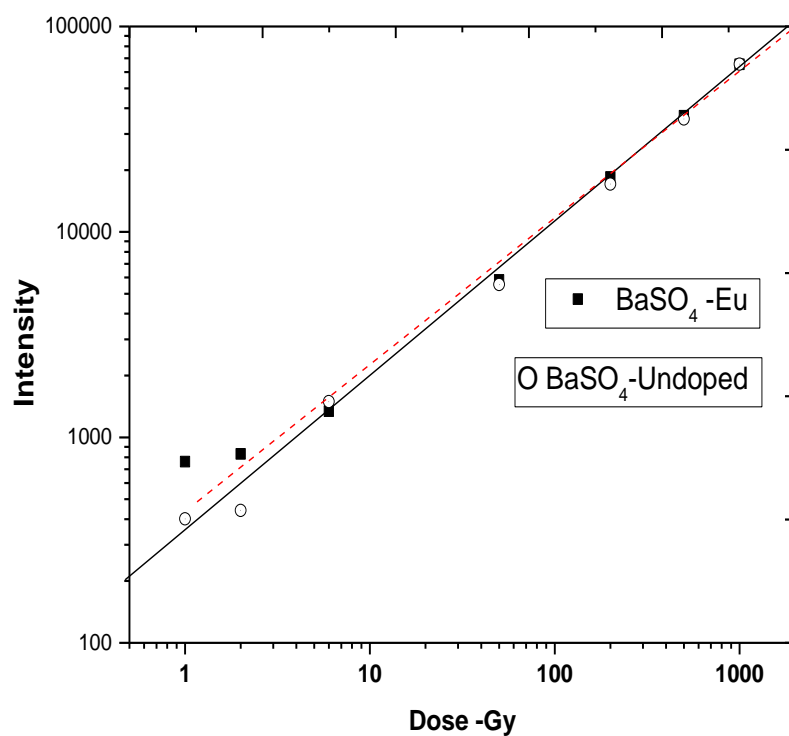


Figure 6.7 Comparison between the dose responses of irradiated un-doped BaSO₄ and BaSO₄: Eu to different gamma doses

Conclusions and future scope

In summary, this thesis deals mainly with the synthesis and characterization of polymer composite materials of organic and inorganic compounds, evaluation of their physical properties and their suitability for application as radiation shield/ in radiation dosimetry using ESR technique. In addition, a couple of inorganic materials such as BaSO₄ and glass have also been studied for their ESR dosimetric applications. The advantages of ESR dosimetry for high gamma dose evaluation has been highlighted.

The introductory chapter gives a detailed account on radiation interaction with matter through photoelectric and Compton interactions of electrons and pair production, quantification of radiation dose in terms of radiation induced defects/effects in matter, different essentials of dosimetric systems. Moreover, the techniques currently used for dosimetric evaluation such as calorimetry, Fricke dosimetry, FBX dosimetry, TL dosimetry and ESR dosimetry are described. The principle of ESR technique from fundamentals has been dealt with in detail. Further, an exhaustive literature survey on work related to ESR dosimetry during the past two decades and the motivation of the present work on preparation of cost effective polymer based ESR dosimeters have been provided.

Chapter 2 deals basically with the techniques used for characterization of polymer composite materials and evaluation of their mechanical and thermal properties, quantification of radiation induced radicals and estimation of irradiated material. Mechanical properties, X-ray studies, thermal properties and cross linking density measurements provide important information about the effect of high energy radiation on the basis of induced effects.

In chapter 3, the effective use of gamma irradiation for cross linking the composites containing large amounts of high Z fillers, namely poly-di-methyl-siloxane (PDMS) / bismuth oxide (Bi_2O_3) and PDMS- BaSO_4 composites, have been discussed. The potential of such polymer composites as flexible radiation shields for ^{241}Am γ radiation has been highlighted. The specific gravity of the PDMS- Bi_2O_3 composites followed the rule of mixture closely up to 50 wt % loading; slight deviation at higher loading was assigned to agglomeration within the matrix, Bi_2O_3 reinforcing the PDMS matrix, was well corroborated with the mechanical properties. Elongation Break (EB) decreased with radiation dose as well as with filler loading, while Young's modulus increased significantly and was found to deviate from the Nielsen's micromechanical model. Interestingly, the deviation was positive suggesting formation of Bi_2O_3 network within PDMS. Attenuation of gamma ^{241}Am at 70 wt% filler loading was observed to be 90%. Thermal stability of composites significantly improved with the addition of filler. Radiation cross-linked

matrices were found to be excellent choices for developing lead free flexible shielding. It was established that tailoring of vinyl content can ascertain high radiopacity even at higher loading of BaSO₄. Such effects translated in better gray values than those obtained from the aluminum sheets of comparable thickness, while retaining markedly high elongation at break, low mechanical hysteresis and complete flexibility. Ethylene vinyl acetate (EVA)/ BaSO₄ composites displayed a complex interplay of the morphology, the crystallinity and the copolymer architecture. VA content of 25% displayed unique attribute in most of the rheological, mechanical and dynamic thermo mechanical properties. The power law was followed by all composites in the structural breakdown region and the filler-filler structural breakdowns was found to be a key factor in non-linear strain behavior, which was dependent on VA content. Time-temperature super-imposition study showed a difference in fractional free volume with a change in vinyl acetate content. These results will be extremely useful in designing radiopaque polymer composites for medical and other applications with predetermined physico-mechanical and radiation opacity behavior.

In Chapter 4, radiation effects on a dye doped polymer composite, poly(chloroprene) (PC), a highly flexible polymer, doped with methyl red. This was prepared by shear compounding method. The composite showed dose dependent decoloration upto 30 kGy. Optical micrographs suggested good dispersion of dye in the polymer matrix. There was no significant

effect of dose rate, temperature. The precision of PC/MR film dosimeters was very good and the percentage fluctuation was less than 5% at all doses studied. Such systems have potential applications in routine high range (kGy) radiation dosimetry.

In Chapter 5, the evaluation of mechanical/physical properties of EVA/MGS (magnesium sulphate) composites prepared via melt compounding and their application in radiation dosimetry have been described. Mechanical properties of the composites were greatly influenced by the addition of MGS in EVA matrix, indicating improvement in the elastic modulus and decrease in elongation at break. Composites greater than 50 wt % of MGS did not show flow behavior during melt flow measurement and the specific gravity of the composites increased with the increase in MGS content. The dosimeter displayed linear response between 20Gy and 4kGy. The response was reproducible with around 20% fading in 32 days period. The composite was water equivalent for the energy greater than 100 keV. These results underscores suitability of melt compounded EVA/MGS composites for radiation processing applications.

In Chapter 6, the application of two inorganic materials, BaSO_4 and a commercial glass powder for ESR dosimetry have been described. BaSO_4 and $\text{BaSO}_4\text{:Eu}$, samples in powder form, were found to be responsive for ESR dosimetry. The sensitivity of both samples were found to be nearly the same. In irradiated BaSO_4 samples, for SO_4^- signal ($g = 2.0014$) the

linearity in dose – signal response is observed in the 10 – 1000 Gy dose range, while in case of BaSO₄:Eu samples, the linearity in dose – signal response is observed for SO₃⁻ signal (g = 2.003) in the 10 – 1000 Gy dose range. It could find use as dosimetric material in the intermediate dose range applications; BaSO₄ samples in pellet form could lead to dose response at lower threshold dose.

Scope for future studies

1. Further understanding of morphology-attenuation correlation and attenuation coefficients of PDMS/Bi₂O₃ for gamma rays of different energies are needed to use such composites in advanced applications such as mixed radiation field (gamma + neutrons) dosimetry and radiation shielding.
2. Designing more radiopaque polymer composites for medical and other applications with predetermined physico-mechanical and radiation opacity behavior.
3. The glass powder samples will be further investigated by ESR for identification of the radiation induced radicals and application as possible accidental dosimeters.

Reference:

1. Knoll, Glenn F., Radiation detection and measurement, Wiley & Sons, 2000; New York.
2. Price, William, J. Nuclear radiation detection, Mc Graw Hill, 1964; New York.
3. Gupta B.L. and Bhat R.M., Calibration of high – dose radiation facilities, 1986; BARC – 1303.
4. Nayak A.R., Interaction of radiation with matter, IAEA regional basic professional course on radiation protection, 1998.
5. Attix F.H., Roesch W.C. Radiation dosimetry, Vol.II, Academic Press, 1968; New York.
6. Measurement Uncertainty A Practical Guide for Secondary Standards Dosimetry Laboratories, 2008, TECDOC-1585, IAEA, VIENNA
7. Sudheer T.S. M.Sc., Thesis (2001), – University of Mumbai.
8. Ralph Livingston, Free radical produced by radiation, Radiation Research (1959),
9. Ralph Mathews, Aqueous chemical dosimetryInt., J. Appl. Rad.Iso. , 1982, 33.
10. Moe. H.J., Lausk S.R., Schumacher M.C. and Hunt H.M. Radiation safety technician course, Argonne National Laboratory, 1972, U.S.A.
11. Marfunin A.S. Spectroscopy, Luminescence and Radiation Centers in minerals, Berlin, Springer – Verlag, 1979, New York.

12. Nambi, K.S.V. Bapat V.N.J.Phys. 1980, C-13, 1555.
13. Nambi, K.S.V. Thermo luminescence – its understanding and applications, Inst. Energy Atom, (Sao Paulo) Rep.1977, IAEA – 541.
14. Seshagiri T.K., Natarajan V., Dalvi A.G.I. and Sastry M.D. Pramana, J. Phys.1989, 33.
15. Bradshaw W.W., Cadena D.G., Crawford G.W. and Spetzler H.A.W., The use of alanine as a solid dosimeter Radiat. Res.1962, 17.
16. Chu.S., Wieser A., Feist H. and Regulla D.F. ESR / Alanine dosimetry of high-energy electrons in radiotherapy, Appl. Rad. Isot. (1989), 40.
17. Hansen J.W., Olsen K.J. and Wille M. The alanine radiation detector for high and low LET dosimetry, Radiat. Prot. Dosim. 1977, 19(1)
18. Kojima T., Morishita N., Itoh H. and Biramontri S., Irradiation and ESR analysis of temperature dependence of the Gamma-ray response of Alanine-Polystyrene dosimeters, Appl. Radiat. Isot.1996, 47
19. Martin M. Dorio, Jack H., Freed, Multiple electron spin Resonance spectroscopy, 1979.
20. Gamal M. Hassan*, Motoji Ikeya, Shunji Takaki Radiation-induced defects in magnesium lactate as ESR dosimeter Radiation

- measurement, 1999, 30, 189-196.
21. Regulla D.F., and Deffner U., Dosimetry by ESR spectroscopy of alanine, Int.J. Appl. Radiat. Isot. (1982, 33.
 22. Sastry M.D., Natarajan V., and Bhatt B.C. EPR technique for radiation dosimetry – Emerging trend for laboratory and accidental dosimetry, J.Med. Phys. 1996; 21, 4.
 23. Wieser A., Siegele R., and Regulla D.F. Influence of the temperature on the Free-radical response of Alanine, Appl.Rad. Isot.1998; 40.
 24. Zagorskil Z.P., Dosimetric application of –Alanine, J.Radioanal. Nucle. ChemLett. 1994, 187, (1).
 25. Miller, Calculation of energy dependence of some commonly used dosimeters. High dose dosimetry for radiation processing, Proc. Int. Symp (1984).
 26. Venkataramani R., Mehta S.K., Iyer M.R., Natarajan V., and Sastry M.D. Dose determination by ESR technique using cotton fabric, J.Radioanal. Nucl.Chem. Lett. 1993, 175, (1).
 27. Romanyukha A A, M F Desrosiers, D MF Ragullla Current issue of EPR dosereconstruction in tooth enamel App. Rad. and Isotope. 2000, 52, 5, 1265-1273.
 28. M. Ikeya, J Miyagima and S Okajima ESR dosimetry for atomic bomb survivors using shell buttons and tooth enamel, , Japanese Journal Of App. Phy. 1984; 23, 9, L.697-L.699.

29. S Cook and T Obje, An ESR study on Biological dosimeter: humain hair Radiation measurements, 2011, 46, 5, 465-472
30. Symons,M.,H. Chandra, and J. Wyatt, EPR spectra of irradiated finger nails: a possible measure of accidental exposure. Radiation protection dosimetry, 1995, 58(1): p. 11-15.
31. Nakajima T., ESR of sugar as a personal monitor for radiation emergencies, Appl. Rad. Isot., 1995, 46.
32. Z.M.Da Costa,W M Pontuschka, L l CamposStudy of the ESR signal of gamma irradiated hydroxyapatite for dose assessment Nuclear Instruments and Methods in Physics Research; 2004, Volume 218, Pages 283-288.
33. A Krivokapic, A saderud, S G Aalberg, E O Hole, E Sagsstun, Lithium Formate for EPR dosimeter(2) : Secondary radicals in X-Irradiated Crystals, Rad. Res. 2015, 183(6), 675-83.
34. Romanyukha A A; et al. EPR dosimetry in chemical treated fingernails. Radiation measurements, 2007, 42(6): 1110-1113.
35. Ahmed M. Maghraby, A. Mansour, A. A. Abdel-Fattah Taurine-EVA copolymer-paraffin rods dosimeters for EPR high-doseNukleonika 2014, 59(1):9–13.
36. Kraus, G. Journal of Applied Polymer Science, 1963, 7(3): p. 861-871.
37. Cain, J., Q. Yu, X. Zhang, J. Lin, and L. Jiang. Journal of Polymer Science, Part B: Polymer Physics, 2005, 43(20): p. 2885-2897

38. El-Sabbagh, S.H. *Polymer Testing*, 2003. 22(1): p. 93-100.
39. S Murali (PhD) Thesis, 2002, University of Mumbai.
40. Gordy W, *Theory and applications of electron spin resonance*, John Wiley & Sons, 1980; New York.
41. Charles Poole *Electron spin resonance*, John Wiley & Sons, 1962; New York.
42. Abragam A and Bleaaney B; *Electron Para-Magnetic Resonance of Transition Ions*, 1970. Oxford, England.
43. Kulshreshtha, A.K., B.P. Singh, and Y.N. Sharma. *European Polymer Journal*, 1988, 24(1): p. 33-35.
44. Kulshreshtha, A.K., B.P. Singh, and Y.N. Sharma. *European Polymer Journal*, (1988), 24(1): 29-31.
45. Abdel-Rehim, F., Said, F.I.A., Abdel Azim, A.A., El-Dessouky, M.M., Youssef, N., Use of bromothymol blue solutions as a spectrophotometric dosimeter. *Radiat. Phys. Chem.* 1987, 30, 209.
46. Barakat, M.F., El-Salamawy, K., El-Banna, M., Abdel-Hamid, M., Abdel-Rehim Taha, A., Radiation effects on some dyes in non-aqueous solvents and in some polymeric films. *Radiat. Phys. Chem.* 2001, 61, 129–136
47. El-Banna, M., Study on some radiolytic effects in non-aqueous samples of organic dyes. Ph.D. Thesis, 1998, .Ain Shams University, Physical Chemistry Department, Egypt.
48. Chang, P., *Polymer implant materials with improved X-ray opacity*

- and biocompatibility. *Biomaterials* 1981, 2 (3), 151-5.
49. Aviv, H.; Bartling, S.; Kiesling, F.; Margel, S., Radiopaque iodinated copolymeric nanoparticles for X-ray imaging applications. *Biomaterials* 2009, 30 (29), 5610-5616.
 50. de Vries, A.; Custers, E.; Lub, J.; van den Bosch, S.; Nicolay, K.; Grüll, H., Block-copolymer-stabilized iodinated emulsions for use as CT contrast agents. *Biomaterials* 2010, 31 (25), 6537-6544.
 51. Kiran, S.; James, N. R.; Joseph, R.; Jayakrishnan, A., Synthesis and characterization of iodinated polyurethane with inherent radiopacity. *Biomaterials* 2009, 30 (29), 5552-5559.
 52. Xiao, Q.; Bu, W.; Ren, Q.; Zhang, S.; Xing, H.; Chen, F.; Li, M.; Zheng, X.; Hua, Y.; Zhou, L.; Peng, W.; Qu, H.; Wang, Z.; Zhao, K.; Shi, J., Radiopaque fluorescence-transparent TaOx decorated upconversion nanophosphors for in vivo CT/MR/UCL trimodal imaging. *Biomaterials* 2012, 33 (30), 7530-7539.
 53. Bartosch, M.; Peters, H.; Spriestersbach, H.; O H-Ici, D.; Berger, F.; Schmitt, B., A Universal Delivery System for Percutaneous Heart Valve Implantation. *Annals of Biomedical Engineering* 2016, 1-12.
 54. Fischer, S. C. L.; Levy, O.; Kroner, E.; Hensel, R.; Karp, J. M.; Arzt, E., Bioinspired polydimethylsiloxane-based composites with high shear resistance against wet tissue. *Journal of the Mechanical Behavior of Biomedical Materials* 2016, 61, 87-95.
 55. Li, K.; Huang, J.; Gao, H.; Zhong, Y.; Cao, X.; Chen, Y.; Zhang, L.;

- Cai, J., Reinforced Mechanical Properties and Tunable Biodegradability in Nanoporous Cellulose Gels: Poly(l-lactide-co-caprolactone) Nanocomposites. *Biomacromolecules* 2016, 17 (4), 1506-1515.
56. Wang, Y.; Gale, D. C., Bioabsorbable stent with radiopaque layer and method of fabrication. Google Patents: 2015.
57. Felix T, Pinto OP, Peres A, Costa JM, Sayer C, Morgan AB, et al. Comparison of bismuth trioxide and antimony trioxide as synergists with decabromodiphenyl ether in flame retardancy of high-impact polystyrene. *Journal of Fire Sciences*. 2012;30:566-74.
58. Zhang J, Feng S, Ma Q. Kinetics of the thermal degradation and thermal stability of conductive silicone rubber filled with conductive carbon black. *Journal of Applied Polymer Science*. 2003;89:1548-54.
59. Noor Azman NZ, Siddiqui SA, Low IM. Synthesis and characterization of epoxy composites filled with Pb, Bi or W compound for shielding of diagnostic x-rays. *Applied Physics A: Materials Science and Processing*. 2013;110:137-44.
60. Nambiar S, Osei EK, Yeow JTW. Polymer nanocomposite-based shielding against diagnostic X-rays. *Journal of Applied Polymer Science*. 2013;127:4939-46.
61. Harish V, Nagaiah N, Prabhu TN, Varughese KT. Preparation and characterization of lead monoxide filled unsaturated polyester based polymer composites for gamma radiation shielding applications.

Journal of Applied Polymer Science. 2009;112:1503-8.

62. Uthoff, H.; Benenati, M. J.; Katzen, B. T.; Pena, C.; Gandhi, R.; Staub, D.; Schernthaner, M., Lightweight bilayer barium sulfate-bismuth oxide composite thyroid collars for superior radiation protection in fluoroscopy-guided interventions: a prospective randomized controlled trial. *Radiology* 2014, 270 (2), 601-6.
63. Luo, C.; Chen, G.; Zhu, K.; Yuan, X., Preparation of X-ray developable LDPE/SA-BaSO₄ composites and their thermal and mechanical properties. *Polymer Composites* 2016, 37 (5), 1396-1406.
64. Arifin, D. R.; Manek, S.; Call, E.; Arepally, A.; Bulte, J. W. M., Microcapsules with intrinsic barium radiopacity for immunoprotection and X-ray/CT imaging of pancreatic islet cells. *Biomaterials* 2012, 33 (18), 4681-4689.
65. Nambiar S, Osei EK, Yeow JTW. Polymer nanocomposite-based shielding against diagnostic X-rays. *Journal of Applied Polymer Science*. 2013;127:4939-46.
66. Singh S, Kumar A, Singh D, Thind KS, Mudahar GS. Barium–borate–flyash glasses: As radiation shielding materials. *Nuclear Instruments and Methods in Physics Research Section B: Beam Interactions with Materials and Atoms*. 2008;266:140-6
67. Alyassin AM, Maqsoud HA, Mashat AM, Al-Mohr A-S, Abdulwajid S. Feasibility study of gamma-ray medical radiography. *Applied*

Radiation and Isotopes. 2013;72:16-29.

68. Shastri, P. V., Toxicology of polymers for implant contraceptives for women. *Contraception* 2002, 65 (1), 9-13.
- 69 . Nguyen, B. T.; Jensen, J. T., Evaluating the efficacy and safety of a progestin- and estrogen-releasing ethylene vinyl acetate copolymer contraceptive vaginal ring. *Expert Opin Drug Saf* 2014, 13 (10), 1423-30.
70. Fishbein, I.; Brauner, R.; Chorny, M.; Gao, J.; Chen, X.; Laks, H.; Golomb, G., Local delivery of mithramycin restores vascular reactivity and inhibits neointimal formation in injured arteries and vascular grafts. *Journal of Controlled Release* 2001, 77 (3), 167-181.
71. Hagiwara, K.; Hasebe, T.; Hotta, A., Effects of plasma treatments on the controlled drug release from poly(ethylene-co-vinyl acetate). *Surface and Coatings Technology* 2013, 216, 318-323.
72. Weinberg, B. D.; Blanco, E.; Gao, J., Polymer implants for intratumoral drug delivery and cancer therapy. *J Pharm Sci* 2008, 97 (5), 1681-702.
73. Fung, L. K.; Saltzman, W. M., Polymeric implants for cancer chemotherapy. *Advanced Drug Delivery Reviews* 1997, 26 (2–3), 209-230.
74. Hou, Y.; Chen, C.; Zhou, S.; Li, Y.; Wang, D.; Zhang, L., Fabrication of an integrated cartilage/bone joint prosthesis and its potential application in joint replacement. *J Mech Behav Biomed Mater* 2016,

59, 265-71.

75. Velayudhan, S.; Anilkumar, T. V.; Kumary, T. V.; Mohanan, P. V.; Fernandez, A. C.; Varma, H. K.; Ramesh, P., Biological evaluation of pliable hydroxyapatite-ethylene vinyl acetate co-polymer composites intended for cranioplasty. *Acta Biomater* 2005, 1 (2), 201-9.
76. Williams J, Pryor M, Landsberger S, Schulte L. A complete approach to reduce operator dosage in hazardous environments. 2011. p. 213-24.
77. Latha P, Vinodkumar AM, Varier KM, Babu BRS, Joseph A, Abdullah KK, et al. Effective atomic numbers for gamma ray interaction at 59.54 keV in heterogeneous layers of materials using ²⁴¹Am gamma rays. *Radiation Physics and Chemistry*. 2012;81:1817-22.
78. Flory PJ. Statistical thermodynamics of polymer solutions. *Principles of Polymer Chemistry*. 1953:495-540.
79. Flory PJ, Rehner Jr J. Statistical mechanics of cross-linked polymer networks II. Swelling. *The Journal of Chemical Physics*. 1943;11:521-6.
80. Dubey K, Bhardwaj Y, Chaudhari C, Sarma K, Goel N, Sabharwal S. Electron beam processing of LDPE/EVA/PCR ternary blends: radiation sensitivity evaluation and physico-mechanical characterization. *Journal of Polymer Research*. 2011;18:95-103.
81. Dubey KA, Bhardwaj YK, Chaudhari CV, Goel NK, Sabharwal S, Rajkumar K, et al. Radiation effects on styrene-butadiene-ethylene-

- propylene diene monomer-multiple walled carbon nanotube nanocomposites: Vulcanization and characterization. *Polymers for Advanced Technologies*. 2011;22:1888-97.
82. Makuuchi K, Cheng S. Chain Scission and Oxidation. *Radiation Processing of Polymer Materials and its Industrial Applications*: John Wiley & Sons, Inc.; 2012. 201-47.
83. Dubey KA, Bhardwaj YK, Chaudhari CV, Kumar V, Goel NK, Sabharwal S. Radiation processed ethylene vinyl acetate-multiple walled carbon nanotube nano-composites: Effect of MWNT addition on the gel content and crosslinking density. *Express Polymer Letters*. 2009;3:492-500.
84. Kraus G. Swelling of filler-reinforced vulcanizates. *Journal of Applied Polymer Science*. 1963;7:861-871.
85. Ahmed S, Jones FR. A review of particulate reinforcement theories for polymer composites. *J Mater Sci*. 1990;25:4933-42.
86. Li H, Tao S, Huang Y, Su Z, Zheng J. The improved thermal oxidative stability of silicone rubber by using iron oxide and carbon nanotubes as thermal resistant additives. *Composites Science and Technology*. 2013;76:52-60.
87. Kaewkhao J, Limsuwan P. Mass attenuation coefficients and effective atomic numbers in phosphate glass containing Bi₂O₃, PbO and BaO at 662;keV. *Nuclear Instruments and Methods in Physics Research Section A: Accelerators, Spectrometers, Detectors and Associated*

Equipment.619:295-7.

88. Dubey, K. A.; Majji, S.; Sinha, S. K.; Bhardwaj, Y. K.; Acharya, S.; Chaudhari, C. V.; Varshney, L., Synergetic effects of radiolytically degraded PTFE microparticles and organoclay in PTFE-reinforced ethylene vinyl acetate composites. *Materials Chemistry and Physics* 2013, 143 (1), 149-154.
89. Almeida, A.; Possemiers, S.; Boone, M. N.; De Beer, T.; Quinten, T.; Van Hoorebeke, L.; Remon, J. P.; Vervaet, C., Ethylene vinyl acetate as matrix for oral sustained release dosage forms produced via hot-melt extrusion. *European Journal of Pharmaceutics and Biopharmaceutics* 2011, 77 (2), 297-305.
90. Martínez de Arenaza, I.; Sadaba, N.; Larrañaga, A.; Zuza, E.; Sarasua, J. R., High toughness biodegradable radiopaque composites based on polylactide and barium sulphate. *European Polymer Journal* 2015, 73, 88-93.
91. Cui, J.; Kratz, K.; Heuchel, M.; Hiebl, B.; Lendlein, A., Mechanically active scaffolds from radio-opaque shape-memory polymer-based composites. *Polymers for Advanced Technologies* 2011, 22 (1), 180-189.
92. Brice, D. K., Stopping powers for electrons and positrons (ICRU report 37; International commission on radiation units and measurements, Bethesda, Maryland, USA, 1984): pp. viii + 267, \$24.00; ISBN 0-913394-31-9. *Nuclear Instruments and Methods in*

Physics Research Section B: Beam Interactions with Materials and Atoms 1985, 12 (1), 187-188.

93. Dubey, K. A.; Mondal, R. K.; Grover, V.; Bhardwaj, Y. K.; Tyagi, A. K., Development of a novel strain sensor based on fluorocarbon-elastomeric nanocomposites: Effect of network density on the electromechanical properties. *Sensors and Actuators, A: Physical* 2015, 221, 33-40.
94. Yang, J.; Han, C.-R.; Zhang, X.-M.; Xu, F.; Sun, R.-C., Cellulose Nanocrystals Mechanical Reinforcement in Composite Hydrogels with Multiple Cross-Links: Correlations between Dissipation Properties and Deformation Mechanisms. *Macromolecules* 2014, 47 (12), 4077-4086.
95. Wang, K.; Wu, J.; Ye, L.; Zeng, H., Mechanical properties and toughening mechanisms of polypropylene/barium sulfate composites. *Composites Part A: Applied Science and Manufacturing* 2003, 34 (12), 1199-1205.
96. Kossuth, M. B.; Morse, D. C.; Bates, F. S., Viscoelastic behavior of cubic phases in block copolymer melts. *Journal of Rheology* 1999, 43 (1), 167-196.
97. González, O.; Muñoz, M. E.; Santamaría, A.; García-Morales, M.; Navarro, F. J.; Partal, P., Rheology and stability of bitumen/EVA blends. *European Polymer Journal* 2004, 40 (10), 2365-2372.
98. Nusser, K.; Schneider, G. J.; Richter, D., Rheology and Anomalous

Flow Properties of Poly(ethylene-alt-propylene)–Silica Nanocomposites. *Macromolecules* 2013, 46 (15), 6263-6272.

99. Cardiel, J. J.; Dohnalkova, A. C.; Dubash, N.; Zhao, Y.; Cheung, P.; Shen, A. Q., Microstructure and rheology of a flow-induced structured phase in wormlike micellar solutions. *Proceedings of the National Academy of Sciences of the United States of America* 2013, 110 (18), E1653-E1660.
100. Nait-Ali, K. L.; Bergeret, A.; Ferry, L.; Colin, X., Chain branching detection by Cole–Cole modeling of rheological properties changes during PET mechanical recycling. *Polymer Testing* 2012, 31 (3), 500-504.
101. Payne, A. R., The dynamic properties of carbon black loaded natural rubber vulcanizates. Part II. *Journal of Applied Polymer Science* 1962, 6 (21), 368-372.
102. Kraus, G., Reinforcement of Elastomers by Carbon Black. *Rubber Chemistry and Technology* 1978, 51 (2), 297-321.
103. Kraus, G. In Mechanical losses in carbon-black-filled rubbers, *Journal of Applied Polymer Science: Applied Polymer Symposium*, 1984; 75-92.
104. Boland, C. S.; Khan, U.; Ryan, G.; Barwich, S.; Charifou, R.; Harvey, A.; Backes, C.; Li, Z.; Ferreira, M. S.; Möbius, M. E.; Young, R. J.; Coleman, J. N., Sensitive electromechanical sensors using viscoelastic graphene-polymer nanocomposites. *Science* 2016,

354 (6317), 1257-1260.

105. Williams, M. L.; Landel, R. F.; Ferry, J. D., The Temperature Dependence of Relaxation Mechanisms in Amorphous Polymers and Other Glass-forming Liquids. *Journal of the American Chemical Society* 1955, 77 (14), 3701-3707.
106. Knoglinger, H.; Schausberger, A.; Janeschitz-Kriegl, H., The role of short chain molecules for the rheology of polystyrene melts. *Rheologica Acta* 1987, 26 (5), 460-467.
107. Pedrazzoli, D.; Pegoretti, A.; Kalaitzidou, K., Synergistic effect of exfoliated graphite nanoplatelets and short glass fiber on the mechanical and interfacial properties of epoxy composites. *Composites Science and Technology* 2014, 98, 15-21
108. Chmielewski, A.G., Al-Sheikhly, M., Berejka, A.J., Cleland, M.R., Antoniuk, M., Recent developments in the application of electron accelerators for polymer processing. *Radiat. Phys. Chem.* 2014. 94, 147-150.
109. Dubey, K.A., Bhardwaj, Y.K., Chaudhari, C.V., Bhattacharya, S., Gupta, S.K., Sabharwal, S., Radiation effects on SBR–EPDM blends: A correlation with blend morphology. *J. Polym. Sci. Pol. Phys* 2006. 44, 1676-1689
110. Dubey, K.A., Majji, S., Sinha, S.K., Bhardwaj, Y.K., Acharya, S., Chaudhari, C.V., Varshney, L., Synergetic effects of radiolytically degraded PTFE microparticles and organoclay in PTFE-reinforced

- ethylene vinyl acetate composites. *Mater. Chem. Phys.* 2013.143, 149-154.
111. Biramontri, S., Haneda, N., Effect of low irradiation temperature on the gamma-ray response of dyed and undyed PMMA dosimeters. *Radiat. Phys. Chem.* 1996; 48; 105-109.
 112. Devic, S., Radiochromic film dosimetry: Past, present, and future. *Physica Medica* 2011; 27; 122-126.
 113. Galante, A.M.S., Villavicencio, A.L.C.H., Campos, L.L., Sisti Galante, A.M., Preliminary investigations of several new dyed PMMA dosimeters. *Radiat. Phys. Chem.* 2004; 71; 391-394.
 114. Whittaker, B., Uncertainties in absorbed dose as measured using PMMA dosimeters. *Radiat. Phys. Chem.* 1993; 42; 841-844.
 115. Bett, R., Watts, M.F., Plested, M.E., The shelf life of dyed polymethylmethacrylate dosimeters. *Radiat. Phys. Chem.* 2002; 63; 793-797.
 116. Kattan, M., al Kassiri, H., Daher, Y., Using polyvinyl chloride dyed with bromocresol purple in radiation dosimetry. *Appl. Radiat. Isotopes* 2011; 69, 377-380.
 117. McLaughlin, W.L., Radiation chemistry of anionic disazo dyes in Cellophane films applications for high-dose dosimetry. *Radiat. Phys. Chem.* 2003; 67, 561-567.
 118. Tu, N.T., Dung, N.V., Nghiep, T.D., Dose response of polyvinyl alcohol films dyed by methyl red under gamma irradiation. *Int. J.*

- Low Radiat. 2009; 6; 177-184.
119. Whittaker, B., Bett, R., Plested, M.E., Watts, M.F., Extending the dose range of the red 4034 PMMA dosimeter. Radiat. Phys. Chem. 1997; 49; 505-508.
120. Soliman, Y.S., Abdel-Fattah, A.A., Leuco crystal violet/poly (vinyl butyral) thin film as a high-dose dosimeter. Radiat. Meas. 2013; 49, 1-6.
121. Ajji, Z., 2006. Usability of aqueous solutions of methyl red as high-dose dosimeter for gamma radiation. Radiat. Meas. 41, 438-442.
122. Al Zahrary, A., Rabaeh, K., Basfar, A., Radiation-induced color bleaching of methyl red in polyvinyl butyral film dosimeter. Radiat. Phys. Chem. 2011; 80; 1263-1267.
123. Barakat, M.F., El-Salamawy, K., El-Banna, M., Abdel-Hamid, M., Abdel-Rehim Taha, A., Radiation effects on some dyes in non-aqueous solvents and in some polymeric films. Radiat. Phys. Chem. 2001; 61; 129-136.
124. Russo, M., D'Angelantonio, M., Takács, E., Lavallo, M., Fuochi, P.G., Emmi, S.S., Effects of different matrixes on the dosimetric response of α -terthiophene films from the kGy to MGy range. Radiat. Phys. Chem. 2002a; 63; 781-784.
125. Dubey, K.A., Bhardwaj, Y.K., Rajkumar, K., Panicker, L., Chaudhari, C.V., Chakraborty, S.K., Sabharwal, S., Polychloroprene rubber/ethylene-propylene diene monomer/multiple walled carbon

- nanotube nanocomposites: synergistic effects of radiation crosslinking and MWNT addition. *J. Polym. Res.* 2012; 19; 9876-9876.
126. Meiner, J., Mellor, P., Patil, D., Garcia, R., Temperature response for the Harwell Red 4034 Perspex® dosimeter. *Radiat. Phys. Chem.* 2004; 71; 397-399.
127. Dubey, K.A., Bhardwaj, Y.K., Chaudhari, C.V., Goel, N.K., Sabharwal, S., Rajkumar, K., Chakraborty, S.K., Radiation effects on styrene-butadiene-ethylene-propylene diene monomer-multiple walled carbon nanotube nanocomposites: vulcanization and characterization. *Polym. Advan. Technol.* 2011; 22; 1888-1897.
128. Babic, S., McNiven, A., Battista, J., Jordan, K., Three-dimensional dosimetry of small megavoltage radiation fields using radiochromic gels and optical CT scanning. *Phys. Med. Biol.* 2009; 54; 2463-2481.
129. Kozicki, M., Sasiadek, E., Polyamide woven fabrics with 2,3,5-triphenyltetrazolium chloride or nitro blue tetrazolium chloride as 2D ionizing radiation dosimeters. *Radiat. Meas.* 2012; 47; 614-621.
130. Robilă, G., Buruiană, E.C., Caraculacu, A.A., Determination of labile chlorine in PVC with the aid of phenolysis reaction. *Eur. Polym. J.* 1977; 13; 21-24.
131. Luther, D.W., Linsky, L.A., Improving gamma radiation resistance: Medical grade, flexible clear PVC compounds. *J. Vinyl Add. Techn.* 1996; 2, 190-192.

132. Guild, J., the Colorimetric Properties of the Spectrum. Philos. Soc. 1932; 230, 149-187.
133. Arakawa, K., Seguchi, T., Yoshida, K., Radiation-induced gas evolution in chlorine- containing polymer. Poly(vinyl chloride), chloroprene rubber, and chlorosulfonated- polyethylene. Radiat. Phys. Chem. 1986; 27, 157-163.
134. Russo, M, D'Angelantonio, M., Takács, E., Lavalle, M., Fuochi, P.G, Emmi, S.S.,. Effects of different matrixes on the dosimetric response of α -terthiophene films from the kGy to MGy range. Radiat. Phys. Chem. 2002b; 63, 781-784.
135. Whittaker, B., Watts, M.F., The influence of dose rate, ambient temperature and time on the radiation response of Harwell PMMA dosimeters. Radiat. Phys. Chem. 2001; 60, 101-110.
136. Basfar, A.A., Rabaeh, K.A., Moussa, A.A., Msalam, R.I; Dosimetry characterization of nitro-blue tetrazolium polyvinyl butyral films for radiation processing. Radiation Radiat. Phys. Chem. 2011; 80, 763-766.
137. Galante, A.M.S., Campos, L.L., 2006. Electron dose radiation response of dyed PMMA detectors developed at IPEN. Radiat. Prot. Dosim. 120, 113-116.
138. Mai, H.H., Solomon, H.M., Taguchi, M., Kojima, T., Hoa, H., Polyvinyl butyral films containing leuco-malachite green as low-dose dosimeters. Radiat. Phys. Chem. 2008; 77, 457-462.

139. Dubey, K.A., Bhardwaj, Y.K., Chaudhari, C.V., Kumar, V., Goel, N.K., Sabharwal, S., Radiation processed polychloroprene-co-ethylene-propene diene terpolymer blends: Effect of radiation vulcanization on solvent transport kinetics. *Nucl. Instrum. Meth. B.* 2009; 267; 795-801.
140. Berejka, A.J., Cleland, M.R., Walo, M., 2014. The evolution of and challenges for industrial radiation processing; *Radiat. Phys. Chem.* 2012; 94, 141-146.
141. Negron-Mendoza A, Uribe RM, Ramos-Bernal S, Camargo-Raya C, Gomez-Vidales V, Kobayashi K. Calcium carbonate as a possible dosimeter for high irradiation doses. *Applied Radiation and Isotopes.* 2015; 100: 55-59.
142. Mikou M, Ghosne N, El Baydaoui R, Zirari Z, Kuntz F. Performance characteristics of the EPR dosimetry system with table sugar in radiotherapy applications. *Applied Radiation and Isotopes.* 2015; 99:1-4.
143. Steven B, Andrea M, Jerry B, Kevin J. Three-dimensional dosimetry of small megavoltage radiation fields using radiochromic gels and optical CT scanning. *Physics in Medicine and Biology.* 2009;54(8):2463.
144. Tuner H, Oktay Bal M, Polat M. Radiation sensitivity and EPR dosimetric potential of gallic acid and its esters. *Radiation Physics and Chemistry.* 2015; 107:115-120.

145. Alzimami K S, Maghraby A M, Bradley D A. Comparative study of some new EPR dosimeters. *Radiation Physics and Chemistry*. 2014; 95:109-112.
146. Khoury HJ, da Silva Jr EJ, Mehta K, de Barros VS, Asfora VK, Guzzo PL, et al. Alanine-EPR as a transfer standard dosimetry system for low energy X radiation. *Radiation Physics and Chemistry*. 2015, 116; 147-150.
147. Levêque P, Desmet C, Dos Santos-Goncalvez AM, Beun S, Leprince JG, Leloup G, et al. Influence of Free Radicals Signal from Dental Resins on the Radio-Induced Signal in Teeth in EPR Retrospective Dosimetry. *Applied Radiation & Isotope*. 59, 181-188.
148. Lelie S, Hole EO, Duchateau M, Schroeyers W, Schreurs S, Verellen D. The investigation of lithium formate hydrate, sodium dithionate and N-methyl taurine as clinical EPR dosimeters. *Radiation Measurements*. 2013; 59:218-224.
149. Nakagawa K, Sato Y. Investigation of Heavy-Ion-Induced Sucrose Radicals by Electron Paramagnetic Resonance. *Radiation Research*. 2005; 164(3):336-8.
150. Aboelezz E, Hassan GM, Sharaf MA, El-Khodary A. EPR dosimetric properties of nano-barium sulfate. *Radiation Physics and Chemistry*. 2015; 106:385-93.
151. Morton J R, Ahlers F J, Schneider C C J. ESR Dosimetry with Magnesium Sulphate. *Radiation Protection Dosimetry*. 1993; 47(1-

4):263-6.

152. Rushdi M A H, Abdel-Fattah A, Sherif M M, Soliman Y S, Mansour A. Strontium sulfate as an EPR dosimeter for radiation technology application. *Radiation Physics and Chemistry*. 2015; 106:130-5.
153. Tani A, Hasegawa N, Norizawa K, Yada T, Ikeya M. Radiation-induced radicals in hydrated magnesium sulfate. *Radiation Measurements*. 2012; 47(9):890-3.
154. Negron-Mendoza A, Uribe RM, Ramos-Bernal S, Camargo-Raya C, Gomez-Vidales V. The gamma ray response of alanine film dosimeters at low temperatures. *Applied Radiation and Isotopes*. 2012; 71, Supplement: 61-65.
155. Gancheva V, Yordanov N D, Callens F, Vanhaelewyn G, Raffi J, Bortolin E, et al. An international intercomparison on “self-calibrated” alanine EPR dosimeters. *Radiation Physics and Chemistry*. 2008; 77(3):357-64.
156. Al-Karmi A M, Morsy M A. EPR of gamma-irradiated polycrystalline alanine-in-glass dosimeter. *Radiation Measurements*. 2008;43(7):1315-8.
157. Lin M, Li H, Chen Y, Cui Y, Xiao Z, Chen K, et al. Thin film alanine-PE dosimeter for electron beam transfer dosimetry. *Radiation Physics and Chemistry*. 2005; 73(5):280-6.
158. Dubey K A, Sinha S K, Bhardwaj Y K, Panicker L, Varshney L. Carbon Black-Filled PE/PP/EPDM Blends: Phase Selective

- Localization of Carbon Black and EPDM-Induced Phase Stabilization. *Polymer - Plastics Technology and Engineering*. 2014; 53(5):442-50.
159. Suman S K, Dubey K A, Mishra B B, Bhardwaj Y K, Mondal R K, Seshadri M, et al. Synthesis of a flexible poly(chloroprene)/methyl red film dosimeter using an environment-benign shear compounding method. *Applied Radiation and Isotopes*. 2015; 98:60-5.
 160. Dubey K A, Bhardwaj Y K, Chaudhari C V, Sabharwal S. LDPE/EVA/PCR/MWNT nanocomposites: Radiation crosslinking and physicomechanical characteristics. *Polymer Composites*. 2011; 32(5):737-46.
 161. Meesat R, Sanguanmith S, Meesungnoen J, Lepage M, Khalil A, Jay-Gerin JP. Utilization of the ferrous sulfate (Fricke) dosimeter for evaluating the radioprotective potential of cystamine: experiment and Monte Carlo simulation. *Radiat Res*. 2012; 177(6):813-26.
 162. Chaudhari C V, Dubey K A, Bhardwaj Y K, Naxane G, Sarma K S S, Sabharwal S. Effect of electron beam radiation on the polypropylene/polyethylene blends: Radiation stabilization of polypropylene. *Nuclear Instruments and Methods in Physics Research, Section B: Beam Interactions with Materials and Atoms*. 2007; 263(2):451-7.
 163. Dubey K A, Bhardwaj Y K, Chaudhari C V, Goel N K, Sabharwal S, Rajkumar K, et al. Radiation effects on styrene-butadiene-ethylene-

- propylene diene monomer-multiple walled carbon nanotube nanocomposites: Vulcanization and characterization. *Polymers for Advanced Technologies*. 2011; 22(12):1888-97.
164. Brice D K. Stopping powers for electrons and positrons *Nuclear Instruments and Methods in Physics Research Section B: Beam Interactions with Materials and Atoms*.1985; 12(1):187-8.
165. M. Ikeya, G.M. Hassan, H. Sasaoka, Y. Kinoshita, S. Takaki, C. Yamanaka; Strategy for finding new materials for ESR dosimeters, *Applied Radiation and Isotopes*. 2000; 52; 1209-1215.
166. M.A. Sharaf, Gamal M. Hassan; Radiation induced radical in barium sulphate for ESR dosimetry: a preliminary study; *Nuclear Instruments and Methods in Physics Research*. 2004; B 225, 521–527
167. Soliman Y S, Abdel-Fattah A A, Magnesium lactate mixed with EVA polymer/paraffin as an EPR dosimeter for radiation processing application *Radiation Physics and Chemistry* 81 (12), 1910-1916
168. Brady, J. M., Aarestad, N. O., Swartz,H.M. In-vivo dosimetry by electron spin resonance spectroscopy.*HealthPhys*. 1968; 15, 43–47.
- 169.Desrosiers,M.F.,Schauer,D.A.,2001.Electronparamagneticresonance(EPR) biodosimetry. *Nucl. Instrum. Methods* 184(1–2), 219–228.
- 170.SchauerD.A.,IwasakiA.,Romanyukha,A.A.,Swartz,H.M.,Onori,S.,Electron paramagnetic resonance(EPR) in medical dosimetry. *Radiat. Meas*. 2007; 41; 117–123.

171. B.C.Bhat, S.S.Sanaye, S.S,Shinde, and J.K. Srivastava; Radiat. Prot. Dosim, 1997; 69(2); 105-106
172. Numan Salah, Sami S.Habib, Zishan S. Khan, Salim Al Hamedi, S.P. Lochab; J. Lumin., 2009; 129(3); 192-193.
173. J. Manam, S. Das, Characterization and TSL dosimetric properties of Mn doped BaSO₄ phosphor prepared by recrystallisation method, Journal of Alloys and Compounds, 2010; 489; 84–90.
174. U. Madhusoodanan, M.T. Jose, A.R. Lakshmanan, Development of BaSO₄: Eu;The luminescence phosphor, Radiation Measurements;1999; 30; 65-72.
175. E. Aboelezz , G.M.Hassan , M.A.Sharaf , A.El-Khodary, EPR dosimetric properties of nano-barium sulfate, Radiation Physics and Chemistry 2015;106; 385–393.
176. O.Annalakshmi, M. T. Jose* and U. Madhusoodanan, synthesis and characterization of BaSO₄: Eu Thermo luminescence phosphor, Radiation Protection Dosimetry (2012), 1-7.